Alma Mater Studiorum · Università di Bologna

SCUOLA DI SCIENZE
Corso di Laurea Magistrale in Astrofisica e Cosmologia
Dipartimento di Fisica e Astronomia

Interpreting the CO SLED with starburst and AGN feedback

Tesi di Laurea Magistrale

Candidato:
Federico Esposito

Relatore:
Chiar.ma Prof.
Francesca Pozzi

Co-relatore:
Prof. Andrea Cimatti

Sessione II
Anno Accademico 2016/17

If science teaches us anything,
it teaches us to accept our failures
as well as our successes,
with quiet dignity and grace.
Gene Wilder

Sommario

Il presente lavoro di tesi si basa sullo spettro rotazionale del monossido di carbonio (CO) di galassie locali, e lo interpreta sulla base della densità del mezzo molecolare responsabile dell'emissione e del tipo di sorgente radiativa che eccita tale molecola. Due tipi di sorgente sono stati considerati in questo lavoro: popolazioni stellari con formazione stellare attiva, contenenti quindi stelle giovani, calde e con un'importante luminosità ultravioletta, ed un nucleo galattico attivo (AGN), il cui spettro contiene anche molti (rispetto alle stelle) fotoni in banda X.

La CO SLED è stata ricavata principalmente da osservazioni del satellite infrarosso Herschel. Abbiamo scelto di studiare solo le galassie con la CO SLED con un picco il più possibile a frequenze alte, in modo da massimizzare la probabilità che l'emissione dell'AGN fosse fondamentale per interpretare le osservazioni.

Abbiamo quindi usato i dati disponibili nell'archivio dell'Atacama Large Millimeter/submillimeter Array (ALMA) relativi alle galassie selezionate, e abbiamo prodotto le mappe spazialmente risolte dell'emissione del CO delle osservazioni trovate. Questo ci ha permesso di stabilire un'area fisica all'interno delle galassie entro cui il gas molecolare è presente ed emette radiazione. Le galassie con la CO SLED di interesse osservata da Herschel e, contemporaneamente, con osservazioni di CO disponibili dall'archivio ALMA, sono al momento 4: IRAS F05189−2524, NGC 34, NGC 4418 e NGC 6240.

Con il codice di sintesi spettrale CLOUDY (Ferland et al. 2013) abbiamo preparato due griglie di simulazioni per modelli PDR (*photo-dissociation region*, in cui la sorgente radiativa sono le popolazioni stellari) e modelli XDR (*X-ray dissociation region*, dove la sorgente radiativa è un AGN). I risultati di queste simulazioni sono stati combinati nei modelli finali, composti di due PDRs o di una PDR ed una XDR; la CO SLED simulata è stata quindi comparata a quella osservata tramite una procedura di minimizzazione.

I risultati ottenuti sono i seguenti: per due galassie (NGC 34 e NGC 6240) il modello di best-fit è quello a doppia PDR, per le altre due (IRAS F05189−2524 e NGC 4418) è quello che comprende un modello di PDR ed uno di XDR. I risultati riguardanti NGC 4418 vanno considerati con cautela in quanto il codice di minimizzazione non è riuscito a trovare un buon fit della CO SLED (il chi quadro ridotto minimo per questa galassia è $\chi^2_\nu = 16$).

I 4 oggetti selezionati non sembrano dominati dalla presenza delle XDRs per quanto riguarda l'eccitazione del gas molecolare. Nel caso di IRAS F05189−2524, anche se il fit che include l'AGN ha un χ^2 migliore, la sua probabilità non è significativamente superiore a quella con doppia PDR. Da tali considerazioni si evince che per tutte e 4 le galassie analizzate il contributo dell'AGN (osservato in tutte tranne che in NGC 4418) nel determinare la fisica del gas interstellare non è dominante.

Dai modelli di best-fit sono state ricavate le masse di gas, e da queste sono stati calcolati i fattori di conversione $\alpha_{CO} \equiv M_{mol}/L_{CO}$ e i depletion times $\tau_{depl} \equiv M_{mol}/SFR$. Tali grandezze sono state confrontate con galassie presenti in letteratura, permettendo di inserire le galassie di questa tesi in un contesto scientifico più ampio.

La tesi è organizzata nel seguente modo:

- nel capitolo 1 viene data una panoramica sull'ambiente galattico in cui ci muoviamo: dalle diverse fasi del mezzo interstellare a maggiori dettagli sul gas molecolare; nell'ultima parte del capitolo introduciamo la formazione stellare, i fenomeni di starburst e i nuclei galattici attivi;
- il capitolo 2 contiene la selezione del campione di galassie su cui si è concentrato il lavoro di tesi, l'osservazione della CO SLED con Herschel e la produzione delle mappe delle emissioni del CO dai dati ALMA disponibili;
- nella prima parte del capitolo 3 viene spiegato come abbiamo impostato le simulazioni fatte con il codice CLOUDY; nella seconda parte gli esiti di queste simulazioni sono comparati ai dati osservati tramite un codice di minimizzazione; alla fine del capitolo per ogni galassia si avrà un *miglior* modello
- nel capitolo 4 le masse di gas dei modelli di best-fit sono utilizzate per inserire le galassie studiate in un contesto più generale

Abstract

The present thesis work is based on the rotational spectrum of carbon monoxide (CO) of local galaxies, and interprets it on the basis of the density of the emitting molecular medium and of the type of radiative source which excites such molecule. Two kinds of radiative sources have been considered in this work: stellar populations with active star formation, thus containing young and hot stars with significant ultraviolet luminosity, and an active galactic nucleus (AGN), whose spectrum contains lots (compared to stars) of X-ray photons.

The CO SLED has been obtained mainly from observations made by the infrared satellite Herschel. We have chosen to study only the galaxies with the CO SLED more peaked at high frequencies in order to maximize the probability for the AGN emission to be fundamental in the interpretation of the observations.

We have used the available data from the Atacama Large Millimeter/submillimeter Array (ALMA) archive for the selected galaxies, and thus we have produced the spatially resolved maps of CO emission for the observations found. This has permitted to establish a physical area for the galaxies within which molecular gas is present and emits radiation. The galaxies with the CO SLED of interest observed by Herschel and, at the same time, with available CO observations from the ALMA archive are 4: IRAS F05189−2524, NGC 34, NGC 4418 e NGC 6240.

With the spectral synthesis code CLOUDY (Ferland et al. 2013) we have prepared two simulation grids: one for PDR (*photo-dissociation region*) models, in which the radiative sources are stellar populations, the other for XDR (*X-ray dissociation region*) models, where the radiative source is the AGN. The results of these simulations have been combined in the final models, made by two PDRs or a PDR and an XDR; the simulated CO SLED have been therefore compared to the observed one using a minimization procedure.

The final results are as follows: for two galaxies (NGC 34 and NGC 6240) the best-fit model is the double PDR one, whereas for the other two (IRAS F05189−2524 and NGC 4418) it is the PDR + XDR one. Outcomes regarding NGC 4418 have to be considered with caution, since the minimization code has not been able to find a good fit of its CO SLED (the minimum reduced chi-square for this galaxy being $\chi^2_\nu = 16$).

The 4 selected objects do not seem to be dominated by the presence of XDRs for

what concern the molecular gas excitation. In the case of IRAS F05189−2524, even if the fit with the AGN included has a better χ^2, its associated probability is not significantly greater than the double PDR model one. From such considerations it is evident that, for all 4 analyzed galaxies, the AGN contribute (observed in all except in NGC 4418) is not dominant in determining the physics of the interstellar gas.

From the best-fit models the gas masses have been obtained, and from these the conversion factors $\alpha_{CO} \equiv M_{mol}/L_{CO}$ and the depletion times $\tau_{depl} \equiv M_{mol}/SFR$ have been calculated for each galaxy. Such values have been compared with galaxies in literature, allowing to include the galaxies of this thesis in a wider scientific context.

This thesis is organized as follows:

- in the chapter1 a general view on the galactic environments is given: from the different phases of the interstellar medium to details about the molecular gas; in the last part of the chapter we introduce the phenomena of star formation, starburst and active galactic nuclei;
- chapter 2 contains the selection of the sample of galaxies on which is based this thesis, the observation of the CO SLEDs with Herschel and the production of CO emission maps from the available ALMA data;
- in the first part of chapter 3 the setting of simulations made with the CLOUDY code is explained; in the second part the results of such simulations are compared to the observed data using a minimization code; at the end of the chapter a best model is named for each galay;
- in chapter 4 the gas masses of best-fit models permit us to include the studied galaxies in a more general context

Contents

Chapter 1

The galactic content and processes

1.1 The phases of the interstellar medium

The interstellar medium (ISM) is the gaseous component of galaxies, one of the three main ingredients that form a galaxy together with stars and dark matter.

The ISM is at the same time a byproduct of stars, via stellar winds and supernovae explosions, and the raw material from which new stars form. In section 1.3.1 this second aspect is analyzed in detail, whereas here we want to break up the ISM in its major components, that cover a wide range in densities and temperatures. The physical properties of the ISM are heavily influenced by the radiation sources within it, mainly stars and, if active, the galactic nucleus (section 1.3.2).

The atoms that compose the interstellar medium are about 70% hydrogen, 28% helium and 2% metals (i.e. all the other atoms from the lithium up). As hydrogen is the most present species, a typical way to divide the ISM is to consider the three phases in which hydrogen exists: ionized, neutral and molecular.

Galaxies can be roughly divided in 2 classes: *early-type galaxies* (ETGs, namely ellipticals and lenticulars) have a spheroidal shape, little cold gas content and little specific star formation rate ($sSFR \equiv SFR/M_*$, i.e. star formation rate normalized to the stellar mass of the galaxy - see section 1.3.1 for details), while *late-type galaxies* (LTGs, i.e. spirals and irregulars) have a spiral (sometimes with a bar) or unrecognizable shape, they are rich in cold gas and show a higher sSFR. Since the focus of this thesis work lies on molecular gas, the galaxies of interest in our case are the LTGs.

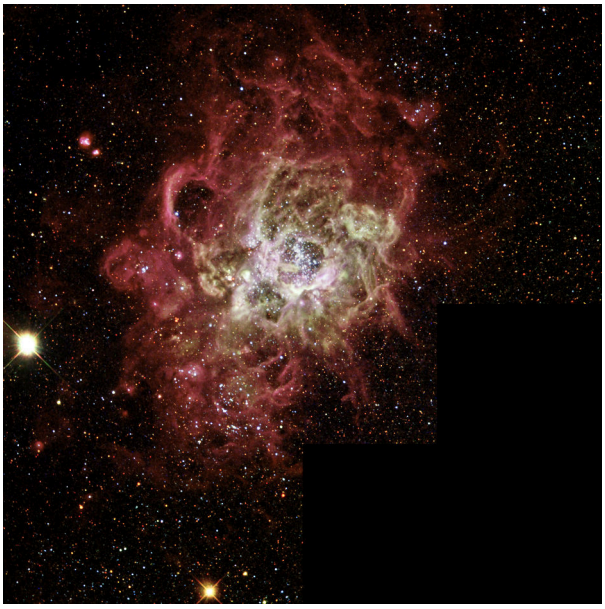

Figure 1.1: The HII region NGC 604 within the galaxy M33, seen by the Wide-Field Planetary Camera 2 (WFPC2) of the Hubble Space Telescope. The image is a combination of several filters, included the ones built around the frequencies of [OII] and Hα lines cited in the text. Taken from the Hubble Space Telescope website http://hubblesite.org/image/1423/gallery/91-astronomical

1.1.1 Ionized medium

(H^+ ion for chemists), and it is basically just a proton. Anyway, the lost electrons remain in the same region occupied by protons, so the ISM is overall a neutral medium. Hydrogen can be ionized in two ways: via photons with energy $h\nu > 13.6$ eV (13.6 eV, or, equivalently, 1 Ry, is the required energy to promote a hydrogen electron from the quantum ground level $n = 1$ up to $n = \infty$) and via collisions with other atoms.

Ionized hydrogen is called by astronomers HII The photo-ionized ISM needs a EUV (Extreme Ultra-Violet) source to be constantly photo-ionized, and typically these sources are young and hot stars of spectral classes O and B: these stars have surface temperatures approximately 3×10^4 K and 1.5×10^4 K (Karttunen et al. 2007), so they irradiate respectively 21% and 1% of their luminosity (see section 1.2.3 and equation 1.2.3 for this calculation) in EUV band (i.e. between 13.6 and 150 eV). The HII regions around O-B stars, also called Strömgren spheres (from the fact that *in theory* they should remain spherical), are mainly seen via *recombination lines*, which occur when electrons are recaptured by ions; the ubiquitous Balmer and Paschen lines form in this way.

Other very important lines in HII regions are the *forbidden lines*, like [OII] (square brackets stay for forbidden): the transitions that generate these lines are called forbidden because they have a low probability to occur spontaneously; this probability is called Einstein A coefficient, and it is of the order of 10^{-5} s^{-1} for the [OII] 3726 nm line, compared to $\sim 10^7$ s^{-1} for Hα. In high-density environments the collisional de-excitations

are way more probable than these radiative transitions, so they are really forbidden on the Earth for example, where the typical density is $\sim 10^{19}$ cm^{-3}; conversely the ISM can reach densities lower than 1 cm^{-3}, so that also collisions are very rare, and spontaneous forbidden emissions are able to come off.

The collisionally ionized ISM needs a temperature $T > 10^4$ K in order to have sufficient atoms to ionize the bulk of the gas (given that the atoms velocities follow the Maxwell-Boltzmann distribution). These temperatures occur mainly with supersonic velocities, so in presence of shock waves, produced by stellar feedback (stellar winds, supernovae explosions) or by gas accretion from outside the galaxy. It emits primarily a continuum spectrum given by the collisions between ions and electrons, a process called *bremsstrahlung* radiation.

1.1.2 Neutral atomic medium

Neutral hydrogen (called HI by astronomers) is distributed in two different phases: the Cold Neutral Medium (CNM), with $T \sim 70$ K and tipically high densities as $n \sim 50$ cm^{-3}, and the Warm Neutral Medium (WNM), with $T \sim 7000$ K and $n \sim 0.5$ cm^{-3}. Thanks to the thermal instability[1], given that the different parts of ISM are in pressure equilibrium (i.e. have the same pressure, which is about 3×10^{-13} dyne cm^{-2} in the Milky Way), the gas cannot stay at any temperature (if thermally stable), and for this reason we can talk about separate ISM phases.

Neutral hydrogen is seen through the 21-cm hydrogen line, i.e. the emission line resulting from the spin-flip transition of the hydrogen electron, from parallel to anti-parallel with respect to the nucleus. This transition is highly forbidden, with a Einstein coefficient $A \sim 10^{-15}$ s^{-1}, which corresponds to a typical timescale $\tau \sim 1/A \sim 10^7$ yr. However, thanks to the low density of ISM and to the abundance of neutral hydrogen, the 21-cm is one of the most observed lines in the Universe.

This emission is ubiquitous among spiral galaxies, and shows a gas disk superimposed but more extended than the stellar one. The Doppler shift of the line, once subtracted the effect of the expansion of the Universe (i.e. the cosmological redshift) tells us the radial velocity of the HI disk. Plotting this velocity as a function of the distance from the center of a spiral galaxy shows a so-called *flat rotation curve*: the velocity rises leaving the galactic center until a point at which it becomes constant. If we pose, for simplicity, that the orbits are circular, the gravitational acceleration $GM(R)/R^2$ has to be equal to the centripetal acceleration $v^2(R)/R$, where R is the distance from the center of the galaxy. From this simple equation is straightforward to say that if $V(R)$ is constant with

[1] From the first law of thermodynamics for specific quantities (i.e. per unit mass), $Td\mathcal{S} = d\mathcal{U} + Pd\mathcal{V}$, ignoring the heat conduction, is possible to write the *heat equation* $D\mathcal{S}/Dt = -\mathcal{L}/T$, where $\mathcal{L} = \Lambda - \Gamma$ is the difference between radiative cooling (Λ) and heating (Γ). From this equation, with a small perturbation in entropy, it is feasible to extract the Field criterion for thermal stability, $(\partial\mathcal{L}/\partial T)_P > 0$ (Field 1965). In practice this criterion splits the ISM in well defined stable phases (given the pressure equilibrium between the phases).

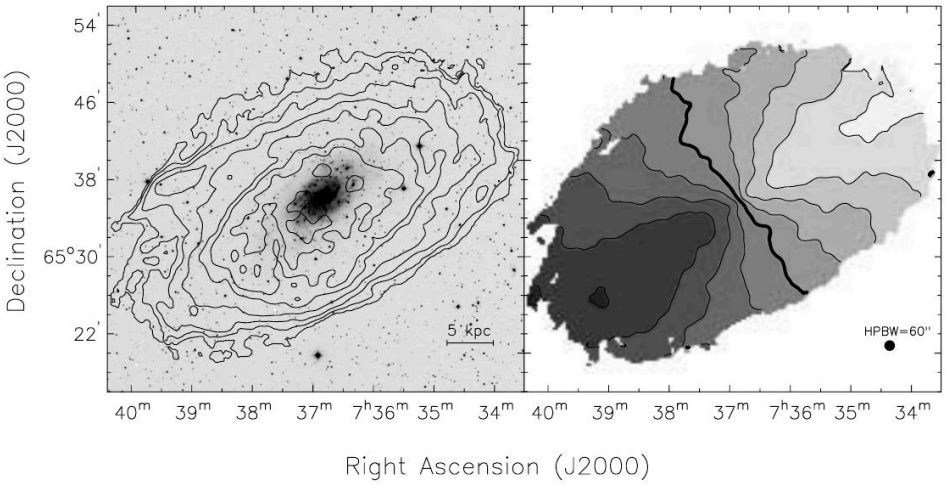

Figure 1.2: HI emission of the spiral galaxy NGC 2403. On the left HI contours are overlaid to the optical image, on the right is the velocity field of the neutral gas: every different shade represents a different velocity, where the darker is receding while the lighter is approaching us with respect to the central thick line, which is the systemic velocity. Taken from Fraternali et al. 2002, figure 6.

R, $M(R)$ has to grow linearly with R, even if the mass is *visibly* decreasing. This is one of the main proofs of the existence of dark matter.

1.1.3 Molecular medium

Molecular hydrogen (called H_2 in concert with chemists) has been found in recent years in all kind of galaxies. The transition between atomic and molecular medium is typically below 40 K. It is often distributed in gravitationally bound clouds called GMCs (giant molecular clouds) that show a complex structure, with clumpiness at various scales and strong turbulence (see section 1.2.2). The molecular gas is mainly concentrated in the inner regions and on the spiral arms of galaxies (figure 1.3), and may be correlated with the presence of the bar in barred spirals (Omont 2007 and references therein). Roughly half of the ISM mass of the Milky Way galaxy is in molecular form (the other half being neutral atomic).

Molecules are observed mainly via their rotational emission lines. For linear molecules (i.e. molecules where the atoms are aligned) like CO and H_2 the energy required for a transition is given by quantum mechanics:

$$E_{rot} = \frac{h^2}{8\pi^2 I} J(J+1) \quad \text{with} \quad J = 0, 1, 2, ... \tag{1.1.1}$$

where $h = 6.626 \times 10^{-27}$ erg s is the Planck constant and I is the moment of inertia of the molecule (Dyson et al. 1997). The selection rule is $\Delta J = \pm 1$ if the molecule has a dipole moment, otherwise the emission has $\Delta J = \pm 2$ via electric quadrupole

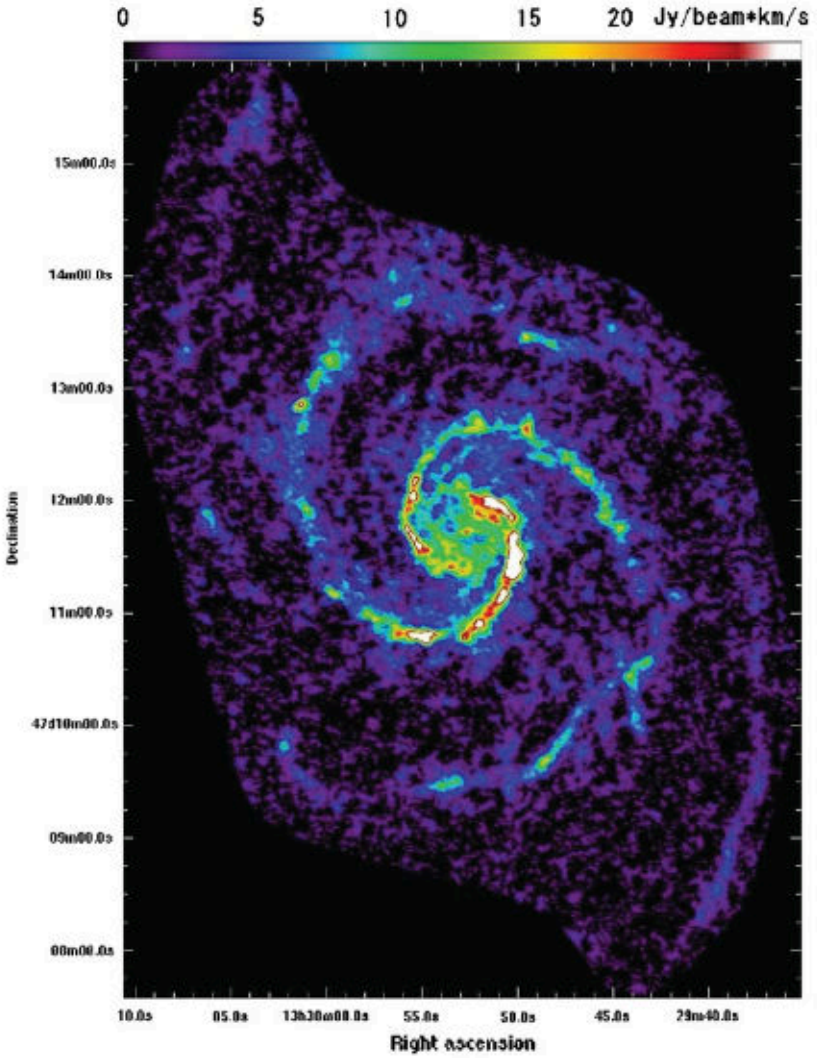

Figure 1.3: CO $J = 1 - 0$ map of M51 galaxy, with combined data from CARMA (Combined Array for Research in Millimeter Astronomy) interferometer, located in the Californian Inyo Mountains, and the Japanese Nobeyama 45-m telescope. The molecular gas is concentrated at the center and on the spiral arms of the galaxy. Taken from Koda et al. 2009, figure 1a.

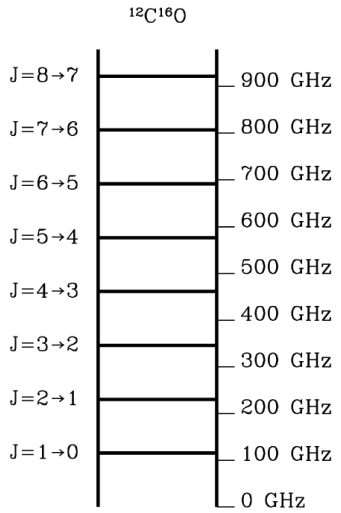

Figure 1.4: The molecular rotational spectrum of a linear molecule like CO looks like a ladder (from which the name CO ladder), because the lines are equidistant having to follow the equation 1.1.1. Taken from http://www.cv.nrao.edu/course/astr534/MolecularSpectra.html

interactions. H_2 molecule, because it is not polar, has zero dipole moment, and the lowest-energy permitted quadrupole rotational transition ($J = 2 - 0$) is rarely observed because of the high lifetime of $J = 2$ level (3×10^{10} s) compared to typical timescales between molecular collisions (10^5 $n[\mathrm{cm}^{-3}]$ s).

CO molecule (in this thesis we will always intend, with CO, the $^{12}C^{16}O$ molecule), indeed, has a dipole moment, and its $J = 1 - 0$ transition has an excitation temperature $T = E_{rot}/k_B$ equivalent to 5.5 K. CO is the most abundant molecule after H_2 with $n(\mathrm{CO}) \approx 10^{-5} n(H_2)$, and it is the most observed interstellar molecule since the work of Wilson et al. 1970.

In table 1.1 the first 13 CO rotational transitions are listed with their excitation temperatures, line frequencies, Einstein A coefficients and critical densities. The Einstein A coefficient is the rate (in units of s^{-1}) at which a $\Delta J = -1$ transition spontaneously occurs, while the critical density $n_{crit} \approx A/(\sigma v)$ is the ratio between spontaneous radiative decay (represented by the A coefficient) and collisional depopulation (σv, where $\sigma \sim 10^{-15}$ cm^2 is the collisional cross section and $v \approx \sqrt{3k_B T/m}$ is the mean molecular velocity) of a quantum level. If the density is greater than the critical density (which is unique per every molecule, transition and local temperature) then radiative cooling (with *cooling* is intended loss of energy, in this case via photon emission) is favoured to collisional deexcitation.

It is important to note that the critical densities listed in table 1.1 are only valid for *optically thin* lines: these are the lines whose photons have a little probability of being scattered or absorbed while traveling through a gas cloud. Conversely, CO transitions are *optically thick*, so the observed emitting CO molecules (from a molecular cloud, for

instance) are only the ones at the cloud surface nearest to the observer, and all the photons below a little shell on the surface are absorbed or scattered within the cloud, like what happens in stars. Computing the effective densities at which transitions become to emerge from a certain cloud is not simple and involves the use of a radiative transfer code (see Shirley 2015 for details). The rising trend in critical densities shown in table 1.1, however, is valid also in more complex treatments.

It can be shown that the Einstein coefficient A_{jk} for a given molecular radiative transition between two quantum states j and k is a function of the molecular permanent electric dipole moment μ and of the frequency corresponding to the $j-k$ transition: $A_{jk} \propto \mu^2 \nu_{jk}^3$. The value of μ_e depends on the structural properties of the molecule, and in the case of CO is $\mu_{CO} = 0.11D$ (where D is the symbol of debye units, with $1D = 10^{-18}$ statC cm). Molecules with an higher μ_e are natural tracers of denser gas, because they tend to have a greater critical density: HCN, for instance, is one of the most used tracer for the densest part of molecular gas (Gao et al. 2004b) mostly thanks to its high dipole moment, which is $\mu_{HCN} = 2.99D$ (Shirley 2015).

Transition	T [K]	λ [μm]	ν [GHz]	A [s^{-1}]	n_{crit} [cm^{-3}]
$J = 1-0$	5.5	2600.85	115.27	7.2×10^{-8}	6.5×10^{2}
$J = 2-1$	11.1	1300.43	230.54	6.9×10^{-7}	6.2×10^{3}
$J = 3-2$	16.6	866.98	345.80	2.5×10^{-6}	2.2×10^{4}
$J = 4-3$	22.1	650.27	461.04	6.1×10^{-6}	5.5×10^{4}
$J = 5-4$	27.7	520.24	576.27	1.2×10^{-5}	1.1×10^{5}
$J = 6-5$	33.2	433.57	691.47	2.1×10^{-5}	1.9×10^{5}
$J = 7-6$	38.7	371.66	806.65	3.4×10^{-5}	3.1×10^{5}
$J = 8-7$	44.3	325.23	921.80	5.2×10^{-5}	4.7×10^{5}
$J = 9-8$	49.8	289.13	1036.91	7.4×10^{-5}	6.7×10^{5}
$J = 10-9$	55.3	260.24	1151.99	1.0×10^{-4}	9.2×10^{5}
$J = 11-10$	60.8	236.62	1267.01	1.4×10^{-4}	1.2×10^{6}
$J = 12-11$	66.4	216.93	1381.96	1.8×10^{-4}	1.6×10^{6}
$J = 13-12$	71.9	200.27	1496.92	2.3×10^{-4}	2.0×10^{6}

Table 1.1: First 13 CO rotational transitions. Columns are: transition excitation temperature ($T = E_{rot}/k_B$), emission line wavelength (λ) and frequency (ν), Einstein A coefficient for spontaneous emission, critical density calculated as $n_{crit} = A/(\sigma v)$ with $\sigma = 10^{-15}$ cm^2, $v = \sqrt{3k_BT/m}$, $m = 2m_p$ and $T = 100$ K.

1.2 Physics and processes in molecular ISM

1.2.1 Formation of molecules

Molecules are not a byproduct of big bang nucleosynthesis nor of stars nuclei, and forming them via collisions between atoms is really difficult: the probability of such a formation channel is $\geq 10^{-5}$ per collision. Reactions between ions and molecules, conversely, proceed rapidly, thanks to the induced electric dipole in H_2 in reactions like

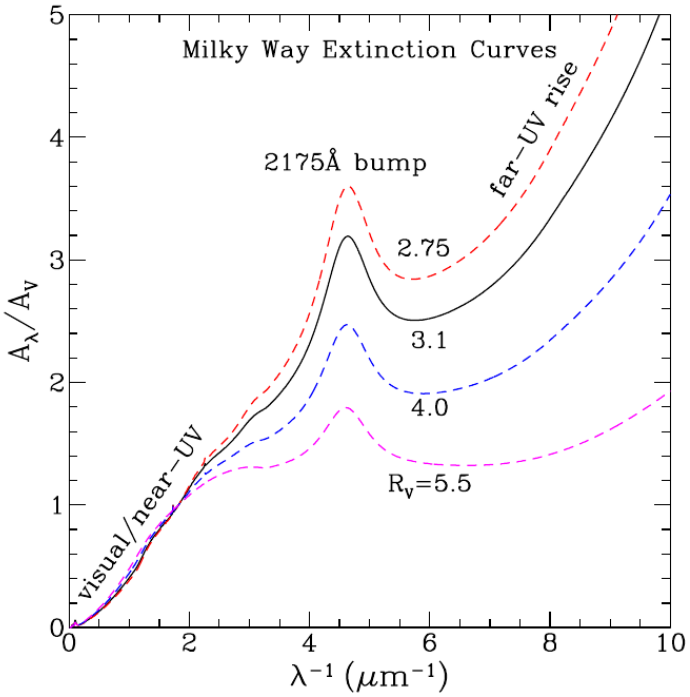

Figure 1.5: Interstellar extinction curves of the Milky Way with different values for $R_V \equiv A_V/(A_B - A_V)$*, reflecting different galactic environments: lower-density regions have a smaller* R_V*, whilst denser regions have it larger. The average value for the Milky Way is* $R_V = 3.1$*. Taken from Li 2007, figure 1.*

$O^+ + H_2 \rightarrow OH^+ + H$; these ions can be produced in the depth of molecular clouds by collisions between H or H_2 and *cosmic rays*, i.e. high-velocity charged particles (nuclei and electrons) accelerated by supernovae or active galactic nuclei (AGN, see section 1.3.2). Anyway, for this reactions channel to be open it needs the pre-existence of interstellar molecules.

The solution resides in the existence of small grains formed in the outflowing gas from cool giant stars: the interstellar dust. In figure 1.5 is shown one of the major effects of interstellar dust (and one of the causes for its discovery as well), namely the extinction curve of the Milky Way. The extinction depends on grains composition and size: the visual part of figure 1.5 is caused by large grains (with size $a \geq 0.1$ μm), while the far-UV rise by smaller grains ($a \leq 0.02$ μm); the ubiquitous 2175 Å bump is probably due to graphite (the main dust material together with silicates) grains with $a \sim 0.01$ μm (Mathis et al. 1977).

Interstellar dust grains act as a third body in the encounter of two atoms: while one H atom is retained bound to the grain surface, thanks to van der Waals forces caused by all the atoms of the grain, a second H atom arrives and a H_2 molecule can form. Once H_2 is formed, CO may emerge from chain reactions like $C^+ + H_2 \rightarrow CH^+ + H$ (Indriolo et al. 2010) followed by $CH^+ + O \rightarrow CO + H^+$ (Arshutkin 1985).

Dust is also important in shielding the molecules from UV radiation, as grains are

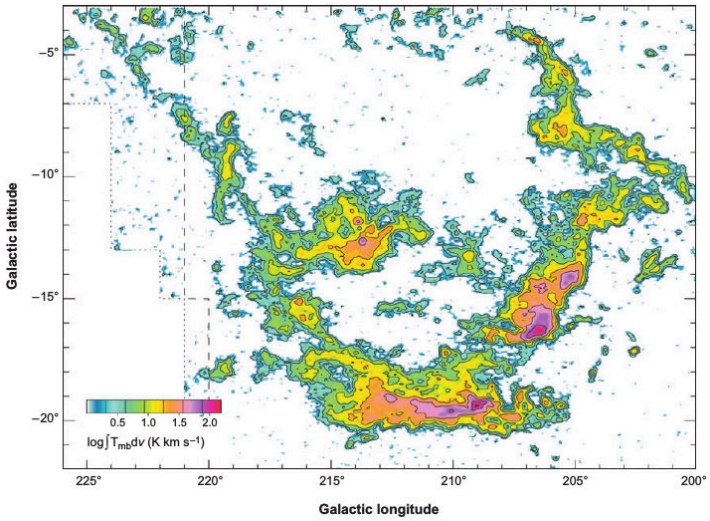

Figure 1.6: Integrated CO $J = 1 - 0$ map of the Orion-Monoceros region, in the Milky Way. The total gas mass is few $\times 10^5$ $M_\odot$. Angular size of 1° corresponds to ≈ 8 pc. Taken from McKee et al. 2007, figure 1.

very effective absorbers of such photons; actually the exposition to a mild UV radiation field can trigger the production, on the grains surface, of very complex molecules like fullerene (Cami et al. 2010). Dust grains re-radiate the UV absorbed energy as grey bodies in the IR (i.e. infrared) band: it is possible to see the emission of the whole dust population of a galaxy in the IR part of its SED, like depicted (actually for an AGN dusty torus but the mechanism is the same) in figure 1.15.

1.2.2 Molecular clouds

In a typical star-forming galaxy (like the Milky Way for instance) most of the molecular mass is in large ($\sim$ 50 pc) structures called *giant molecular clouds* (GMCs), with typical parameters $M \sim 10^5$ $M_\odot$, $n \sim 10^2$ cm^{-3}. Inwardly these clouds have a hierarchical structure, with overdense regions termed *clumps* ($M \sim 10^3$ $M_\odot$, $n \sim 10^3$ cm^{-3}), out of which stellar clusters form. Individual stars form in denser ($n \sim 10^4$ cm^{-3}) sub-pc clouds called *cores* (McKee et al. 2007).

The molecular mass is mainly inferred using the luminosity of the ^{12}CO $J = 1-0$ line. This line is optically thick (see section 1.1.3 for details) so its intensity is not linearly correlated to the number of CO atoms: this is the reason for which a conversion factor is needed. This is called *X-factor* ($X_{CO} \equiv N(H_2)/I_{CO}$, where I_{CO} is the CO $J = 1-0$ line intensity, typically in units of K km s^{-1}, and $N(\mathrm{H_2})$ the $\mathrm{H_2}$ column density in cm^{-2}) and have to be calibrated: one method is to infer the total gas mass from the observation of γ rays emitted in the interactions between cosmic rays and the ISM, and then subtracting the known HI mass (A. W. Strong et al. 1996 and others have found $X_{CO} \approx 2 \times 10^{20}$ cm^{-2} (K km s^{-1})$^{-1}$ with this technique); another method, exploitable only for nearby molecular clouds, is to use the extinction maps of dark clouds in the near-IR (Lada,

Lombardi, et al. 2010).

In starburst galaxies (galaxies with high levels of star formation, described in section 1.3.1) a lower X_{CO} value is expected, mainly due to the higher temperature of the gas that increases I_{CO}; the standard adopted value in this case is $X_{CO} = 0.4 \times 10^{20}$ cm^{-2} (K km s^{-1})$^{-1}$ (Bolatto et al. 2013).

Once adopted a value for X_{CO} the molecular mass is given by:

$$M_{mol} = 1.05 \times 10^4 \left(\frac{X_{CO}}{2 \times 10^{20} \text{cm}^{-2} (\text{K km s}^{-1})^{-1}} \right) \frac{S_{CO} \Delta v D_{Mpc}^2}{(1+z)} \tag{1.2.1}$$

where $S_{CO}\Delta v$ is the integrated line flux density in Jy km s^{-1}, D_{Mpc} is the luminosity distance in Mpc and z is the redshift (Bolatto et al. 2013).

Spectroscopic observations have revealed that the molecular medium (but the same is true also for other ISM phases) is randomly moving at a speed ~ 10 times greater than its thermal speed. Moreover, the observed line widths σ_{obs} strongly correlate with the size L of the clouds: this is called first *Larson law*, from Larson 1981, and has the form of a power-law $\sigma_{obs} \propto L^{\alpha}$, with $\alpha \simeq 0.4$.

These are the main evidences of the presence of turbulence, which is often described as an irregular state of motion characterized by vortices or *eddies* on several scales: this apparent chaos actually imposes a structure to the gas motion, as seen in the Larson law. Kolmogorov classic theory (1941) and more recent numerical simulations (see McKee et al. 2007 and references therein for details) have shown that supersonic turbulence, i.e. when the RMS[2] turbulent velocity is greater of the sound speed, imposes a log-normal distribution[3] of gas density: this is called density probability distribution function (PDF)

$$f(x)dx = \frac{1}{\sqrt{2\pi\sigma_x^2}} \exp\left[-\frac{1}{2} \left(\frac{x - x_0}{\sigma_x} \right)^2 \right] dx \tag{1.2.2}$$

where $x \equiv \ln(\rho/\rho_0)$ and $x_0 = \sigma_x^2/2$ (Vallini et al. 2017). In figure 1.6 is possible to see a Galactic example of such a complex density structure.

1.2.3 Photo-dissociation regions

Photo-dissociation regions (PDRs, sometimes also called photon-dominated regions) are the transition regions between the fully ionized and fully molecular zones. In this

[2]The RMS (Root Mean Square) of a set of n values is $x_{rms} = \sqrt{\frac{1}{n}(x_1^2 + x_2^2 + ... + x_n^2)}$, while for a continuous distribution function $f(y)$ (e.g. the velocity field) is $f_{rms} = \sqrt{\frac{1}{y_2 - y_1} \int_{y_1}^{y_2} [f(y)]^2 dy}$

[3]Actually this is the simplest approach to the problem of the density structure imposed by turbulence, but it seems to be a valid assumption when self-gravity is unimportant and both with and without a magnetic field.

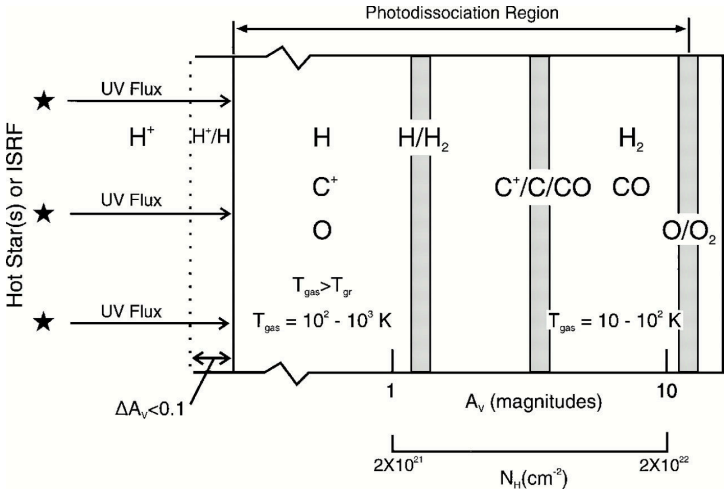

Figure 1.7: Section of a PDR, with depth measured with A_V extinction. On the left side the UV source ionize hydrogen until the beginning of the PDR. Sharp transition regions are highlighted. Taken from Hollenbach et al. 1997, figure 3.

regions the photons with energy $h\nu < 13.6$ eV penetrate, while the ones with $h\nu > 13.6$ eV have been absorbed within the Strömgren sphere (see section 1.1). These photons could come from a nearby star or from the interstellar radiation field (ISRF). Of our interest is the FUV band, i.e the photons with $6 < h\nu[\text{eV}] < 13.6$: these are the photons able to photodissociate the molecular hydrogen. The FUV flux is often called G_0 and is normalized to 1.6×10^{-3} erg s^{-1} cm^{-2}, which is the average local interstellar flux (Habing 1968). The incident FUV flux G_0 and the gas density n are the main two variables in modeling a PDR.

The FUV photons are mainly generated on the surface of hot stars, mainly of O, B and A spectral classes. These stars have a surface temperature respectively of 3, 1.5 and 0.9×10^4 K (Karttunen et al. 2007); with these numbers is possible to calculate for each star class the fraction of the luminosity within a certain frequency band over the *bolometric* (i.e. over the whole energy spectrum) luminosity:

$$\frac{L_{\nu_1-\nu_2}}{L_{tot}} = \frac{15}{\pi^4} \int_{x_1}^{x_2} \frac{x^3}{e^x - 1} dx \tag{1.2.3}$$

where we have defined $x \equiv h\nu/(kT)$, and x_1 and x_2 correspond to ν_1 and ν_2. With the FUV range ($h\nu_1 = 6$ eV and $\nu_2 = 13.6$ eV) the fractions are respectively 54%, 29% and 5% of total luminosity of O, B and A stars. Therefore these three stellar classes, especially O and B, are the main emitters of FUV radiation within a galaxy, if we do not consider the AGN (sections 1.2.4 and 1.3.2).

When describing the interiors of clouds it is more meaningful, instead of depth, to use the column density (N_H, in units of cm^{-2}, is the number of H nuclei within a cilinder of top area 1 cm^2) or the visual extinction ($A_V = 1$ mag corresponds to $N_H = 2.2 \times 10^{21}$ cm^{-2} for a standard extinction curve $R_V = 3.1$, Güver et al. 2009) as we go deeper inside. In figures 1.7 and 1.8 are shown schematic diagrams of a PDR. Radiation come from stars or the ISRF, ionizing hydrogen until the beginning of the PDR; then a first

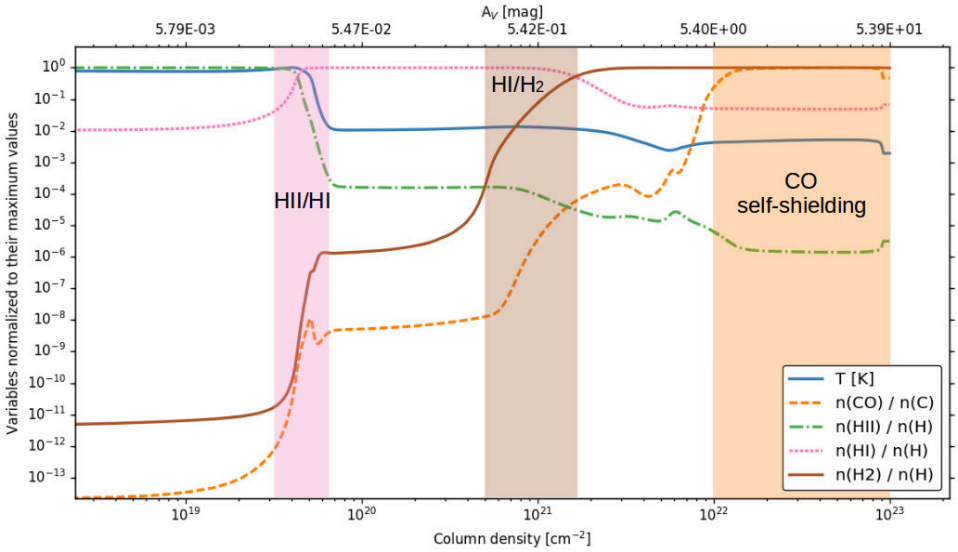

Figure 1.8: PDR model computed with CLOUDY *code (section 3.1.1). The lines represent the gas temperature, the CO fraction relative to C and the ionized, neutral atomic and molecular (only in H_2 molecule) hydrogen relative to total hydrogen density (defined in equation 3.1.3). Every variable is normalized to its maximum value among the column densities (or visual extinctions) range; for the temperature the maximum value is 8.3×10^3 K. Transition between the different phases of hydrogen are highlighted.*

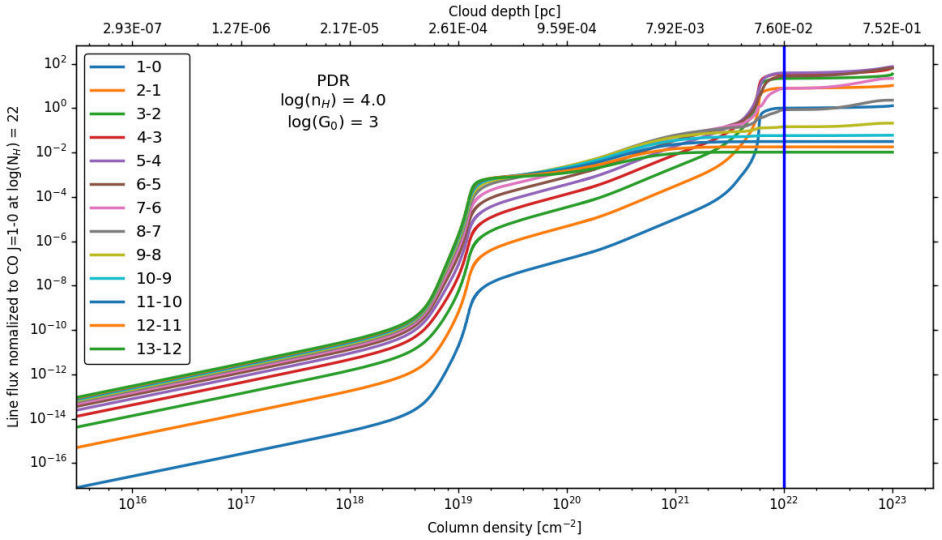

Figure 1.9: PDR model computed with CLOUDY *code (section 3.1.1). Every colored line is one of the CO rotational lines listed in table 1.1. The fluxes are normalized to the CO $J = 1 - 0$ flux measured at $N_H = 10^{22}$ cm^{-2}. This column density value is the one adopted among the simulations (section 3.1.3).*

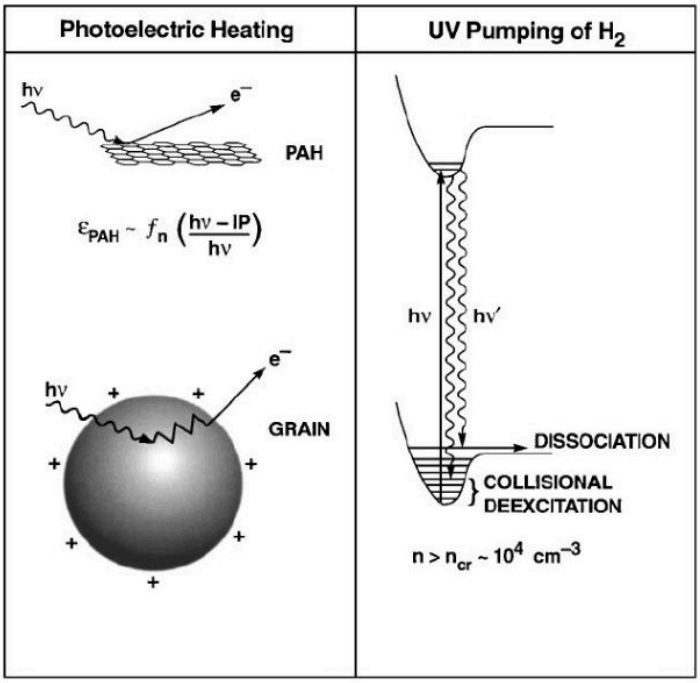

Figure 1.10: The two main heating mechanisms in PDRs. On the left is photoelectric heating of PAHs and dust grains, on the right UV pumping and photo-dissociation of H_2. See section 1.2.3 for details. Taken from Hollenbach et al. 1997, figure 6.

layer, characterized by atomic hydrogen and ionized carbon (the first ionization energy of carbon is 11.3 eV), followed by the sharp transition between atomic and molecular H (at $N_H \sim 2 - 4 \times 10^{21}$ cm^{-2}) and by the one between ionized carbon and neutral atomic or molecular in CO (around $4 - 8 \times 10^{21}$ cm^{-2}). The PDR layers are mantained by the FUV photons penetration, that photodissociate molecules and photoionize carbon (Hollenbach et al. 1997). In our simulations (figure 1.8), indeed, the transitions between HII and HI and between HI and H_2 are quite distinct.

Deeper than 10^{22} cm^{-2} (that is $A_V \approx 5$ mag) the CO is essentially self-shielded against FUV radiation, and the CO SLED should saturate with cloud depth, as shown in figures 1.8 and 1.9; some simulations made with the CLOUDY code (section 3.1), however, showed some deviation from this behaviour.

Photodissociation of H_2 consists in the absorption of FUV photons in the Lyman-Werner bands (between 11.2 and 13.6 eV): Lyman (B) and Werner (C) are the first two excited electronic levels of H_2 (the ground state is called X). The molecule then goes to vibrational excited levels of the electronic ground state X emitting a photon, hence it is collisionaly de-excited and heats the gas; however, in about $10 - 15\%$ of the cases, the molecule goes to the vibrational continuum of the ground electronic state, which leads to H_2 photodissociation (Hollenbach et al. 1997).

The other main source of heating in PDRs is photoelectric heating of dust by FUV photons: an electron is extracted from a grain via photoelectric effect, then it yields its

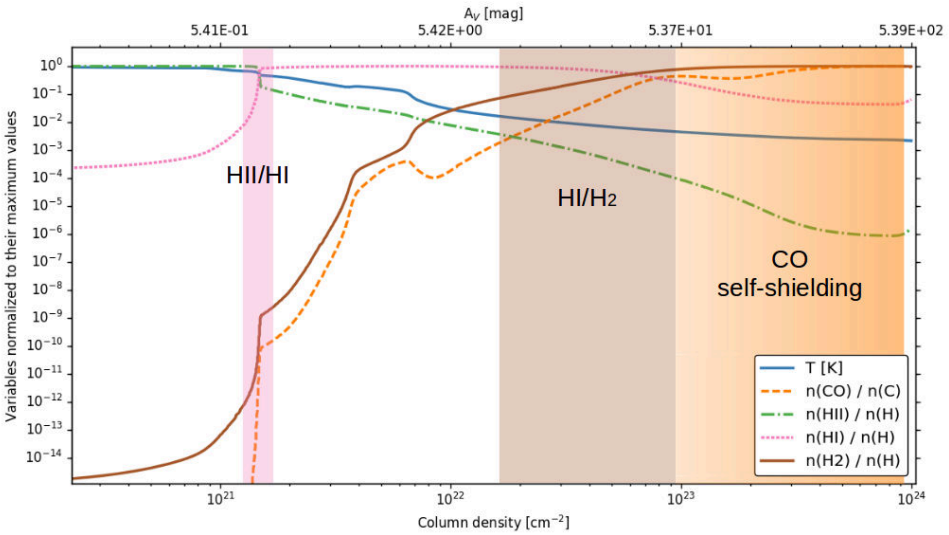

Figure 1.11: XDR model computed with CLOUDY *code (section 3.1.1). The lines represent the gas temperature, the CO fraction relative to C and the ionized, neutral atomic and molecular (only in H_2 molecule) hydrogen relative to total hydrogen density (defined in equation 3.1.3). Every variable is normalized to its maximum value among the column densities (or visual extinctions) range; for the temperature the maximum value is 2×10^4 K. Transition between the different phases of hydrogen are highlighted. Compared to PDR (see figure 1.11), in XDR the H_2 and CO fractions saturate together at $N_H \approx 10^{23}$ cm^{-2}; another difference is that the temperature here drops gently, while in PDR model a sharp fall in T overlapped to the HII-HI transition.*

excess energy to the ISM via collisions. Theoretical calculations (Hollenbach et al. 1997) show that the most effective heating agents are PAHs and small (< 50 Å) grains. Figure 1.10 reassumes these two heating mechanisms.

1.2.4 X-ray dissociation regions

XDRs, i.e. X-ray dissociation (or dominated) regions, are the gas regions in which hard-X photons ($1 < h\nu[\text{keV}] < 100$) penetrate and dissociate molecules like H_2 or CO. The X-ray photons are able to penetrate deeper in a molecular cloud compared to FUV photons (section 1.2.3), so the XDR survives at optical depths greater than 10^{22} cm^{-2}; CO self-shielding, as shown in figure 1.12, becomes important at $N_H \approx 10^{23}$ cm^{-2}.

The X-ray sources could be X-ray binaries, supernovae remnants or an active galactic nucleus, i.e. a complex structure that surrounds the supermassive black hole that is thought to exist at the center of every galaxy. In this thesis we will put emphasis only on the AGN emission, described in section 1.3.2.

The two most important physical variables in XDR modeling are the gas density n

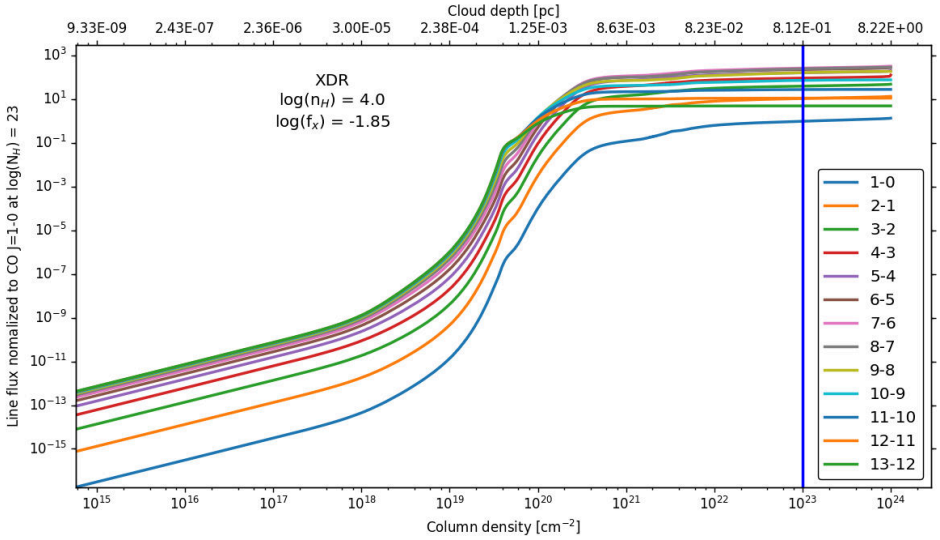

Figure 1.12: XDR model computed with CLOUDY *code (section 3.1.1). Every colored line is one of the CO rotational lines listed in table 1.1. The fluxes are normalized to the CO $J = 1 - 0$ flux measured at $N_H = 10^{23}$ cm^{-2}. This column density value is the one adopted among the simulations (section 3.1.4).*

and the local X-ray deposition rate per particle H_X, given by:

$$H_X = \int_{E_{min}}^{E_{max}} \sigma_{pa}(E) F(E) dE \tag{1.2.4}$$

where $\sigma_{pa}(E)$ is the photoelectric cross section per hydrogen nucleus and $F(E)$ the local photon energy flux per unit energy interval.

The X-ray photons ($0.1 < h\nu[\text{keV}] < 100$) ionize the ISM producing photoelectrons (via photoelectric effect) with energy $\sim$ keV: this is the *primary ionization*. However it is the secondary ionization that dominates the hydrogen ionization rate, both in neutral atomic and molecular medium (Maloney et al. 1996). Figure 1.13 summarizes the loss routes for energetic photoelectrons in XDR. In case of ionized gas (high X_e) the photoelectrons heat the gas via Coulomb interactions with ISM free electrons.

Deeper in the XDR the gas is mainly neutral, and the primary photoelectrons energy is spent indeed in ionization and excitation of the ISM (figure 1.13). In the fully molecular gas, the ionization of H_2 results in the reaction $H_2^+ + H_2 \rightarrow H_3^+ + H$, which may lead to other such reactions, and eventually the remaining molecular ion will dissociatively recombine with a free electron, so that much of the original ionization energy is transformed in kinetic energy of the reaction products. If the gas is partly atomic, also the reaction $H_2^+ + H \rightarrow H_2 + H^+$ is important, and the ending is the same.

The larger fraction (close to 50%) of the photoelectrons energy goes into collisional excitation: principally electronic excitations of H and electronic, vibrational, and rotational excitations of H_2 (Maloney et al. 1996 and references therein).

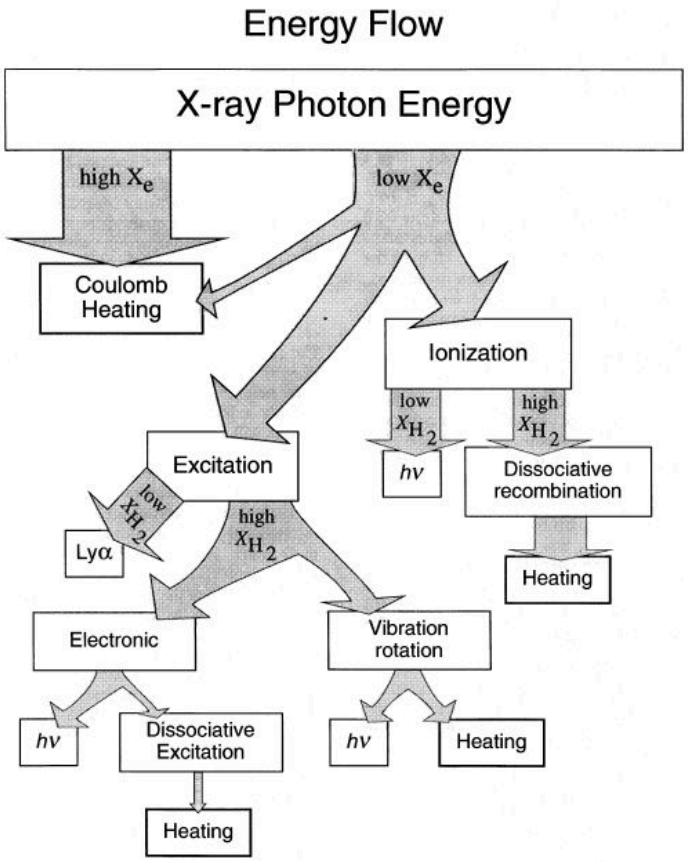

Figure 1.13: Flow chart showing the yields of interactions between photoelectrons produced by X-ray (primary ionization) and the ISM in a XDR. The arrows widths represent the probabilities of the sundry processes. X_e and X_{H_2} are respectively the electrion and molecular hydrogen fractions. See section 1.2.4 for details. Taken from Maloney et al. 1996, figure 2.

1.3 Star formation and AGN feedback

From the epoch of the formation of the first stars, galaxies and supermassive black holes, the interstellar medium has continuously renewed its chemistry and dynamics through feedback from its products. Keeping a galaxy isolated from the intergalactic medium (IGM) and other galaxies or cluster of galaxies (like in the so-called *closed box* model), the major events that shape the ISM are stars (from the formation process to phenomena like planetary nebulae, stellar winds and supernovae) and, if present, an active galactic nucleus.

1.3.1 Star formation

A star is a gaseous sphere in hydrostatic equilibrium (i.e. where the gravity that keeps the gas towards the interior is balanced by the pressure that pulls it outward) that emits a spectrum of radiation that can be approximated to a black body, so with a frequency distribution of photons that follows the Planck law:

$$B_\nu(T)\, d\nu = \frac{2h\nu^3}{c^2} \frac{1}{e^{h\nu/kT} - 1}\, d\nu \tag{1.3.1}$$

The great advantage of using this law is that the *color* of a star depends only on the temperature T of the surface of the star.

Stars born in groups from the collapse of dense clumps in the giant molecular clouds (section 1.2.2), so the majority of the star formation for a galaxy is situated in the nuclear region and on the spiral arms (see figure 1.3). The way in which the newborn stars masses are distributed is called *initial mass function* (IMF), and there is an ongoing research for understanding if there is a valid universal model for the IMF. The most famous and used one is the Salpeter model, $\phi(M)dM = M^{-s}$ with index $s = 2.35$ (Salpeter 1955), while more recent works indicate a flattening of the power law at low masses.

The star formation rate (SFR) is the measure of the newborn stars per unit time and is tipically measured in $M_\odot$/yr. In principle the only way to derive it directly is to count the number of young stellar objects (YSOs) within the region of interest: unfortunately this is only possible for the Milky Way and the Magellanic Clouds (Kennicutt and Evans 2012). The most common way to infer the SFR of a galaxy is to assume that young stars affect a certain observable luminosity, like the IR luminosity (due to the cooling of dust heated by stellar radiation, see section 1.2.1) or the Hα luminosity (from HII regions around hot stars, see section 1.1.1). Kennicutt and Evans 2012 give a review of the conversion factors between these luminosities and SFRs.

The SFR of a galaxy seems to be correlated to its content of cold gas; this was the assumption in the work of Schmidt 1959, and has been studied in deep in the next half century by a multitude of authors. A good review of this research field is Kennicutt

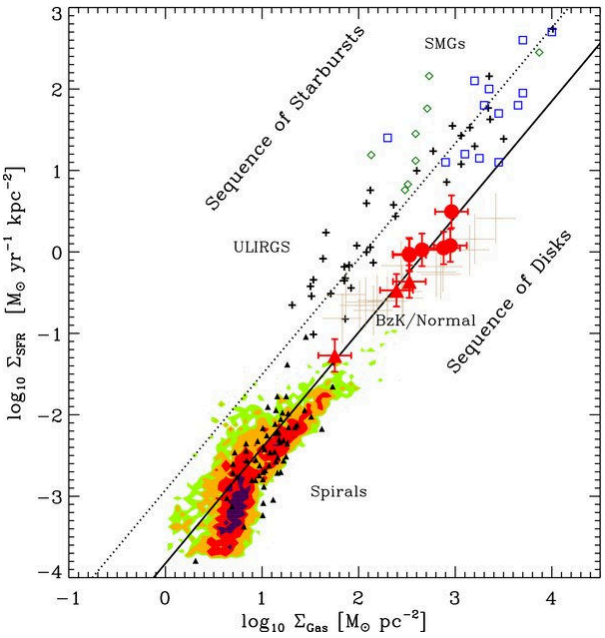

Figure 1.14: Taken from Daddi et al. 2010, figure 2.

and Evans 2012. The main idea is that the star formation rate surface density (Σ_{SFR}, in units of $M_\odot$ yr^{-1} pc^{-2}) follows the gas surface density (Σ_g) with a power-law $\Sigma_{SFR} \propto \Sigma_g^N$ with a index between 1 and 2.

Daddi et al. 2010 argue that indeed two power-laws are needed to reproduce the observed star formation and gas densities: one for normal star-forming disk galaxies, that stand on the so-called *main sequence* of star-forming galaxies, the other, with the same slope but higher normalization, for starburst galaxies (figure 1.14). The slope they found is 1.4, the same as Kennicutt 1998.

Starburst galaxies are galaxies with a very high SFR, typically $\geq 10\ M_\odot\ yr^{-1}$ (Carroll et al. 2007). These galaxies are not so bright in the optical part of the spectrum, since most of their stellar radiation is absorbed by large quantities of gas and dust, that re-emit it mainly at IR wavelengths. If the infrared luminosity L_{IR}, measured between 8 and 1000 μm, is $L_{IR} > 10^{11} L_\odot$ (where $L_\odot = 3.9 \times 10^{33}$ erg s^{-1}), it is defined as a luminous infrared galaxy (LIRG, Sanders and Mirabel 1996); if $L_{IR} > 10^{12} L_\odot$ it is called a ultra-luminous infrared galaxy (ULIRG).

If we divide the galaxies according to their IR luminosity, what we see is that the fraction of interacting or merging galaxies increases with it, reaching the 95% of the cases for $L_{IR} > 10^{12} L_\odot$ (Sanders and Mirabel 1996). Numerical simulations show that mergers between gas-rich galaxies can lead to high nuclear concentrations of gas; it is rather difficult to understand from a theoretical point of view if this gas reservoir can be used to fuel star formation activity.

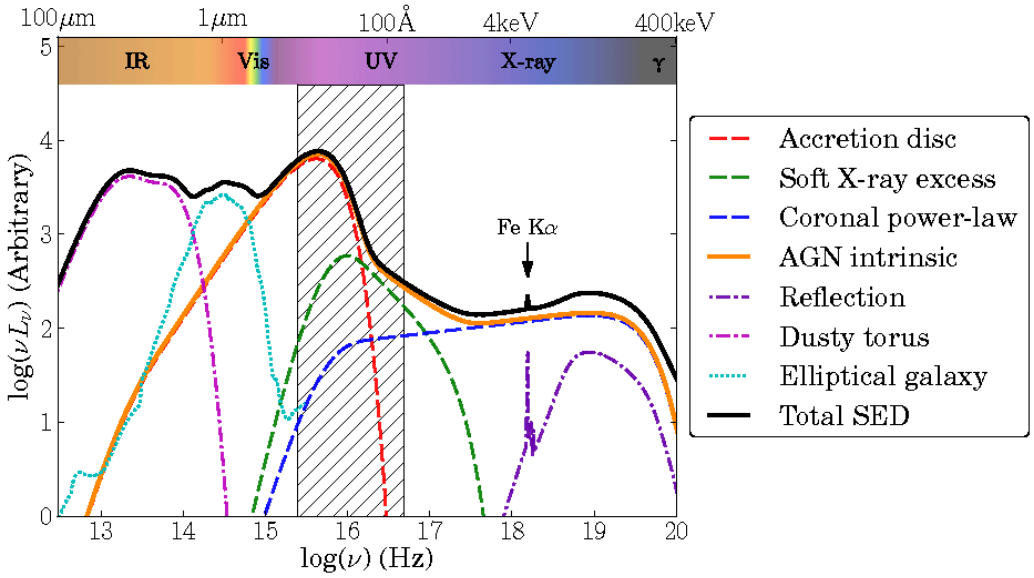

Figure 1.15: A typical AGN SED broken into its different components (including an elliptical host galaxy). The highlighted region around 10^{16} Hz is the spectral range heavily obscured by IGM (intergalactic medium) absorption. Taken from Collinson et al. 2017, figure 1.

1.3.2 Active Galactic Nuclei

Active Galactic Nuclei (AGNi) are compact sources of radiation that reside at the center of $\sim$ 1% of the galaxies in the Universe. The main hypothesis for the engine that produces the emission is a supermassive black hole (SMBH, with mass $\geq 10^6$ $M_\odot$) surrounded by an accretion disk of infalling material. This disk is heated by viscosity forces and emit black body radiation (indeed a sum of black bodies if the disk temperature is a function of radius).

The AGN typical SED (in figure 1.15) shows how complex the physical understanding of these kind of objects could be, involving a hot gaseous corona standing over the accretion disk, a surrounding dusty torus and other even more exotic components. To make matters worse, $\sim$ 1% of the AGN population show even radio jets, made of charged particles thrown from the AGN at velocities that graze the speed of light.

Over the last century a great variety of different names have emerged to describe the observed AGNi, depending on the observed band or the luminosity or to other properties: quasars, QSOs, radio galaxies, Seyfert galaxies, LINERs, Blazars are only the most famous ones. Here we describe only the ones important for our work, based upon the sample of galaxies described in section 2.1.

Seyfert galaxies, named after Carl Seyfert, the first who studied these objects in 1943, have optical spectra similar to gaseous nebulae (i.e. the HII regions described in section 1.1.1), with the width of emission lines that splits this AGN class in type 1

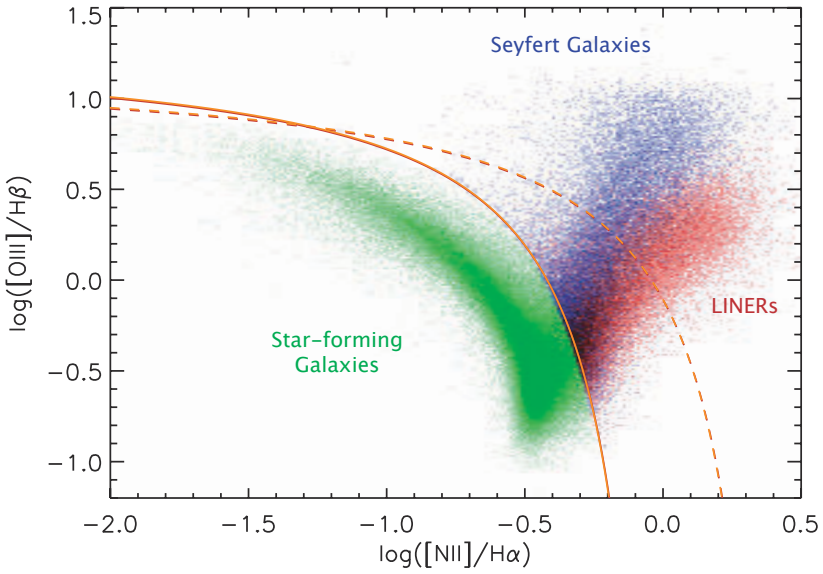

Figure 1.16: The BPT diagram is a line ratio diagnostic diagram, created by Baldwin et al. 1981. It uses the ratios between the optical lines [OIII] at 5007 Å, [NII] at 6583 Å, Hα at 6563 Å and Hβ at 4861 Å. The two lines are the empirical (solid) and theoretical (dashed) separators between star-forming galaxies (here identified by their HII regions spectrum) and AGNi, like Seyferts and LINERs. Adapted from Kewley et al. 2006.

(broad lines) and type 2 (narrow lines). The BPT diagram (from Baldwin et al. 1981) is a useful diagnostic tool for separating optical selected AGNi like Seyferts from star-forming galaxies (figure 1.16): in the former the high level of photoionization responsible for the observed lines ([OIII] and [NII]) is associated to the nuclear emission, in the latter the radiation sources are young stars.

The low-ionization nuclear emission-line regions (LINERs), defined by Heckman 1980, are a controversial type of galaxies, similar to type 2 Seyferts but with strong low-ionization lines, like [OI]. It is a matter of debate if these objects are powered by the central engine (namely the accretion disk and the hot corona), by stellar radiation, or even by shocks waves moving at ~ 100 km s^{-1} (Heckman 1980); probably they are just the extension to lower luminosities of type 2 Seyferts (Osterbrock 1991).

Despite (jets aside) all its complexity the AGN is confined in the central kpc or less of the galaxy, and despite its small size its effects are thought to be important for the whole galaxy. An indirect evidence of this consideration is the famous $M_{BH} - \sigma$ relation (Ferrarese et al. 2000 and Gebhardt et al. 2000), i.e. a correlation between the SMBH mass and the velocity dispersion (σ) of the bulge if the host galaxy is a spiral or of the entire spheroidal galaxy if the host is an ETG (figure 1.17).

The comparison of the star formation history (SFH) (Madau plot, from Madau, Pozzetti, et al. 1998) with the black hole accretion history of the Universe is even more challenging: figure 1.18 (from Madau and Dickinson 2014) shows that the cosmic evolution of star formation follows the same pattern of the massive black hole accretion rate

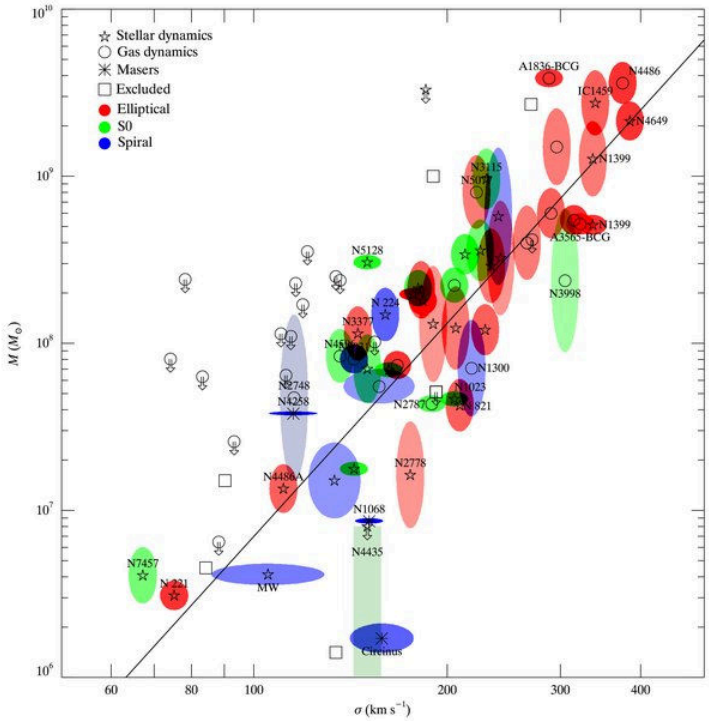

Figure 1.17: $M_{BH} - \sigma$ relation for several galaxy types. Symbols indicate the method of BH mass measurement, while color is the Hubble type, as shown in the figure legend. Taken from Gültekin et al. 2009, figure 1.

in function of redshift z or lookback time, with a peak around $z \approx 2$, corresponding to a Universe age of $3 - 4$ Gyr. The black hole accretion rate $\dot{M}$ is calculated assuming that the energy emitted by an AGN is a fraction ϵ of the mass energy mc^2 eaten by the black hole: $\dot{M} = L/(\epsilon c^2)$.

Despite the precise mechanisms of how the central black holes influence the star formation of galaxies are still matter of research, a scenario accepted by a large part of the scientific community is the one described in Hopkins et al. 2008: the authors depict a comprehensive hypothesis for the life phases of a typical gas-rich large galaxy undergoing a merger with another gas-rich large galaxy (this is called a *wet major* merger). This hypothesis, reassumed in figure 1.19, states that during a major merging, in the final coalescence of the two galaxies, the star formation rate reach a peak thanks to massive inflows of gas (starburst phase, see also section 1.3.1). During and after the starburst phase the SMBH grows rapidly, and the combined action of AGN and stellar feedback (mainly via supernovae explosions) expells the majority of dust and gas, quenching the star formation and revealing directly the AGN, a process that slowly drives the system towards the formation of a quiescent elliptic galaxy.

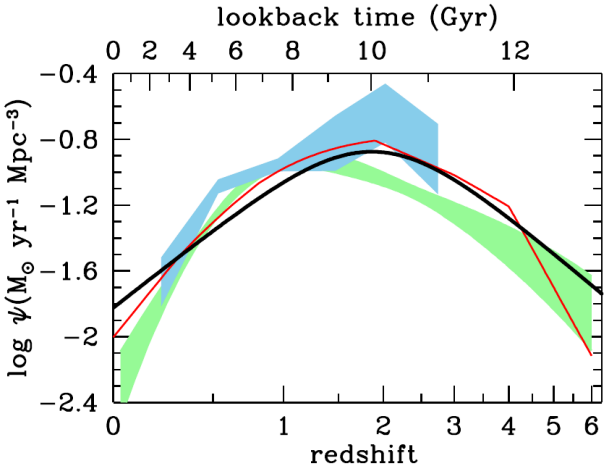

Figure 1.18: Cosmic history of star formation and AGN evolution: the thick solid line is the cosmic star formation rate density (data from Madau and Dickinson 2014), whereas the other colors are for black hole accretion rate densities, computed from X-ray (red solid line by Shankar et al. 2009 and light green shading by Aird et al. 2010) and IR data (light blue shading by Delvecchio et al. 2014). Radiative efficiency has been set to $\epsilon = 0.1$*, and the BH accretion rates have been scaled up by a factor* 3300 *for facilitating the comparison. Taken from Madau and Dickinson 2014, figure 15.*

1.4 Thesis purposes

The aim of this thesis work is to understand, on a sample of star-forming local galaxies, which is the dominant radiation field able to heat the molecular gas clouds, and in case to evaporate them. The two major agents in this sense are the population of young and hot stars (that resides in the same galactic region of those clouds, see sections 1.2.3 and 1.3.1) and, if present, the active galactic nucleus (sections 1.2.4 and 1.3.2). Shocks would have been a third important agent in that sense (Pereira-Santaella et al. 2014) but it has not been included in this work. It is known that the star formation history of a system is linked to the evolution of this cold gas reservoir, so to understand in which conditions it survives or is destroyed is a way to comprehend more about this complex organisms that are galaxies.

In order to reach the aforesaid objectives, we have selected a sample of star-forming galaxies with available molecular observed data and with some indications of AGN presence. Since H_2 is difficultly observable (section 1.1.3), our choice has fallen on the CO observations, in detail on the CO spectral line energy distribution (CO SLED), which is the distribution of the rotational lines (the first 13 lines of which are listed in table 1.1).

After the data selection and measurement, the molecular clouds responsible for the observed emission has been simulated numerically through a spectral synthesis code (CLOUDY, section 3.1.1). These simulations take as input some physical parameters of the clouds and the radiative field and give as output the resulting CO SLED, hence compared with the observations in order to find the most plausible cloud model.

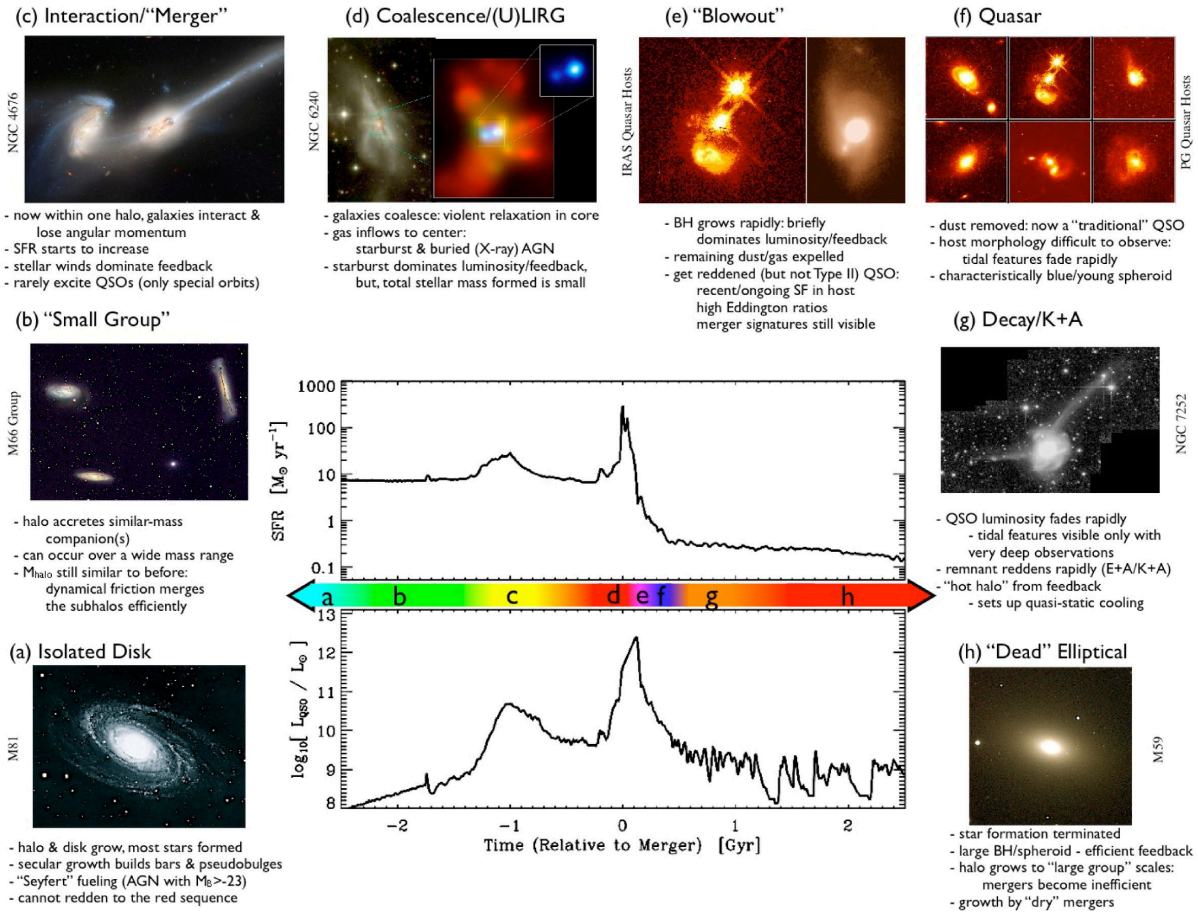

Figure 1.19: Infographics for the different phases, from left bottom (a) to right bottom (h), of formation of an elliptical galaxies from a major merger event. The central picture shows the trend of SFR and AGN luminosity as functions of time. Taken from Hopkins et al. 2008, figure 1.

Once obtained the most reliable physical parameters for the molecular clouds and its surroundings, we have tried to compare this work to other similar or concerning the same open problems.

Chapter 2

CO SLEDs observations

2.1 Sample selection

The most brilliant molecule of the Universe is the carbon monoxide (CO), studied since the works of Wilson et al. 1970 and Rickard et al. 1975. The CO rotational lines are intensively studied in infrared and sub-millimetric astronomy, given that their wavelengths go from 2.6 mm (CO $J = 1 - 0$) up to 30 μm (CO $J = 91 - 90$).

The ESA *Herschel Space Observatory*, launched on 14 May 2009 and ended on 29 April 2013 after the exhaustion of its supply of liquid helium coolant, contained several instruments operating at FIR and sub-mm frequencies (Pilbratt et al. 2010). Of particular importance for this study is the Fourier-transform spectrometer (FTS) of the Spectral and Photometric Imaging REceiver (SPIRE), operating in the spectral range $194 - 671$ μm ($447 - 1550$ GHz), accordingly able to detect CO lines from $J = 4 - 3$ (λ = 650 μm) to $J = 13 - 12$ (λ = 200 μm). The SPIRE spectrometer has a field of view approximately circular with a 2.6′ diameter and a spectral resolution between 1.2 GHz and 25 GHz (Griffin et al. 2010).

During the lifetime of *Herschel Space Observatory* an important survey has been done: the *Herschel* Comprehensive ULIRG Emission Survey (HerCULES, Rosenberg et al. 2015). This survey takes galaxies from the *IRAS* Revised Bright Galaxy Sample (Sanders, Mazzarella, et al. 2003) which satisfy the following conditions: if $L_{IR} > 10^{12} L_{\odot}$ (ULIRGs, see section 1.3.1) all sources with $S_{60} > 11.65$ Jy (S_{60} is the flux measured at 60 μm) are included, while if $10^{11} L_{\odot} < L < 10^{12} L_{\odot}$ (LIRGs, in section 1.3.1 again) all sources with $S_{60} > 16.14$ Jy are included. These criteria have selected 29 galaxies (21 LIRGs and 8 ULIRGs) for which the CO ladder (see section 1.1.3) between $J_{upp} = 4$ and $J_{upp} = 13$ has been observed by *Herschel*/SPIRE-FTS.

For this thesis we have chosen the HerCULES galaxies that had been observed, at CO frequencies, also by the Atacama Large Millimeter/submillimeter Array (ALMA). The

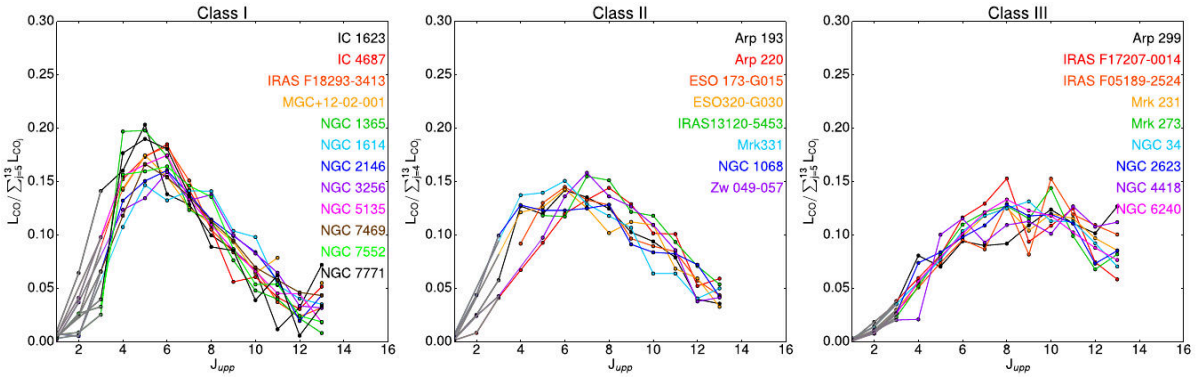

Figure 2.1: The three classes defined by Rosenberg et al. 2015 with equation 2.1.1 are shown. Galaxies have been divided by the authors in the 3 classes on the basis of equation 2.1.1. Figure taken from Rosenberg et al. 2015, figure 4.

high spatial resolution (up to 5×10^{-3} arcsec at $\nu = 900$ GHz) of ALMA observations allows to infer the size of the CO emitting region. Of the 29 HerCULES galaxies, only 17 are available up to now in the ALMA archive.

As studies have shown, the typical starburst CO SLED is characterized by an increase of luminosity up to the CO $J = 5-4$ transition, followed by a net decrease going towards the highest J. Galaxies with AGN, conversely, show a flatten CO SLED. Given the goal of the thesis we decided to focus on HerCULES galaxies with a flat CO SLED, defined in Rosenberg et al. 2015 as class III galaxies (see figure 2.1), following this definition:

$$\alpha = \frac{L_{11-10} + L_{12-11} + L_{13-12}}{L_{5-4} + L_{6-5} + L_{7-6}} \Rightarrow \begin{cases} \alpha < 0.33 & \rightarrow \quad \text{class I} \\ 0.33 < \alpha < 0.66 & \rightarrow \quad \text{class II} \\ \alpha > 0.66 & \rightarrow \quad \text{class III} \end{cases} \tag{2.1.1}$$

where L_{b-a} is the luminosity of CO $J = b - a$ line.

The final sample, after all these restrictions, is made of 4 class III galaxies: IRAS F05189−2524, NGC 34, NGC 4418 and NGC 6240. They are listed in table 2.1 with redshift, luminosity distance, type (see section 1.3.2), coordinates, infrared and hard-X luminosity and SFR.

2.2 The HerCULES CO SLEDs

All the informations and data about HerCULES, in this section and elsewhere in this essay, are taken from Rosenberg et al. 2015. The CO lines from $J = 4 - 3$ to $J = 13-12$ have been observed with the SPIRE spectrometer, using a beam size varying from $17'' - 42''$ and the higher possible spectral resolution (1.2 GHz). CO line fluxes have

Galaxy	IRAS F05189−2524	NGC 34	NGC 4418	NGC 6240
z	0.04256	0.01962	0.007268	0.02448
D_L [Mpc]	187	84.1	36.5	116
Type	QSO	SB	Sy2	SB, AGN
$\log L_{IR}$	45.75	45.08	44.78	45.52
$\log L_X$	44.17	41.98	–	43.39
SFR [$M_\odot$ yr^{-1}]	220	50	20	130

Table 2.1: Sample of galaxies analyzed in this work. Columns z (redshift), type (SB = starburst, AGN = active galactic nucleus, Sy2 = Seyfert 2, QSO = quasi-stellar object) are from NED (https://ned.ipac.caltech.edu/). Columns D_L (luminosity distance) and infrared luminosity (in range $8-1000$ μm) from Armus, Mazzarella, et al. 2009. X-ray luminosity (between 2 and 10 keV) is from Brightman et al. 2011. Star formation rate is calculated from tabulated L_{IR} using Kennicutt and Evans 2012 formula: $\log SFR = \log L_{IR} - 43.41$.

been extracted using a Gaussian fit with a width derived from CO 1−0 (observed by other sub-mm/infrared instruments, see subsequent paragraphs) and through the convolution with the instrument line shape. All the galaxies studied in this thesis are seen by SPIRE as point sources, and the adopted flux error in this case has been of 16%: 10% for the flux extraction and baseline definition, and 6% for the absolute calibration uncertainty.

The CO lines from $J = 1 - 0$ to $J = 3 - 2$ are taken, by Rosenberg et al. 2015 and consequently by this work, from literature about ground based observations.

NGC 34 line $J = 1 - 0$ come from Heckman, Blitz, et al. 1989, observed with the 12-m telescope at NRAO located on Kitt Peak (2096 m), Arizona. It have a beam size equivalent to 48″ The flux error is 40%. CO $J = 2 - 1$, as stated in Rosenberg et al. 2015, has a 3.06×10^{-15} erg s^{-1} cm^{-2} flux, with a beam size of 23″. The reference for this $J = 2 - 1$ line should be Heckman, Blitz, et al. 1989, but it is not. A flux error of 40% is assumed, since it is the maximum flux error available for the sample (for the NGC 34 CO $J = 1 - 0$ line).

CO lines at low J for IRAS F05189−2524, NGC 4418 and NGC 6240 come from Papadopoulos et al. 2012. CO $J = 1 - 0$ has been observed with the IRAM 30-m telescope, located on Pico Veleta (2850 m) in the Spanish Sierra Nevada. CO $J = 2 - 1$ and $J = 3 - 2$ lines instead have been observed with the 15-m JCMT on Mauna Kea (4092 m) in Hawaii. The beam sizes are 22″ for $J = 1 - 0$, 14″ for $J = 2 - 1$ and 11″ for $J = 3 - 2$. The flux errors are between 14 and 17% for IRAS F05189−2524 (hence 17% is assumed), 21% for NGC 4418 lines and 9%, 17% and 20% going from lower to higher J in case of NGC 6240.

2.3 The ALMA CO SLEDs

2.3.1 The Atacama Large Millimeter/submillimeter Array

The Atacama Large Millimeter/submillimeter Array (ALMA) is an international mm/sub-mm interferometer situated in the Atacama Desert of northern Chile, at 5059 m of altitude (Wootten et al. 2009). It comprises the *12-m Array*, made of 50 12-m antennas, with a maximum baseline of 15 km, and the *Atacama Compact Array* (ACA), with 4 12-m and 12 7-m antennas and a minimum baseline of 15 m (Mangum 2016). It has a frequency coverage from 31 to 950 GHz (or from 9.7 mm to 316 μm) divided in 10 Bands. Every Band is divided in spectral windows (a standard observation comprehends 4 spectral windows), and every spectral window is splitted in 3840 channels, every one with a bandwidth of 488.281 kHz. Every antenna is also equipped with a Water Vapour Radiometer (WVR) for correcting the signal phase fluctuations caused by fluctuations of water vapour content of the atmosphere.

Typically ALMA observes for first the flux and bandpass calibrators, and then the phase calibrator and the target alternatively for the rest of the time. The resulting visibility data are stored in a raw Measurement Set (MS), ready for be calibrated and cleaned.

ALMA calibrated and cleaned observations come in two types: continuum images and line images. The former are the product of a Multi-Frequency Synthesis (MFS) algorithm, that combine all the channels without the line emission. The latter is a sequence of images, each one produced by the visibilities of a single channel, that is commonly called a *data-cube*; the name comes from the fact that these images have three dimensions: the two spatial ones (e.g. right ascension and declination in an astrometrized image) plus the frequencies or channels or velocities axis. These three concepts in data-cube are equiparable, because every channel is an observation band, i.e. has a frequency range (so that a channel can be identified with his central frequency), and to every frequency, once the source rest frame is set, can be associated a radial velocity from the Doppler effect ($\Delta v/c = \Delta\nu/\nu$, where $\Delta\nu$ is the channel width). A symbolic data-cube is represented in figure 2.2.

2.3.2 Measuring the ALMA fluxes and sizes

In this section is illustrated how the ALMA line images has been processed and the fluxes have been obtained in this work. Since ALMA observations are shaped as data-cubes, it is necessary to collapse all the observed frequencies on a single image (see figure 2.2): this collapsed image is called moment 0 map, and the intensity on a pixel i is just the integral of the intensities of all pixels in the same x, y position along all the observed channels (i.e. frequencies or wavelengths or energies).

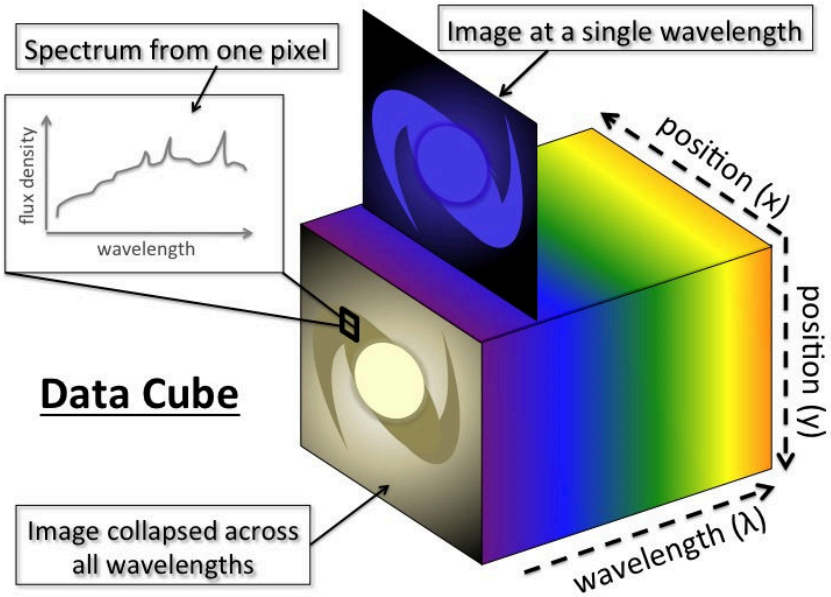

Figure 2.2: Picture of a data-cube: in our case the two position axes (x and y in figure) are right ascension and declination. The single wavelengths are actually single channels with a certain width $\Delta\lambda$. The collapsed image is the moment 0 map (see section 2.3.2 for a proper definition). Taken from Harrison 2014, figure 2.1.

It is common to use velocities instead of frequencies for the different channels: these come directly from the Doppler formula $\Delta v/c = \Delta\nu/\nu$, so for every transition with frequency (emitted at rest) ν, to every given channel frequency width $\Delta\nu$ is possible to associate the correspondent channel velocity width Δv. The moment 0 integral will be done over the velocity axis, and the result is an intensity expressed in units of Jy km s^{-1}, easily convertible, given the emitted frequency ν, in the erg s^{-1} cm^{-2} common flux units.

The software used for the moment 0 map production is the Common Astronomy Software Applications (CASA, McMullin et al. 2007) with the following steps.

1. Manually inspect the data-cube channel per channel in order to discard the ones containing only noise
2. Spatially isolate the central emission in a box; this is done to avoid the noise that could be present in the outer parts of the field of view, that can be seen for instance in figure 2.3
3. Calculate the Root Mean Square (RMS $= \sqrt{\sum_i I_i^2/n}$, where n is the number of pixels and I_i the i-th pixel value, here in units of Jy/beam) of the *noise* channels; this is a measure of the average noise of the single channel images
4. Produce a moment 0 map of the emission on the selected channels (step 1) and within the created box (step 2); from this map extract the RMS, that we call here σ to avoid confusion with the single-channel RMS (approximately $\sigma = N_{chans}\Delta v_{chan}$RMS, in units of Jy km s^{-1}).

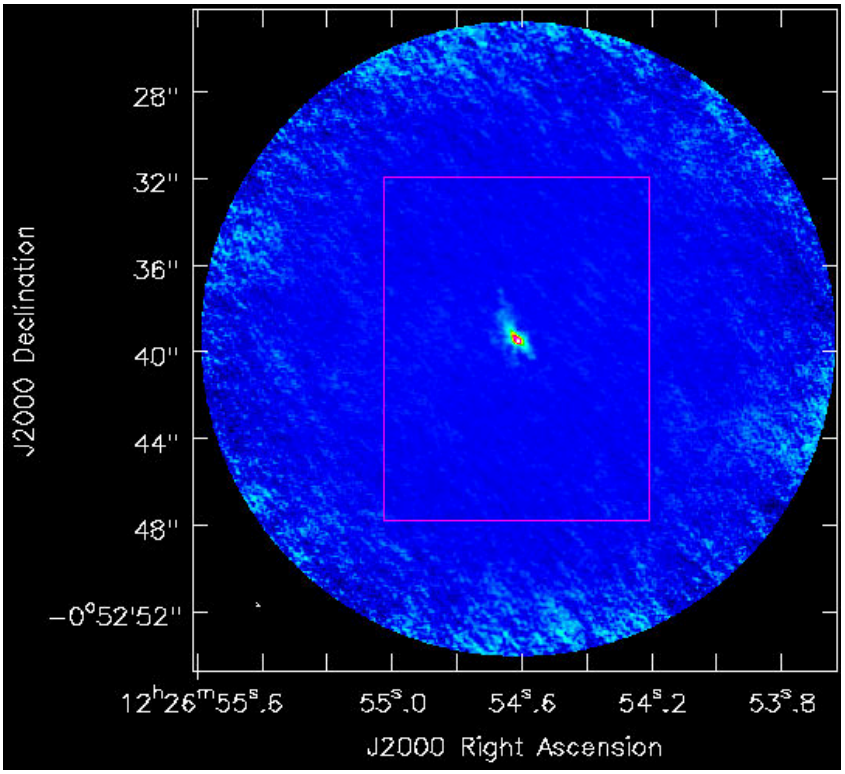

Figure 2.3: An example of box making on an ALMA data-cube. The image is a single channel from the data-cube relative to NGC 4418 CO $J = 3 - 2$ transition. The image is already astrometrized, so the axes are right ascension and declination at the epoch J2000 (i.e. January 1^{st}, 2000 at 12 o'clock). In the outer part of the field is possible to see some noise, avoidable with the rectangular box created. The tiny point on the bottom left is actually an ellipse that represents the size of the synthesized beam.

5. Calculate the flux density (in Jy km s^{-1}) inside a manually selected region from the moment 0 map made with a threshold of 3σ; the manual selection is made to exclude peripheral clouds and focus on the central one

6. In order to quantify the flux error, cover the *noise-masked* (i.e. masked from emission) moment 0 map with as many as possible square regions with the same (within a 10% tolerance) pixel area of the region selected at step 5, extract the flux density from each of them and calculate the standard deviation of these fluxes

7. Produce also a moment 1 map of the aforesaid emission on the selected channels (step 1) and within the created box (step 2) with a threshold chosen on the fly in units of RMS (the one got at step 3); the threshold here is necessary to make a clean moment 1 image

At the end of this procedure two images have been produced, the 0 and 1 moment maps. The contours superimposed to them are always in this work, if not mentioned, the CO isophotes at 3, 4, 5, 10, 20, 50 and 100 σ, where σ is the one computed at step 4.

Note about CASA flux measure units

After the calibration and cleaning processes, every pixel on a channel map of data-cube conveys with it the 2 spatial coordinates in which is located and the calibrated flux, in units of Jy/beam (1 Jy = 10^{-23} erg s^{-1} cm^{-2} Hz^{-1}). The beam (i.e. the synthesized beam) appears here because every pixel is convolved with it, so in order to switch from Jy/beam to Jy is just to divide for the beam area in pixels. However this process is automatic for the flux density, so that CASA gives this quantity both in Jy and Jy/beam.

2.3.3 Results of observations

The ALMA calibrated and cleaned CO data-cubes have been downloaded from the ALMA Science Archive[1] in March 2017; all the public data concerning the 4-galaxies sample $^{12}C^{16}O$ observations available at that time has been taken and processed as explained in section 2.3.2.

In this section the data for each galaxy is shown and compared, where present, with CO line fluxes obtained from different instruments from Rosenberg et al. 2015. We will give here particular importance to the synthesized beam, the largest angular scale and the field of view; all of these three depend on the observed wavelength λ. The first is a measure of the spatial resolution of the observation, and often is worst than the original spatial resolution achieved by the interferometer (which is $\theta \simeq \lambda/B_{max}$, with B_{max} the maximum baseline, i.e. the distance between the two most distanced antennas), due to the calibration and cleaning procedure. The second, LAS for brevity, is the maximum recovable scale that can be seen by the interferometer, and depends on the minimum baseline (LAS $\simeq \lambda/B_{min}$); any feature bigger than the LAS is not recovered by the interferometer and its flux is lost. The last one, FoV for brevity, is a measure of the field that the interferometer can see, and depends on the diameter D of a typical antenna of the interferometer (which in the case of ALMA is always 12m or 7m): FoV $\simeq \lambda/D$.

The errors on the fluxes are the squared root of the sum of the squared of the error due to measurement noise (ε_{noise}) and the one caused by flux calibration (ε_{calib}); the latter depends on which calibrators have been used in a particular observation, and is always a value between 10% and 20%, so for convenience we have decided to keep it fixed to the most conservative value of 20% of the observed flux. Since in these observations $\varepsilon_{calib} \gg \varepsilon_{noise}$, the total error is always assumed $\varepsilon_{tot} = \sqrt{\varepsilon_{noise}^2 + \varepsilon_{calib}^2} \approx \varepsilon_{calib} = 20\%$.

In table 2.1 the sample of galaxies is synthesized. The complete CO SLED used in this work for each galaxy is presented in table 3.1, whilst in table 2.2 the sizes of the observed CO emitting regions are listed.

[1] http://almascience.nrao.edu/aq/

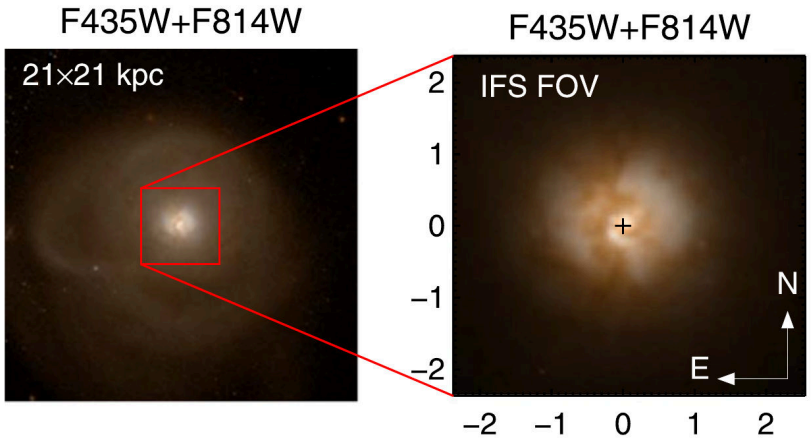

Figure 2.4: Hubble Space Telescope image of IRAS F05189−2524, done with ACS F435W and F814W filters. The left FoV is 25" × 25", the right one 5".6 × 5".4. Taken from Rupke et al. 2015, figure 1.

IRAS F05189-2524

IRAS F05189−2524 ($05^h21^m01^s.42 - 25°21'45''.47$, $z = 0.04256$, $D_L = 187$ Mpc) is a ULIRG ($L_{IR} = 10^{12.16} L_\odot$) classified as Quasi-Stellar Object (Rosenberg et al. 2015) and Seyfert 2 (Veilleux et al. 1995, using the BPT diagram: see section 1.3.2 for details), with a hard-X luminosity $L_{2-10} = 10^{44.17}$ erg/s (Brightman et al. 2011), that unequivocally labels it as an AGN (section 1.3.2). From the optical image [2] is possible to see tidal tails, evidence of past merging activity (however now it seems a fully relaxed system, due to little tails compared to other ULIRGs and a single pointlike nucleus, according to Rigopoulou et al. 1999). It has a ratio between fluxes at 25 and 60 μm > 0.2 ($f_{25}/f_{60} = 0.25$, Chung et al. 2009), which categorizes it as a *warm* ULIRG (Sanders and Mirabel 1996).

The only CO transition found on ALMA Archive is the CO $J = 1 - 0$. The observations date back to September 3, 2015 (cycle 1, project 2012.1.00306.S, PI: Sturm). The galaxy was observed in Band 3, with spatial resolution 0.23″, LAS 26″ and FoV 61″, the last two corresponding to 21.6 kpc and 50.7 kpc in physical scales (given an angular distance of $D_A = 172$ Mpc). At the end of the calibration and cleaning the synthesized beam has become 0.40″ or 335 pc. The line image has a $RMS = 0.30$ mJy/beam, the moment 0 image a $RMS = 71$ mJy km s^{-1} beam^{-1}. The measured flux on moment 0 (figure 2.5) is 18.7 ± 0.3 Jy km/s, or $(6.9 \pm 0.1) \times 10^{-17}$ erg s^{-1} cm^{-2}, with a calibration error $\varepsilon = 1.4 \times 10^{-17}$ erg s^{-1} cm^{-2}. The reported flux for the same transition in Rosenberg et al. 2015 (actually from Papadopoulos et al. 2012) is $(1.8 \pm 0.3) \times 10^{-16}$ erg s^{-1} cm^{-2} (with a 17% error applied − see section 2.2), so apparently ALMA here is losing flux. As Papadopoulos et al. 2012 explain, they took the average between their 2008 measurement (with the Kitt-Peak 12-m telescope of Arizona Radio Observatory) and the 2004 measurement of M. Strong et al. 2004 (done with the 15-m Swedish ESO Submillimetre Telescope), which are similar, but they mention also an older observation

[2] HST image with superimposed CO 1-0 contours

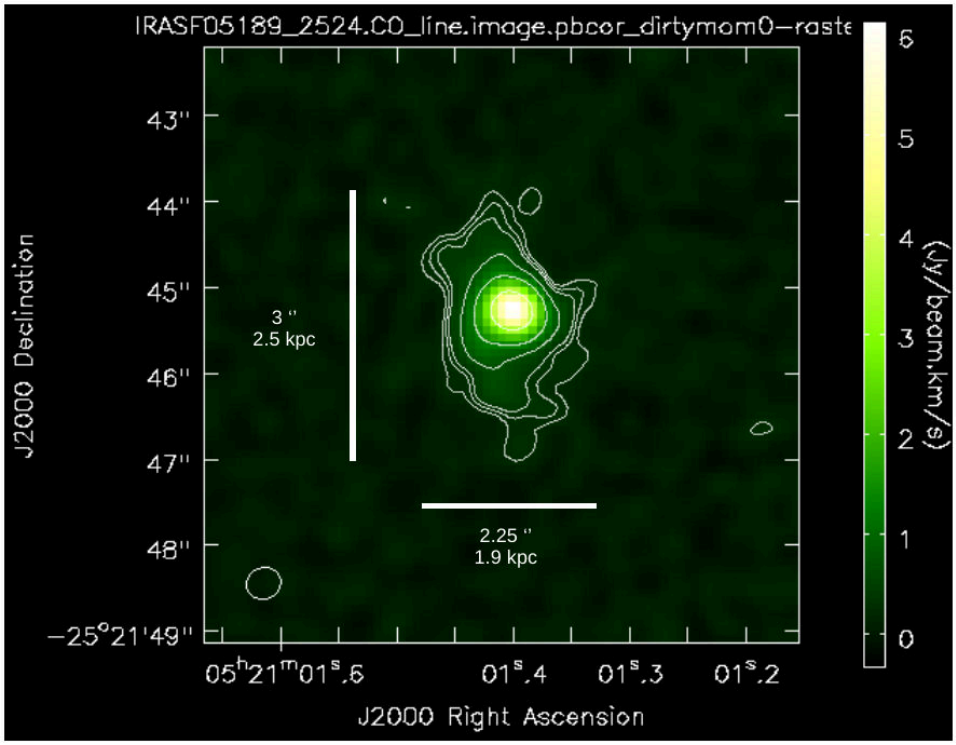

Figure 2.5: Moment 0 image of IRAS F05189−2524 CO $J = 1 - 0$ transition. The RMS is $\sigma = 71$ mJy beam^{-1} km s^{-1}. The contours are at $(3, 4, 5, 10, 20, 50, 100) \times \sigma$. The total flux within 3σ is 18.7 ± 0.3 Jy km s^{-1}. The beam is 0.40 arcsec, the LAS 26 arcsec.

(Sanders, Scoville, et al. 1991) of a more than doubled flux. With the informations in our hand, we have decided to use the final value reported by Papadopoulos et al. 2012 and Rosenberg et al. 2015 and to use ALMA observation only for the size of emitting region, which is approximately 2 kpc × 2.5 kpc (see figure 2.5).

NGC 34

NGC 34 ($00^h11^m06^s.53 - 12°06'24''.90$, $z = 0.01962$, $D_L = 84.1$ Mpc) is a Seyfert 2 galaxy, hosting a strong starburst ($64 M_\odot/yr$) and a weak AGN ($L_{2-10} \approx \times 10^{42}$ erg/s with *XMM-Newton*, Guainazzi et al. 2005 and Brightman et al. 2011), and it is an average LIRG, due to its 8-1300 μm luminosity $L_{IR} = 10^{11.54}$ (Fernández et al. 2010). The galaxy is the remnant of a (probably unequal-mass) *wet* merger, due to the presence of tidal tails and its wealth of cold gas ($M_{HI+H_2} = 1.2 \times 10^{10} M_\odot$, Schweizer et al. 2007). Since the angular distance is $D_A = 80.9$ Mpc, the conversion factor between angular and physical size is $1'' = 392$ pc.

Data-cubes for CO transitions $J = 3 - 2$ and $J = 6 - 5$ are available at ALMA Archive. The former (a Band 7 observation) comes from the project 2013.1.00814.S (PI Haan, Cycle 1, observed in date July 20, 2015), with a synthesized beam 0.16″, LAS 7.5″ and FoV 18.2″. The RMS of the line image is 1.7 mJy/beam, while the moment 0 RMS

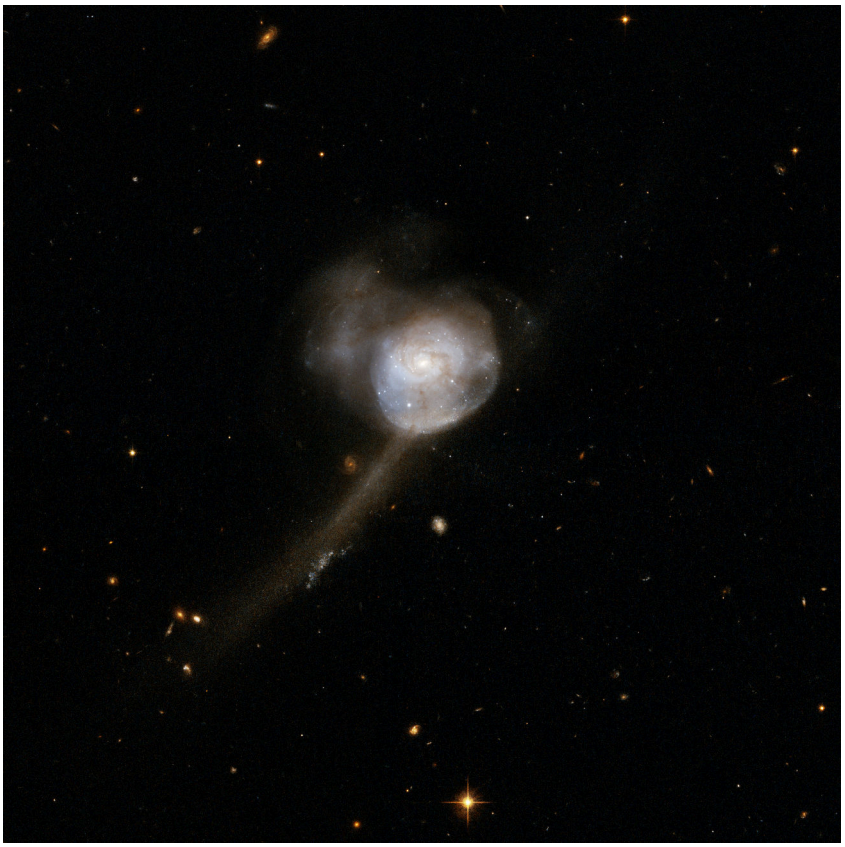

Figure 2.6: This NGC 34 image is part of a large collection of 59 images of merging galaxies taken by the Hubble Space Telescope and released on the occasion of its 18th anniversary on 24th April 2008. The filters used are HST F435W and F814W. Credits: NASA, ESA, the Hubble Heritage (STScI/AURA)-ESA/Hubble Collaboration, and A. Evans (University of Virginia, Charlottesville/NRAO/Stony Brook University).

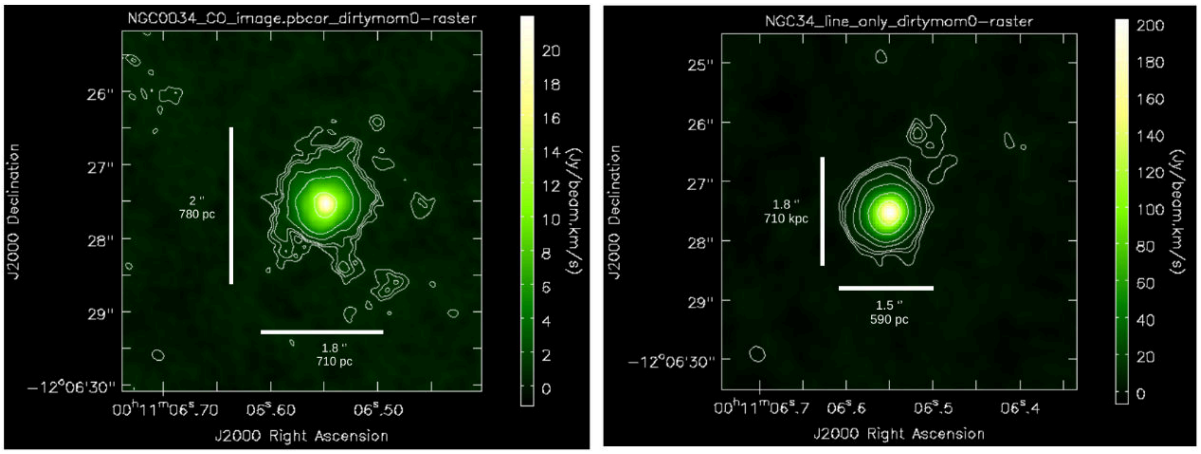

Figure 2.7: Moment 0 images of NGC 34 CO $J = 3 - 2$ (left image) and $J = 6 - 5$ (right image) transitions. For CO $J = 3 - 2$: RMS is $\sigma = 0.23$ Jy beam^{-1} km s^{-1}, total flux within 3σ is 300 ± 10 Jy km s^{-1}, beam is 0.16 arcsec, the LAS 7.5 arcsec. For CO $J = 6 - 5$: RMS is $\sigma = 1.2$ Jy beam^{-1} km s^{-1}, total flux within 3σ is 940 ± 20 Jy km s^{-1}, beam is 0.27 arcsec, the LAS 4.1 arcsec. The contours are at $(3, 4, 5, 10, 20, 50, 100) \times \sigma$ for both maps.

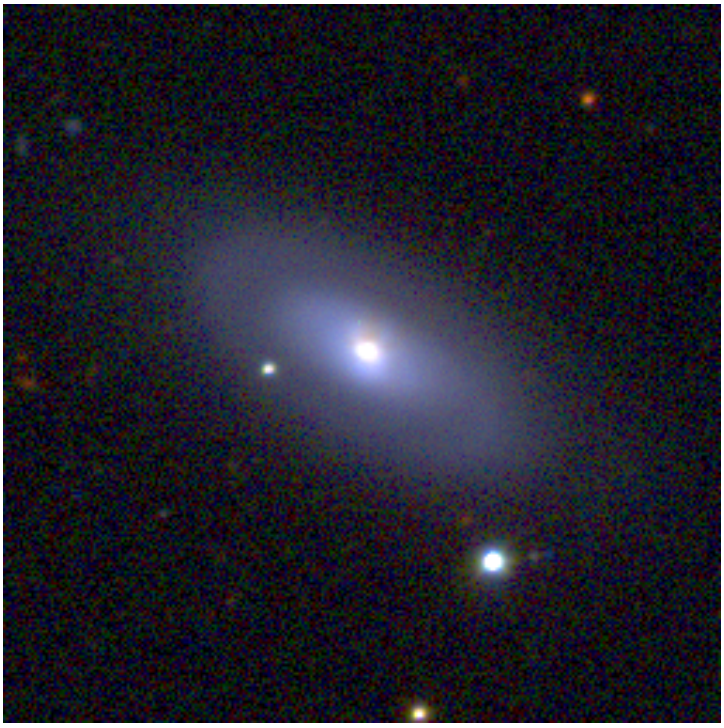

Figure 2.8: NGC 4418 optical image made with SDSS filters. Taken from Baillard et al. 2011.

is 0.23 Jy km s^{-1} beam^{-1}. The measured flux on moment 0 image (left picture of figure 2.7) is 300 ± 10 Jy km/s or $(3.4 \pm 0.1) \times 10^{-15}$ erg s^{-1} cm^{-2}, with a calibration error $\varepsilon = 0.68 \times 10^{-15}$ erg s^{-1} cm^{-2}. The emitting region has a spheroidal shape with 3σ sizes of 710 and 780 pc.

The CO $J = 6 - 5$ observation (Band 9, project 2011.0.00182.S, PI Xu, Cycle 0, observed in May 20, 2012) has a synthesized beam 0.27″, LAS 7.5″ and FoV 18.2″. Data-cube RMS is 6.1 mJy/beam, moment 0 RMS 1.2 Jy km s^{-1} beam^{-1}. Moment 0 flux is $(2.12 \pm 0.04) \times 10^{-14}$ erg s^{-1} cm^{-2}, the same as the *Herschel* one ($(2.1 \pm 0.3) \times 10^{-14}$ erg s^{-1} cm^{-2}, Rosenberg et al. 2015). The flux comes from an elliptical region of axes 590 and 710 pc (see right picture of figure 2.7).

NGC 4418

NGC 4418 ($12^h26^m54^s.60 - 00°52'36''.54$, $z = 0.007268$, $D_L = 36.5$ Mpc) is a LIRG ($L_{IR} = 10^{11.19}$ erg/s, Rosenberg et al. 2015), in which it is not clear whether its multi-wavelength spectrum and features are due only to the presence of a massive and compact (< 100 pc) starburst (of this opinion is Varenius et al. 2014) or also to a buried AGN (Spoon et al. 2001, Imanishi et al. 2004), with column density $N_H > 10^{24}$ cm^{-2} (Maiolino et al. 2003) or even $N_H \gtrsim 10^{25}$ cm^{-2} (González-Alfonso et al. 2012, that find also evidence for a gas inflow towards the nuclear region of $\lesssim 12$ M$_\odot$/yr). Everybody seems just sure that we cannot state the presence of an AGN nor deny it.

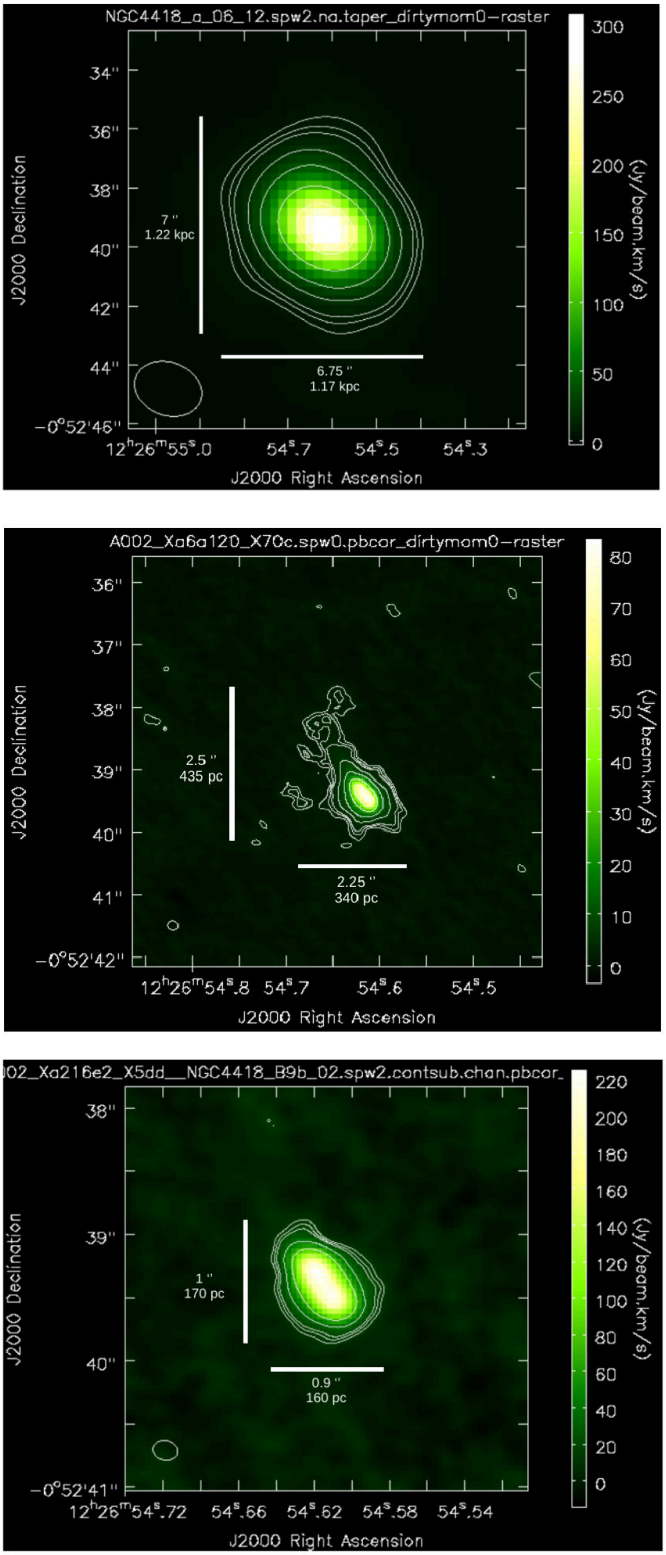

Figure 2.9: Moment 0 images of NGC 4418 CO $J = 2 - 1$ (top), $J = 3 - 2$ (center) and $J = 6 - 5$ (bottom) transitions. CO $J = 2 - 1$: RMS is $\sigma = 1.9$ Jy beam^{-1} km s^{-1}, flux within 3σ is 431 ± 3 Jy km s^{-1}, beam is 2.3 arcsec, the LAS 25 arcsec. CO $J = 3 - 2$: RMS is $\sigma = 0.57$ Jy beam^{-1} km s^{-1}, flux within 3σ is 600 ± 10 Jy km s^{-1}, beam is 0.17 arcsec, the LAS 8.2 arcsec. CO $J = 6 - 5$: RMS is $\sigma = 3.7$ Jy beam^{-1} km s^{-1}, flux within 3σ is 1210 ± 30 Jy km s^{-1}, beam is 0.20 arcsec, the LAS 3.3 arcsec. The contours are at $(3, 4, 5, 10, 20, 50, 100) \times \sigma$ for each moment 0 map.

Data-cubes for CO transitions $J = 2 - 1$ (with 4 different observations) $J = 3 - 2$ and $J = 6 - 5$ are available at ALMA Archive. Two of the four $J = 2 - 1$ images have been discarded: the former due to its low resolution ($28''$, where the others have better ones with a factor of 10), the latter because of the very small flux observed, a factor 100 compared to the other three. Since the angular distance of NGC 4418 is $D_A = 36.0$ Mpc, 1 arcsec is equal to 174 pc. All the NGC 4418 data here shown come from ALMA project 2012.1.00377.S, Cycle 1, PI Sakamoto.

The two Band 6 CO $J = 2 - 1$ data-cubes left, here ordered by resolution, have synthesized beams $2.3''$ and $8.3''$. Their emission areas are respectively 1.1 and 4.8 kpc^2. The first of these three maps is shown in figure 2.9 (the *top* one). Since their LASs are similar ($25''$ and $28''$) we have chosen to use, as a measure of the flux, the average between the two CO $J = 2 - 1$. That said, the average flux is $(3.14 \pm 0.04) \times 10^{-15}$ erg s^{-1} cm^{-2}, with data-cube RMS 5.0 mJy/beam and moment 0 RMS 3.8 Jy km s^{-1} beam^{-1} (flux error and RMSs have been chosen as the bigger values found between the two observations).

CO $J = 3-2$ has been observed in Band 7 on July 24, 2015. Beam, LAS and FoV are respectively 0.17, 8.2 and 18 arcsec. Data-cube and moment 0 RMS are 1.9 mJy/beam and 0.57 Jy km s^{-1} beam^{-1}. The measured flux on moment 0 image (center of figure 2.9) is $(6.9 \pm 0.1) \times 10^{-15}$ erg s^{-1} cm^{-2}, but since is the half of that reported by Papadopoulos et al. 2012 ($(1.14 \pm 0.23) \times 10^{-15}$ erg s^{-1} cm^{-2}), we decided to discard it but to save the size of the emitting region (340×435 pc).

CO $J = 6 - 5$ has the same problem, so it is preferable to use the Rosenberg et al. 2015 one, i.e. $(3.6 \pm 0.6) \times 10^{-14}$ erg s^{-1} cm^{-2}. The ALMA 3σ emission borders a region large 160×170 pc (bottom image of figure 2.9).

NGC 6240

NGC 6240 ($16^h52^m59^s.01 + 02°24'03''.27$, $z = 0.02448$, $D_L = 116$ Mpc) is a local LIRG/ULIRG ($L_{IR} = 10^{11.93}$, Rosenberg et al. 2015) hosting a binary AGN (Komossa et al. 2003, with a $0.1 - 10$ keV luminosity of 0.7×10^{42} erg/s and 1.9×10^{42} erg/s), pointing it as a young merger, maybe the progenitor of an elliptical galaxy. The optical spectrum of NGC 6240 is classified as a LINER (Low Ionization Nuclear Emission-line Region, see section 1.3.2), Armus, Bernard-Salas, et al. 2006 and references therein), and the starburst (SFR = 140 $M_\odot$/yr) is powering a superwind with velocities up to 10^3 km/s (Heckman, Armus, et al. 1990). From fitting the hard X-ray spectrum (as seen by BeppoSAX) the column density is $\sim 2 \times 10^{24}$ cm^{-2} (Vignati et al. 1999).

The ALMA CO observations of NGC 6240 consist in 3 data-cubes: one for the $J = 2 - 1$ and two for the $J = 3 - 2$ transition. In all of these cases the fluxes from moment 0 images are smaller than the ones from Papadopoulos et al. 2012, so we kept only the dimensions of emitting regions from ALMA data. These are 5.6 kpc $\times$ 5.9 kpc for the CO $2-1$ (synthesized beam $1.54'' = 825$ pc, left of figure 2.11) and 2.1 kpc $\times$ 1.6

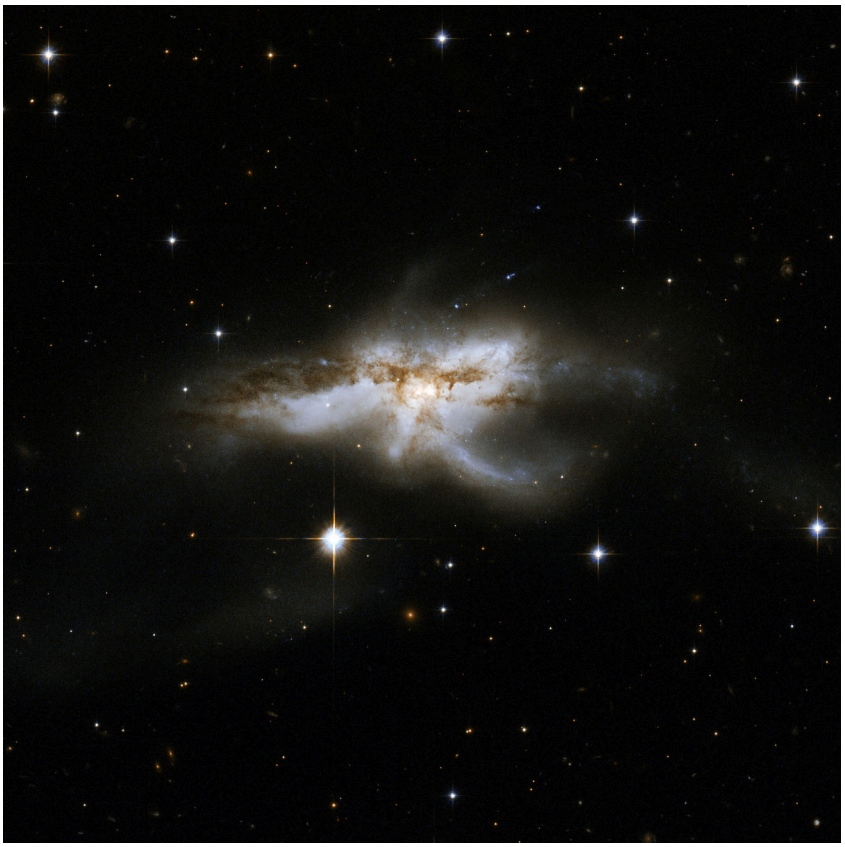

Figure 2.10: NGC 6240 seen by Hubble Space Telescope with filters F435W and F814W. Also this image (like 2.6 has been released on the occasion of HST 18th anniversary on 24th April 2008. Credits: NASA, ESA, the Hubble Heritage (STScI/AURA)-ESA/Hubble Collaboration, and A. Evans (University of Virginia, Charlottesville/NRAO/Stony Brook University).

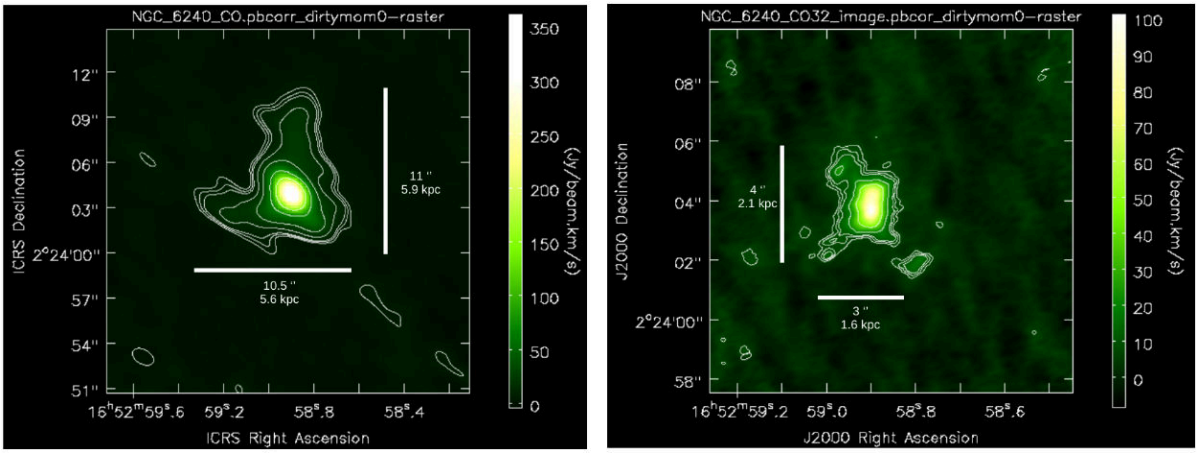

Figure 2.11: Moment 0 images of NGC 6240 CO $J = 2 - 1$ (left) and $J = 3 - 2$ (right) transitions. CO $J = 2-1$: RMS is $\sigma = 1.5$ Jy beam^{-1} km s^{-1}, flux within 3σ is 1260 ± 20 Jy km s^{-1}, beam is 1.54 arcsec, the LAS 13 arcsec. CO $J = 3 - 2$: RMS is $\sigma = 2.1$ Jy beam^{-1} km s^{-1}, flux within 3σ is 2100 ± 90 Jy km s^{-1}, beam is 0.37 arcsec, the LAS 14 arcsec. The contours are at $(3, 4, 5, 10, 20, 50, 100) \times \sigma$ for both images.

kpc for the CO $3-2$ with the best resolution (that is a synthesized beam of $0.37'' = 200$ pc, right part of figure 2.11).

Galaxy	CO Transition	Area [pc^2]	$\theta_{\rm res}$ [pc]	LAS [kpc]	ALMA Project
IRAS F05189−2524	$J = 1-0$	2.5×10^6	335	21.6	2012.1.00306.S
NGC 34	$J = 3-2$	4.9×10^5	64	2.92	2013.1.00814.S
NGC 34	$J = 6-5$	3.1×10^5	105	1.62	2011.0.00182.S
NGC 4418	$J = 2-1$	1.1×10^6	410	4.43	2012.1.00377.S
NGC 4418	$J = 2-1$	4.8×10^6	1440	4.94	2012.1.00377.S
NGC 4418	$J = 3-2$	5.5×10^4	30	1.42	2012.1.00377.S
NGC 4418	$J = 6-5$	1.8×10^4	35	0.57	2012.1.00377.S
NGC 6240	$J = 2-1$	1.8×10^7	825	722	2015.1.00370.S
NGC 6240	$J = 3-2$	1.9×10^6	200	7.40	2013.1.00813.S
NGC 6240	$J = 3-2$	3.0×10^6	500	4.42	2013.1.00813.S

Table 2.2: Observed CO emission regions with ALMA. The areas are calculated within the 3σ contours using the angular distance $D_A = D_L/(1+z)^2$, with D_L and z listed in table 2.1 for each galaxy.

Chapter 3

CO SLEDs interpretation

3.1 Simulations of molecular clouds

In this thesis work the CO spectral line energy distribution of each galaxy of the sample has been physically interpreted using the spectral synthesis code CLOUDY (Ferland et al. 2013 and references therein). The observed CO SLEDs are listed in table 3.1: in case we had both ALMA and Herschel fluxes for a given transition (see sections 2.2 and 2.3.3), the choice has fallen on the larger of the two (assuming the other one is losing flux in that given observation).

Transition	IRAS F05189−2524	NGC 34	NGC 4418	NGC 6240
$J = 1 - 0$	0.018	0.074	0.05	0.121
$J = 2 - 1$	0.096	0.306	0.314^a	1.117
$J = 3 - 2$	0.283	0.34^a	1.137	3.6
$J = 4 - 3$	–	–	2.47	9.57
$J = 5 - 4$	1.96	1.97	2.78	11.13
$J = 6 - 5$	2.38	2.13	3.56	13.38
$J = 7 - 6$	2.61	2.43	4.14	16.53
$J = 8 - 7$	2.80	2.90	5.20	18.08
$J = 9 - 8$	1.74	2.80	5.25	16.51
$J = 10 - 9$	2.90	1.55	5.88	13.92
$J = 11 - 10$	2.53	2.39	6.43	13.20
$J = 12 - 11$	2.07	1.63	5.85	12.45
$J = 13 - 12$	2.12	1.23	6.19	9.80

Table 3.1: CO SLEDs of the 4 galaxies studied in this work. The fluxes are in units of 10^{-14} *erg* s^{-1} cm^{-2}*, and are taken from Rosenberg et al. 2015 and references therein (for details see section 2.2), except for the ones taken from ALMA originally for this thesis (see section 2.3.3) and marked here with an a. The − are missing fluxes in literature. The errors are 16% for the transitions from CO* $J = 4 - 3$ *(if present) going up (Rosenberg et al. 2015), 20% for the ALMA (a) observations (section 2.3.3), and variable for the other lines (see section 2.2 for details).*

3.1.1 The CLOUDY code

CLOUDY is an open source code[1] designed for microphysics simulations of astrophysical gas in diverse situations, such as the stellar corona, the molecular clouds or the accretion disk of an AGN.

The CLOUDY code takes as input the initial conditions of the gas, i.e. its density, geometry, chemical composition, equation of state and a lot of other possible physical specifications, combines these with the incident radiative field that invest the gas (due to the cosmic background, a star population or an AGN) and predicts the resulting spectrum. During a simulation the code computes the ionization, thermal, and chemical state of a gas cloud exposed to radiation. The usual assumption is that atomic processes have had time to become time steady. The numerical density n_i of a species or level i is given by a balance equation of the form:

$$\frac{\partial n_i}{\partial t} = \sum_{j \neq i} n_j R_{ij} + \text{ source } - n_i \left(\sum_{ij} R_{ij} + \text{ sink } \right) \tag{3.1.1}$$

where R_{ij} is the rate with which a species j goes to i, while *source* and *sink* represent the rates for gaining and losing atoms for the i species.

The gas is analyzed zone after zone, where every zone is a thin concentric shell placed at increasing depth inside the cloud, and within each zone the equation 3.1.1 is solved, together with conservations of charge, mass and energy. The thickness of the zones is adjusted with adaptive logic in order to be small enough for the physical conditions across them to be nearly constant.

3.1.2 Simulations setting

The molecules are likely to be excited by OB stars (section 1.2.3) from young star populations (that we know are massively present because the galaxies from this sample are all showing a high level of star formation, as listed in table 2.1), but part of the lines may even have been excited from the central AGN (section 1.2.4), given that significant X-ray luminosity has been observed for all of them, NGC 4418 excluded. Therefore, two models have been produced: a double PDR model, in which a diffuse PDR is combined with a denser one, and a PDR plus XDR model, where is possible to account for the central X-rays source.

A combination of PDRs and XDRs that reproduces the CO SLED can be found in other works in literature, like Meijerink et al. 2007 (in which the authors created their own code and models), Xue et al. 2009 (that used CLOUDY) and Pereira-Santaella et al. 2014 (that used the microphysics code RADEX from van der Tak et al. 2007). The

[1] available for free download at http://www.nublado.org

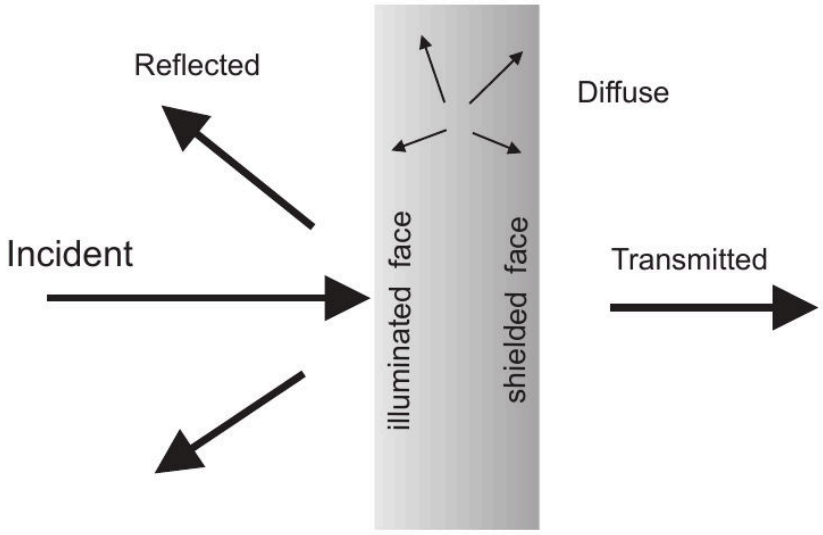

Figure 3.1: CLOUDY *simulates the gas cloud as a slab like the one shown in figure: it distinguishes a illuminated face (illuminated from the incident radiation field) and a shielded face, through which the transmitted radiation emerges. Taken from HAZY, a brief introduction to* CLOUDY *C13.05, figure 2.1.*

method followed in this thesis follows the method described in Vallini et al. 2017, Pozzi et al. 2017 and Mingozzi et al. (2017, in preparation).

The simulations have been set with the least possible number of free parameters, in order to have a more robust statistical result and eventually a easier physical picture to understand. Other important features are the covering of all the expected physical parameters ranges through simulations grids and the necessity to use a reasonable amount of computational time: a single CLOUDY simulation can last from 6×10^4 up to 10^5 seconds.

The input of a simulation is a plain text file with all the details of both the gas cloud properties and the radiation field to which it is exposed. The code produces output files in form of tables, in which density, temperature, pressure, ionization, molecular fractions and line fluxes are shown as functions of depth inside the cloud, measured starting from the illuminated face of the cloud (see figure 3.1). Also the continuum spectrum file is produced in function of emitted frequency, including the emission lines.

Two grids of parameters (a PDR grid and a XDR grid) have been produced; in the next paragraphs the peculiar choices for the corresponding parameters are detailed, while here we will discuss the common parameters for both the grids. The CLOUDY input script is available in appendix A.

The gas follows a plane-parallel geometry (see figure 3.1) and has an unknown covering of the radiation source. Our model (figure 3.2) assumes PDRs and XDRs to be spherical shells; within a PDR resides a little stellar cluster, whose radiation strikes the inner

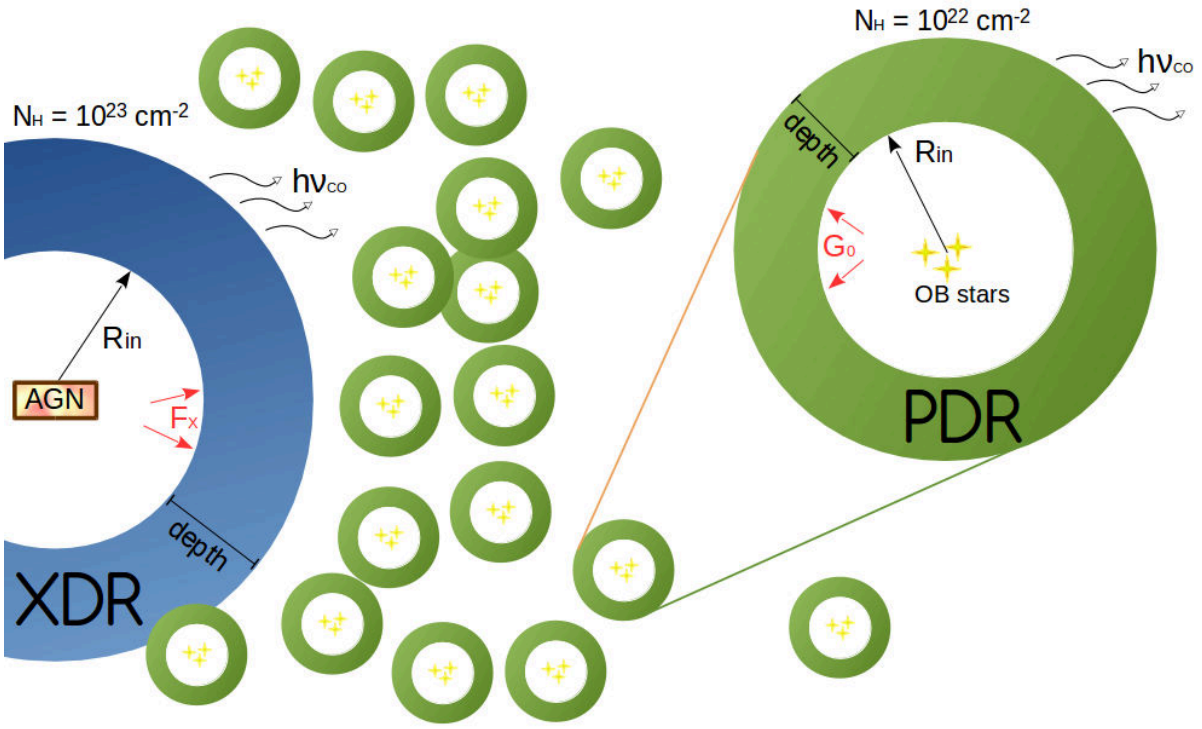

Figure 3.2: Sketch of the assumed model for this thesis. PDRs and XDRs are spherical shells surrounding respectively stellar clusters and the AGN.

surface of the PDR with a FUV flux G_0 (see section 1.2.3); the same thing applies for the XDR model, where the X-rays radiation comes from the AGN (see section 1.2.4).

As equation of state a constant pressure law has been used, in order to ensure an equilibrium with the surrounding ISM (Carral et al. 1994, Abel, Ferland, et al. 2005). In these simulations, CLOUDY defines the pressure as:

$$P_{tot} = P_{gas} + P_{mag} + P_{lines} + \Delta P_{rad} \tag{3.1.2}$$

where $P_{gas} = nk_BT_e$ (n is the numerical density, T_e the electron temperature), $P_{mag} = B^2/8\pi$ is the magnetic pressure, P_{lines} is the radiation pressure due to trapped emission lines[2] and $\Delta P_{rad} = \int a_{rad}\rho dr$ compensates for the acceleration a_{rad} due to the absorption of the incident radiation (Ascasibar et al. 2010). The magnetic field follows a power law of the density $B = B_0(\rho/\rho_0)^{(\gamma/2)}$; the fiducial values adopted in this work have been $\log B_0[G] = -3.5$ and $\gamma = 4/3$.

Cosmic rays, that consist primarily of high-energy protons and electrons, are very important in CLOUDY simulations if molecular gas is present, because they trigger the molecules formation through gas ionization (see section 1.2.1). CLOUDY takes as input the cosmic ray rate, intended as the H^0 ionization rate in s^{-1} units. A logarithmic rate

[2]In case of optically thick medium (see section 1.2.2 for details) to a certain line, that line is said to be *trapped*.

of -16.3 has been adopted (like Williams et al. 1998, Abel, van Hoof, et al. 2008).

The chemical abundances adopted are the ones stored in CLOUDY as `abundances ISM`. They have, for instance, He $= 0.098$, C $= 2.51 \times 10^{-4}$, O $= 3.19 \times 10^{-4}$, Fe $= 6.31 \times 10^{-7}$ as gas-phase abundances relative to the total hydrogen density. These are an average between the works of Cowie et al. 1986 and Savage et al. 1996 on ISM abundances in the Milky Way. Oxygen abundance is from Meyer et al. 1998. The dust grains (another key ingredient for molecular gas simulations, see section 1.2.1) have been set aside: they include both a graphitic and silicate component and reproduce the average Galactic (i.e. of the Milky Way) extinction per reddening of $R_V \equiv A_V/E(B-V) = 3.1$ (see section 1.2.1 and figure 1.5); the dust grains are made of graphite and silicates and their sizes a follow a power-law distribution $n(a) \propto a^{-3.5}$ set by Mathis et al. 1977. Furthermore, PAHs, i.e. Polycyclic Aromatic Hydrocarbons (complex molecules ubiquitously observed and linked to star formation, Calzetti 2011) have been added to the simulations; also their sizes distribution follows a power-law $n(a) \propto a^{-3.5}$, with a number of carbon atoms in every PAH between 30 and 500 (Abel, van Hoof, et al. 2008).

Along with the peculiar radiation source (discussed in next sections 3.1.3 and 3.1.4) the gas is exposed to the background cosmic radiation: this is, in CLOUDY, a combination of CMB[3] and a $\alpha = -1$ power law in the UV part.

A key parameter is the stopping criterion, that tells the algorithm when to stop the simulation: a common way to stop PDR and XDR simulations is to set a maximum column density, after which line fluxes are saturated because almost all the photons from the radiation source have been already processed (see figures 1.9 and 1.12). The adopted column densities are $N_H = 10^{22}$ cm^{-2} for the PDRs and $N_H = 10^{23}$ cm^{-2} for the XDRs, but we decided to run the simulations with a factor 10 greater, so the stopping criteria have been $N_H = 10^{23}$ cm^{-2} for the PDR grid and $N_H = 10^{24}$ cm^{-2} for the XDR one.

Grid	$\log(n_H)$	Incident flux	N_H stop	Simulations
PDR	from 1.5 to 5.5 step 0.5	from $\log(G_0) = 0$ to $\log(G_0) = 5$ step 1	10^{23} cm^{-2}	46
XDR	from 1.5 to 5.5 step 0.5	from $\log(f_x) = -2.85$ to $\log(f_x) = +4.15$ step 0.5	10^{24} cm^{-2}	88

Table 3.2: CLOUDY *simulations. Density is in cm^{-3}, FUV flux G_0 in 1.6×10^{-3} erg s^{-1} cm^{-2}, X-ray ($1-100$ keV) flux f_x in erg s^{-1} cm^{-2}. The N_H reported here is the stopping criterion (see text for details). The number of simulations reported in the last column are only the ones completed by* CLOUDY *code without convergence failures.*

[3]The Cosmic Microwave Background radiation is the emission of photons coming from the epoch recombination, i.e. the cosmic time in which photons and baryons have become decoupled; since the Universe at that time was in thermal equilibrium, the emission is a blackbody radiation. at $z = 0$ (about where the galaxies of our sample are) the temperature of this blackbody is $T = 2.725$ K)

3.1.3 PDR grid

The two main parameters of the PDR models are the total gas density (n) and the intensity of FUV radiation (G_0). The density enters in CLOUDY as the total hydrogen density, defined as the sum of neutral, ionized and molecular components:

$$n(H) = n(H^0) + n(H^+) + 2n(H_2) + \sum_{other} n(H_{other}) \tag{3.1.3}$$

For this work densities from $10^{1.5}$ up to $10^{5.5}$ cm^{-3} have been used, with a logarithmic step of 0.5. In this way both the massive diffuse molecular clouds and the denser clumps and cores are included.

The FUV (6 eV $< h\nu <$ 13.6 eV) radiation field is commonly written in PDR studies in Habing units or G_0, where $G_0 = 1$ corresponds to a FUV flux of 1.6×10^{-3} erg s^{-1} cm^{-2} (Habing 1968). In the Milky Way the average FUV field is around $1\,G_0$, but a higher value is expected in starburst: this is because the FUV luminosity is proportional to the star formation rate (Kennicutt and Evans 2012 and references therein), so, for instance, a SFR $\sim 100 M_\odot$/yr would result in an average FUV flux of $\sim 10^2 G_0$ (the SFR of the Milky Way is ≈ 2, Chomiuk et al. 2011); however, between the OB associations an even greater G_0 is expected. The adopted range goes from 10^0 up to $10^5 G_0$, with a logarithmic step of 1.

The SED shape of the starburst population is taken from a Starburst99 simulation. Starburst99 (Leitherer, Schaerer, et al. 1999, Leitherer, Ekström, et al. 2014) is a stellar population synthesis code for galaxies with active star formation. It takes as input the SFR (Star Formation Rate) of the galaxy, the IMF (Initial Mass Function), the metallicity and other minor important parameters. For the CLOUDY simulations a Starburst99 model with SFR = 80 M$_\odot$/yr, Salpeter IMF (i.e. a single slope IMF with power law index 2.35) with mass boundaries 0.1 and 100 M$_\odot$ and 2012 Geneva evolutionary tracks (Leitherer, Ekström, et al. 2014 and Eldridge 2012) with metallicity $Z = 0.014$ have been assumed. The chosen SFR is representative of the galaxy sample (as listed in table 2.1), however it is only a normalization constant for the Starburst99 SED: the SED is re-normalized by CLOUDY in order to match the specified FUV flux, so changing the SFR does not change any result.

Considering the steps in density and in radiation field and discarding the aborted (for convergence errors) 5 simulations, a total of 46 PDR models have been simulated. The model parameters are reported in table 3.2.

3.1.4 XDR grid

In the XDR grid the radiation source is an AGN, of which both the SED shape and the incident flux (between 1 and 100 keV) on the clouds have to be set up. For this

grid the density (defined in equation 3.1.3) goes from $n_H = 10^2$ to 10^5 cm^{-3}, with a logarithmic step of 0.5. The AGN shape is a multi-component continuum (see section 1.3.2 and figure 1.15), with the flux formulated as in equation 3.1.4:

$$f_\nu \propto \nu^{-0.5} \exp\left(-\frac{h\nu}{kT_{BB}}\right) \exp\left(-\frac{kT_{IR}}{h\nu}\right) + a\nu^{-1} \tag{3.1.4}$$

The first term is the one relative to the *blue bump*, parametrized by a temperature T_{BB}, a low-energy slope $\nu^{-0.5}$ and an infrared exponential cutoff at $kT_{IR} = 0.01$ Ryd (where a Rydberg correspond to an energy of 13.6 eV or 2.18×10^{-11} erg). The second term is a power law, with default index -1, that represent the X-ray component; below $1,36$ eV this term is set to 0, while above 100 keV the code assumes the continuum to fall off as ν^{-2}. The a term is adjusted to produce a X-ray to optical/UV ratio α_{ox}. In our simulations $T_{BB} = 10^6$ K (Abel and Satyapal 2008) and $\alpha_{ox} = -1.4$ (Zamorani et al. 1981).

Through this work's sample of galaxies the X-ray luminosity varies from 10^{42} erg s^{-1} (NGC 34) up to $10^{44.2}$ erg s^{-1} (IRAS F05189−2524); these luminosities are integrated between 2 and 10 keV, and are taken from Brightman et al. 2011.

It is possible to extend the luminosity integration to the $1 - 100$ keV range with the aid of the WebPIMMS service[4], based on PIMMS (Portable, Interactive Multi-Mission Simulator, Mukai 1993). As input PIMMS needs: the Galactic (i.e. of the Milky Way) column density N_H^{gal}, the intrinsic (i.e. of the source) column density N_H^{int}, the unabsorbed flux F_{2-10} and the slope Γ of the AGN power-law. As output it gives both the absorbed and unabsorbed fluxes in the $1 - 100$ keV range.

In Brightman et al. 2011 the $2 - 10$ keV luminosity L_{2-10} is reported. To overcome this issue we have defined a fictitious flux as $F_{2-10} = L_{2-10}/(4\pi r^2)$ with $r = 1$ pc. The PIMMS code hence predicts absorbed and unabsorbed $1 - 100$ keV flux F_{2-10} at distance $r = 1$ pc, so finally the $1 - 100$ keV luminosity is $L_{1-100} = 4\pi(1\text{pc})^2 F_{1-100}$. The values found for L_{1-100} are listed in table 3.3, except for NGC 4418 for which we do not have a X-ray flux or luminosity.

Galaxy	L_{2-10} [erg s^{-1}]	N_H^{gal} [cm^{-2}]	N_H^{int} [cm^{-2}]	Γ	L_{1-100} [erg s^{-1}]
IRAS F05189−2524	1.48×10^{44}	1.7×10^{20}	6.58×10^{22}	2.08	4.00×10^{44}
NGC 34	9.55×10^{41}	2.1×10^{20}	4.7×10^{23}	1.9	2.98×10^{42}
NGC 6240	3.09×10^{43}	5×10^{20}	1.12×10^{24}	1.9	9.64×10^{43}

Table 3.3: X-ray data of the sample. All the columns but the last are from Brightman et al. 2011, with L_{2-10} the intrinsic luminosity of the source in the range $2 - 10$ keV. The last column, L_{1-100}, is the intrinsic luminosity in $1 - 100$ keV range, obtained with WebPIMMS.

The intrinsic $1 - 100$ keV luminosities have been converted to incident $1 - 100$ keV

[4] https://heasarc.gsfc.nasa.gov/cgi-bin/Tools/w3pimms/w3pimms.pl

fluxes on the cloud surface by assuming an area for the emitting gas. In particular, the range of the CO area, for each source, goes from the smallest possible distance recovable with ALMA (i.e. the spatial resolution of the observation) to the largest measured emission region. The smallest regions go from 30 pc for NGC 4418 to 335 pc for IRAS F05189−2524, whilst the largest regions go from NGC 34's 780 pc up to NGC 6240's 5.9 kpc.

With all that said, the striking flux per cloud unit area could be approximately between 10^{-4} and 10^{3} erg s^{-1} cm^{-2}. In the simulations the adopted fluxes extend, in logarithmic scale and with units of erg s^{-1} cm^{-2}, from -2.85 to $+4.15$, with 0.5 steps.

Considering the steps in density and in radiation field a total of 88 XDR models have been simulated (after having discarded 12 failures). The model parameters are reported in table 3.2.

3.2 Best-fit of CO SLEDs

As anticipated in section 3.1.2 the observed CO SLEDs have been compared with two kinds of model: a PDR + PDR model and a PDR + XDR model. Given the number of PDRs and XDRs simulations, this translates into $46 \times 46 = 2116$ of the first type and $46 \times 88 = 4048$ of the second type of models.

Every PDR is labelled by its total density n_H and the FUV flux G_0 (see section 3.1.3 for details), and every XDR by its total density n_H and by the X-ray flux F_X (in the $1 - 100$ keV range, see section 3.1.4) to which it is exposed.

The comparison between the observed CO SLED of a galaxy with a computed model has been made with the χ^2 test: since every model predicts a CO SLED, the χ^2 of a model is the sum of the squared differences between the observed (F_j^{obs}) and the modeled (F_j^{mod}) line flux, divided by the observed flux error (ϵ_j^{obs}) squared, over all the lines j (so from CO $J = 1 - 0$ to $J = 13 - 12$):

$$\chi^2 = \sum_{j=1}^{13} \left(\frac{F_j^{obs} - F_j^{mod}}{\epsilon_j^{obs}} \right)^2 \tag{3.2.1}$$

The modeled flux F_j^{mod} of every line j is a weighted sum between the 2 components of every combination (2 PDRs or PDR + XDR), where the weights, or normalizations, are 2 free parameters; for PDR the normalization goes from 10^2 to 10^{10}, while for the XDR from 10^{-4} to 10^4, both grids with a $10^{0.1}$ step.

The free parameters are, for every model, 6: the 2 normalizations just introduced, the 2 total densities and the 2 incident fluxes (FUV or X). The degrees of freedom ν are defined as the difference between the number of observables, here the 13 CO line fluxes,

and the number of free parameters, 6. It is therefore useful to define the reduced χ^2 as the ratio χ^2/ν: the more this value is close to 1, the more the fit is good. A Python[5] minimization code has been developed to search, for each source, the minimum χ^2, cycling over all the normalizations for each simulation, and then over all the simulations (i.e. through the densities and fluxes listed in table 3.2); the code is available in appendix B.

CLOUDY computes the emerging CO SLED from PDR and XDR as fluxes per unit of emitting area, so it is a matter of choice on which surface integrate this flux to get a luminosity and then a flux observable at Earth distance, in order to compare it with the observed CO flux. In figure 3.2 is pictured our model: PDRs and XDRs are both spherical shells, the former containing small stellar clusters whose radiation G_0 impinges the inner side, the latter encompassing the AGN at the center of the galaxy and being internally stricken by its flux F_X. For every model the depth d of the shell is the one corresponding to the assumed column densities, and one has to choose an external radius R_{ext} in order to integrate the flux.

For the PDR model we decided to adopt a fixed inner radius $R_{in} = 10$ pc: with this uniform choice the integration radius is $R_{ext} = R_{in} + d$, where d is the cloud depth. These radii are perfectly scalable with the normalization factor N_{10} that comes out from the minimization code. N_{10}, to zero order, symbolizes the number of PDRs with average inner radius 10 pc. For every CO line, if F_{sim} is the CLOUDY simulated flux, the observable modeled flux F_{mod} at a Earth's luminosity distance D_L is:

$$F_{mod} = N_{10} \times \frac{4\pi(10 \text{ pc} + d)^2 F_{sim}}{4\pi D_L^2} = N \times \frac{4\pi R^2 F_{sim}}{4\pi D_L^2} \tag{3.2.2}$$

The observable modeled flux F_{mod} in practice doesn't change changing the factor NR^2, that works as an effective normalization factor. In the following sections the normalization constants are always given for $R_{in} = 10$ pc, that is to integrate the fluxes over a surface $4\pi R_{ext}^2 = 4\pi(10 \text{ pc} + d)^2$.

It is worthwile to note that assuming a distance 10 pc between the radiation source and the illuminated side of the PDR translates the incident flux G_0 into a FUV luminosity L_{FUV}. Remembering that $G_0 = 1$ corresponds to a FUV flux (i.e. integrated between 6 and 13.6 eV) $F_{FUV} = 1.6 \times 10^{-3}$ erg s^{-1} cm^{-2} (see section 1.2.3 for details):

$$L_{FUV} = 4\pi R^2 F_{FUV} = 4.91 \times 10^3 \left(\frac{R}{10\text{pc}}\right)^2 G_0 \, \text{L}_\odot \tag{3.2.3}$$

where the solar luminosity is $L_\odot = 3.9 \times 10^{33}$ erg s^{-1}.

So, for instance, a FUV flux $G_0 = 10^3$ (which is the median G_0 value in our simulations, as listed in table 3.2) corresponds to $L_{FUV} = 4.9 \times 10^6$ L$_\odot$, adequate for a stellar cluster.

Equation 3.2.2 is valid also for the XDR model, but in that case we have the luminosity constraint: a incident X-ray flux F_{inc} have to correspond to the galaxy X-ray

[5] https://www.python.org/

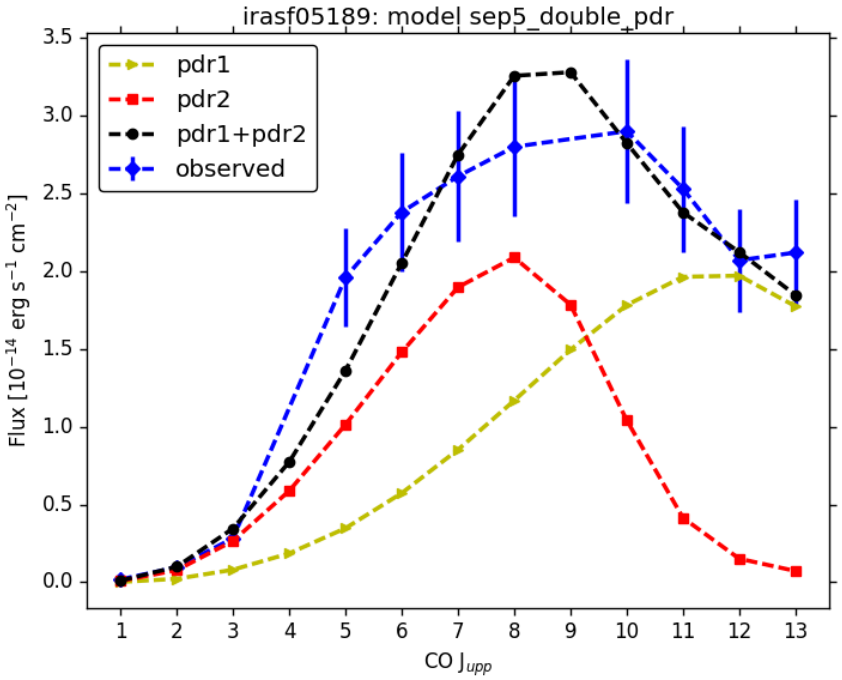

Figure 3.3: Observed and simulated CO SLEDs for galaxy IRAS F05189−2524. This is the best double PDR model selected by the minimization procedure.

luminosity L_X (last column in table 3.3) spread on a spherical shell with a inner radius R_{in}, and furthermore neither this radius nor the external radius R_{ext} of the cloud can be greater than the emission size observed by ALMA (section 2.3.3 and table 2.2).

From ALMA observations we can put an upper limit to the volume occupied by the simulated models, using the area of the CO-emitting region; since our models should reproduce the observed CO SLED, especially, in this galaxy sample, the dominant mid- and high-J transitions, we decided to use the minimum areas among the observed ones (listed in table 2.2). Assuming that galaxies are spherical with radius $R_{gal} = (A_{gal}/\pi)^{1/2}$, their volumes is simply $V_{gal} = 4\pi R_{gal}^3/3$. Since the simulated volume is $V_{comb} = 4\pi(N_1 R_{ext,1}^3 + N_2 R_{ext,2}^3)/3$, where N_1 and N_2 are the two normalizations, is possible to impose that the filling factor V_{comb}/V_{gal} of every combination of models must be less than 1. The minimization code takes into account these costraints; details on each galaxy are found to be in the next sections.

3.2.1 IRAS F05189-2524

IRAS F05189−2524 does not have a flux for the CO $J = 4 - 3$ line in literature, consequently there are only $\nu = 6$ degrees of freedom instead of 7. Moreover, the flux of CO $J = 9 - 8$ transition is oddly lower than the ones near it (see table 3.1), so we decided to exclude it, thereby downgrading the degrees of freedom to $\nu = 5$.

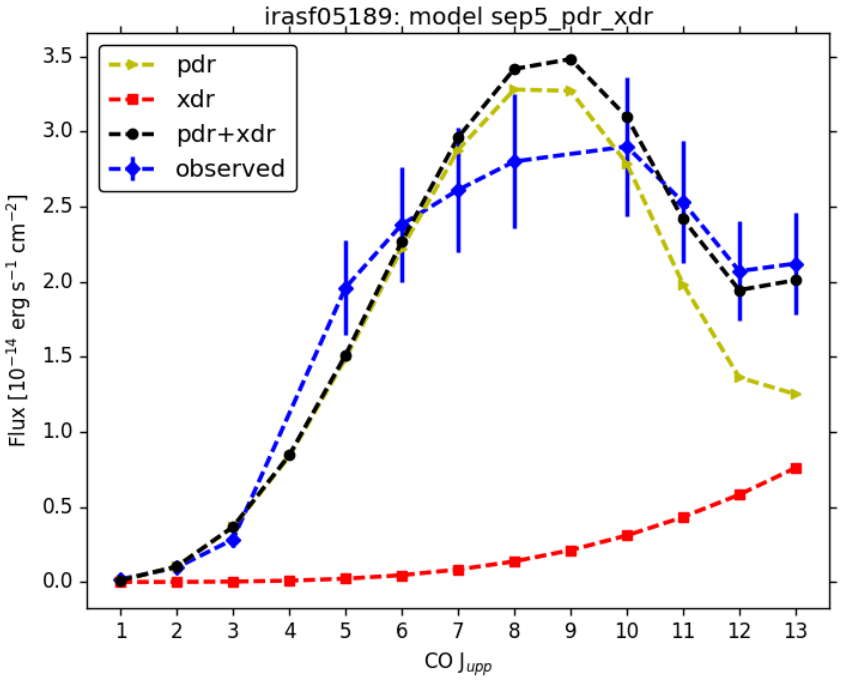

Figure 3.4: Observed and simulated CO SLEDs for galaxy IRAS F05189−2524. This is the best PDR + XDR model selected by the minimization procedure.

The best double PDR model (figure 3.3) is the combination of two dense PDRs, respectively with $n_H = 10^{5.5}$ cm^{-3}, $G_0 = 10^3$ and $n_H = 10^5$ cm^{-3}, $G_0 = 10^1$. The normalizations are respectively $10^{4.0}$ and $10^{5.0}$, and the model has a reduced $\chi^2_\nu = 3.00$. The cloud depths (corresponding to $N_H = 10^{22}$ cm^{-2}) are 2.8×10^{-4} pc for the first and 3.5×10^{-3} pc for the second PDR. The two PDRs have similar densities, so the different positions they occupy in figure 3.3 are due to the different radiation fields to which they are exposed. Even if they look similar in figure 3.3, the left one (PDR 2) has a mass 10 times greater (see table 3.4 for the mass estimates).

The best PDR + XDR model (figure 3.4) sees the combination of a dense PDR ($n_H = 10^{5.0}$ cm^{-3}, $G_0 = 10^5$, $d_{PDR} = 2.1 \times 10^{-3}$ pc), with a dense XDR ($n_H = 10^{4.5}$ cm^{-3}, $F_X = 1.4 \times 10^3$ erg s^{-1} cm^{-2}). Since the X-ray luminosity between 1 and 100 keV of IRAS F05189−2524 is $L_X = 4 \times 10^{44}$ erg s^{-1} (table 3.3), the distance AGN-XDR is 3.2 pc, while the XDR depth (corresponding to $N_H = 10^{23}$ cm^{-2}) is $d_{XDR} = 2.6 \times 10^{-2}$ pc. The normalizations are respectively $10^{5.1}$ and $10^{0.5}$. The XDRs are accounted mainly for the high-J transitions, but the CO SLED is dominated by the PDR component (figure 3.4); masses of the two models (table 3.4) are comparable. The reduced χ^2_ν is 2.98, which is slightly lower than the double PDR model: the PDR+XDR model is the best one for IRAS F05189−2524.

IRAS F05189−2524	Double PDR		PDR + XDR	
	PDR 1	PDR 2	PDR	XDR
n_H [cm^{-3}]	$10^{5.5}$	$10^{5.0}$	$10^{5.0}$	$10^{4.5}$
G_0 or F_X [erg s^{-1} cm^{-2}]	10^3	10^1	10^5	1.4×10^3
R_{in} [pc]	10	10	10	48.6
Cloud depth [pc]	2.8×10^{-4}	3.5×10^{-3}	2.1×10^{-3}	2.6×10^{-2}
Normalization	$10^{4.0}$	$10^{5.0}$	$10^{5.1}$	$10^{0.5}$
Total mass [M$_\odot$]	1.0×10^9	1.0×10^{10}	1.3×10^{10}	1.9×10^{10}
χ^2_ν	3.00		2.98	

Table 3.4: Best two models for galaxy IRAS F05189−2524. Second line contains incident flux as G_0 for the PDRs and as F_X, in units of erg s^{-1} cm^{-2}, for the XDR (last column). R_{in} is the inner radius of the spherical shell (for the PDRs this value is assumed to be always 10 pc), i.e. the average distance between it and the radiation source. Mass is calculated from data listed here using equation 4.1.2.

3.2.2 NGC 34

Also for the NGC 34 model the degrees of freedom are $\nu = 5$, because CO $J = 4 - 3$ line is again missing, and the CO $J = 10 - 9$ line has been excluded as outliers (see table 3.1).

The best double PDR model (figure 3.5) is a combination of two $n_H = 10^4$ cm^{-3} PDRs, respectively stricken by FUV fluxes $G_0 = 10^1$ and 10^4. At $N_H = 10^{22}$ cm^{-2} the cloud depths are respectively 3.5×10^{-3} pc and 1.6×10^{-3} pc. The normalizations are respectively $10^{3.9}$ and $10^{4.1}$, and the model has $\chi^2_\nu = 2.81$. Having the same densities and almost same normalizations, the difference between the two PDRs shown in figure 3.5 is only due to the different G_0.

The best PDR + XDR model (in figure 3.6) presents a dense PDR ($n_H = 10^5$ cm^{-3}, $G_0 = 10^5$, $d = 2.1 \times 10^{-3}$ pc) combined with a thick XDR ($n_H = 10^3$ cm^{-3}, $F_X = 4.5 \times 10^2$ erg s^{-1} cm^{-2}, $d = 1.3$ pc). The illuminated face of the XDR is distant 7.5 pc from an AGN with $L_X = 2.98 \times 10^{42}$ erg s^{-1} in the $1 - 100$ keV range (from table 3.3). Normalizations are $10^{4.4}$ in the PDRs case and $10^{2.6}$ for the XDRs. The χ^2_ν associated to this model is 2.93. The XDR component is almost invisible in figure 3.6, even if its mass is comparable to the PDR one (see table 3.5). Since it has a lower χ^2_ν, double PDR model is the best one (the associated probabilities are 73% and 71%).

3.2.3 NGC 4418

NGC 4418 is the only galaxy in our sample with an increasing CO SLED up to $J = 13 - 12$ (see figures 3.7 and 3.8). Although not detected in X-rays, the presence of a Compton-thick AGN (i.e. with $N_H > 10^{24}$ cm^{-2}) cannot be excluded.

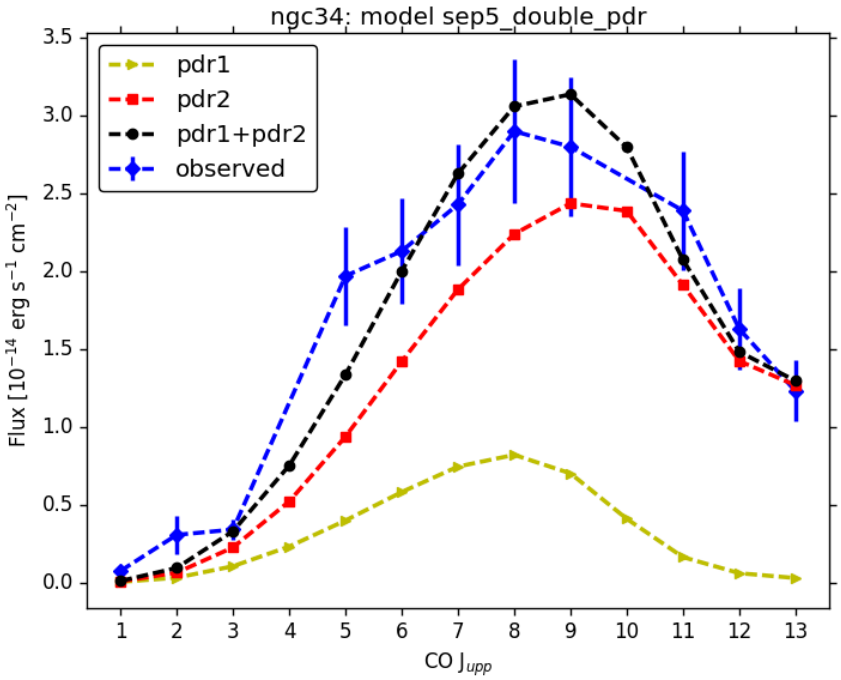

Figure 3.5: Observed and simulated CO SLEDs for galaxy NGC 34. This is the best double PDR model selected by the minimization procedure.

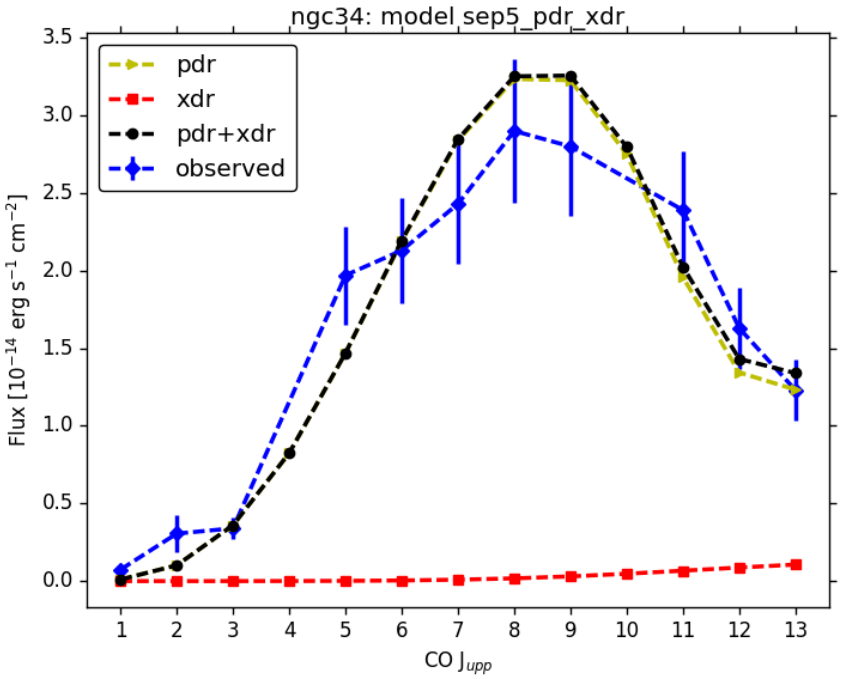

Figure 3.6: Observed and simulated CO SLEDs for galaxy NGC 34. This is the best PDR + XDR model selected by the minimization procedure.

NGC 34	Double PDR		PDR + XDR	
	PDR 1	PDR 2	PDR	XDR
n_H [cm^{-3}]	$10^{5.0}$	$10^{5.0}$	$10^{5.0}$	$10^{3.0}$
G_0 or F_X [erg s^{-1} cm^{-2}]	10^{1}	10^{4}	10^{5}	4.5×10^{2}
R_{in} [pc]	10	10	10	7.5
Cloud depth [pc]	3.5×10^{-3}	1.6×10^{-3}	2.1×10^{-3}	1.3
Normalization	$10^{3.9}$	$10^{4.1}$	$10^{4.4}$	$10^{2.6}$
Total mass [M$_\odot$]	8.0×10^{8}	1.3×10^{9}	2.5×10^{9}	4.9×10^{8}
χ^2_ν	2.81		2.93	

Table 3.5: Best two models for galaxy NGC 34. Second line contains incident flux as G_0 for the PDRs and as F_X, in units of erg s^{-1} cm^{-2}, for the XDR (last column). R_{in} is the inner radius of the spherical shell (for the PDRs this value is assumed to be always 10 pc), i.e. the average distance between it and the radiation source. Mass is calculated from data listed here using equation 4.1.2.

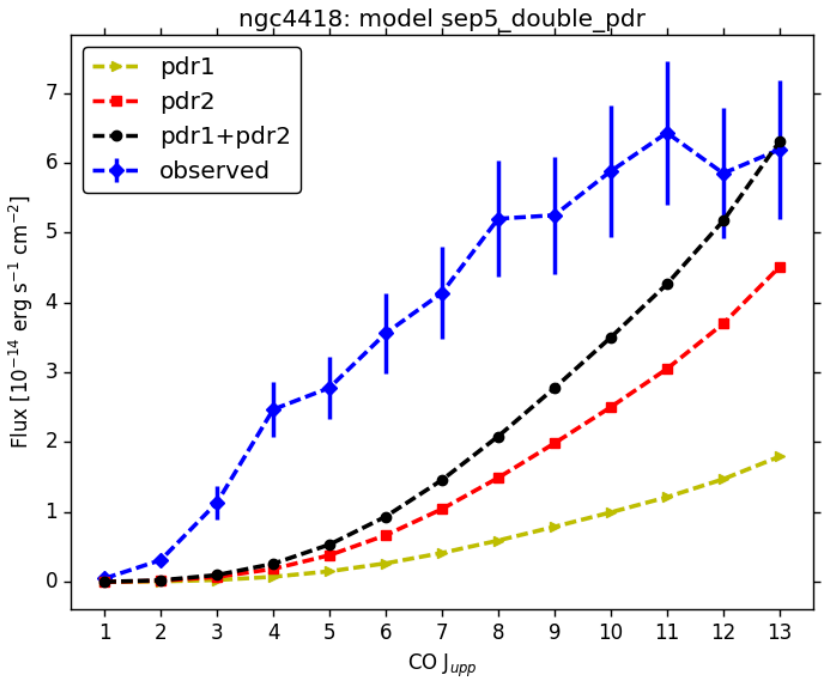

Figure 3.7: Observed and simulated CO SLEDs for galaxy NGC 4418. This is the best double PDR model selected by the minimization procedure.

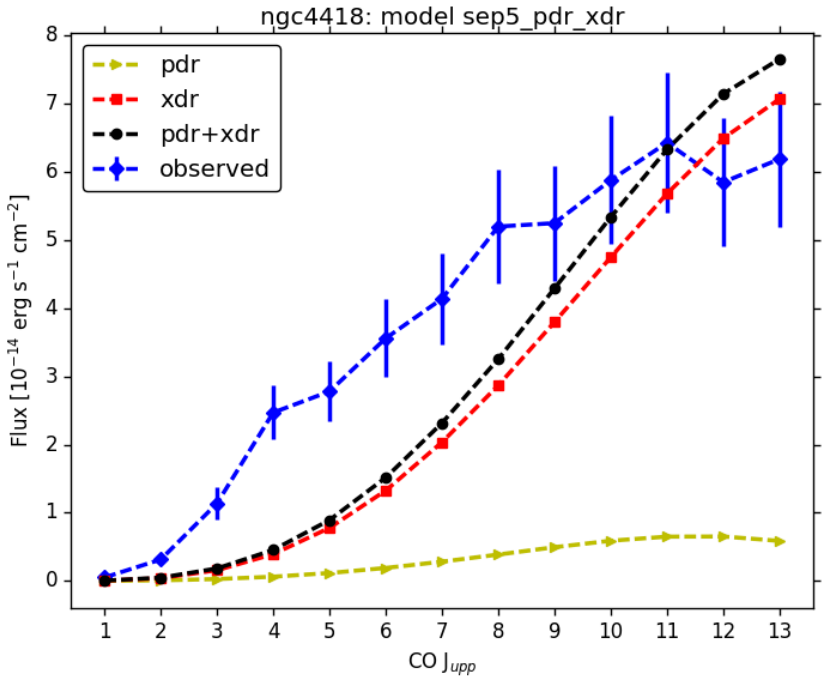

Figure 3.8: Observed and simulated CO SLEDs for galaxy NGC 4418. This is the best PDR + XDR model selected by the minimization procedure.

The best double PDR model for NGC 4418 (in figure 3.7) is actually a single PDR model, with $n_H = 10^{5.5}$ cm^{-3}, $G_0 = 10^5$ and cloud depth, measured at $N_H = 10^{22}$ cm^{-2}, equal to 4.0×10^{-4} pc. Assuming a inner radius of 10 pc, the total normalization factor is $10^{2.6}$. For this model $\chi^2_\nu = 24.14$. This galaxy has the big disadvantage to have a very small emitting area (1.8×10^4 pc^2 for CO $J = 6 - 5$) compared to the other observed objects (see table 2.2); this has limited a lot the minimization procedure, since the code (appendix B) discards all the normalizations that produce a model with filling factor greater than 1.

The PDR + XDR model is a combination of a $n_H = 10^{5.5}$ cm^{-3}, $G_0 = 10^3$ PDR, with normalization $10^{2.1}$ and depth 2.8×10^{-4} pc, and a $n_H = 10^{3.5}$ cm^{-3}, $F_X = 14.2$ erg s^{-1} cm^{-2}, 2.1 pc thick XDR. Since we have not found a value for the X-ray flux of NGC 4418 in literature, a fictitious luminosity $L_X = 10^{42}$ erg s^{-1} is assumed in the $1 - 100$ keV range. With this choice the distance AGN-XDR is 24.3 pc, and the normalization is $10^{1.4}$. This model has a $\chi^2_\nu = 15.76$, hence resulting the best among the two simulated. However, results for this galaxy have to be taken with caution, since the associated probability to this model is 2.7%.

3.2.4 NGC 6240

The best double PDR model is made of two dense PDRs ($n_H = 10^{5.5}$ and $10^{5.0}$ cm^{-3}) stricken by very different FUV fields (respectively $G_0 = 1$ and 10^4). For the first a

NGC 4418	Double PDR		PDR + XDR	
	PDR 1	PDR 2	PDR	XDR
n_H [cm^{-3}]	$10^{5.5}$	$10^{5.5}$	$10^{5.5}$	$10^{3.5}$
G_0 or F_X [erg s^{-1} cm^{-2}]	10^5	10^5	10^3	14.2
R_{in} [pc]	10	10	10	24.3
Cloud depth [pc]	4.0×10^{-4}	4.0×10^{-4}	2.8×10^{-4}	2.1
Normalization	$10^{2.1}$	$10^{2.5}$	$10^{2.1}$	$10^{1.4}$
Total mass [M$_\odot$]	1.3×10^7	3.2×10^7	1.3×10^7	1.1×10^8
χ^2_ν	24.14		15.76	

Table 3.6: Best two models for galaxy NGC 4418. Second line contains incident flux as G_0 for the PDRs and as F_X, in units of erg s^{-1} cm^{-2}, for the XDR (last column). R_{in} is the inner radius of the spherical shell (for the PDRs this value is assumed to be always 10 pc), i.e. the average distance between it and the radiation source. Mass is calculated from data listed here using equation 4.1.2.

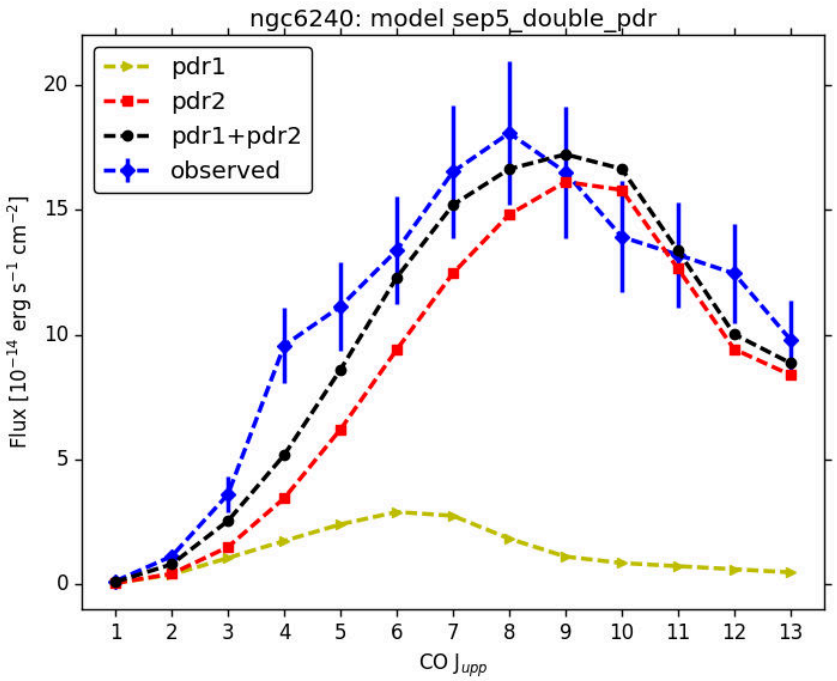

Figure 3.9: Observed and simulated CO SLEDs for galaxy NGC 6240. This is the best double PDR model selected by the minimization procedure.

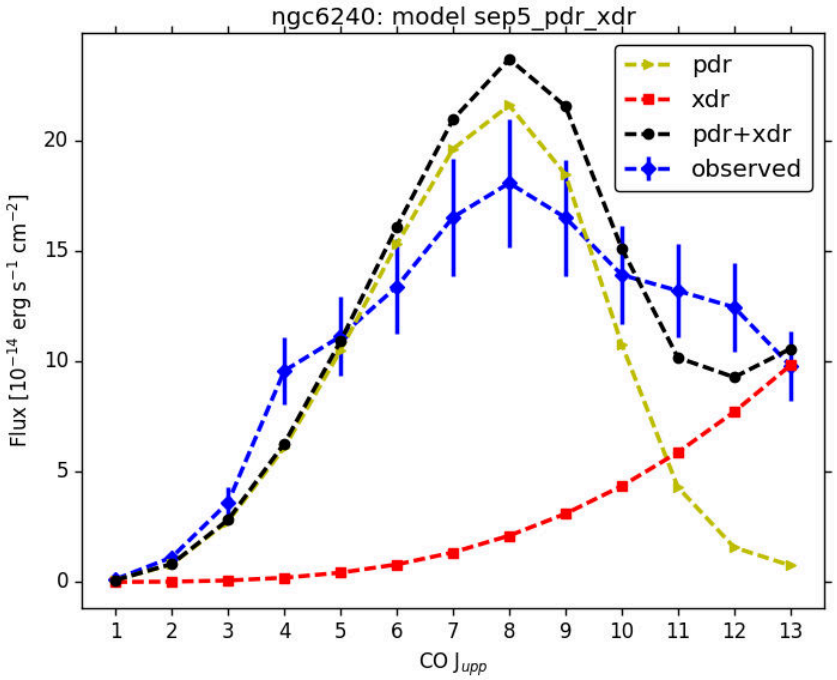

Figure 3.10: Observed and simulated CO SLEDs for galaxy NGC 6240. This is the best PDR + XDR model selected by the minimization procedure.

depth of 2.6×10^{-3} pc and a normalization $10^{5.4}$ comes from the minimization code, for the second the depth is 1.6×10^{-3} pc and normalization $10^{5.2}$. Reduced chi-square is $\chi^2_\nu = 4.27$. The PDR with the FUV flux comparable to the Galactic ISRF (PDR 1), despite its high density, makes only a small part of CO SLED fitting (figure 3.9); however its mass (see table 3.7) is a bit larger than the other PDR.

Also the PDR + XDR model combines dense clouds: the PDR has $n_H = 10^5$ cm^{-3} and $G_0 = 10$, the XDR $n_H = 10^{5.5}$ cm^{-3} and $F_X = 1.4 \times 10^3$ erg s^{-1} cm^{-2}. The PDR has normalization $10^{5.6}$ and is 3.5×10^{-3} thick. Taking into account the X-rays luminosity $L_X = 9.64 \times 10^{43}$ erg s^{-1} (from table 3.3), the AGN results to be 23.9 pc away from the XDR, which has a depth of 2.6×10^{-3} pc; normalization for the XDR is $10^{1.7}$. This model has a $\chi^2_\nu = 5.25$. The XDR best model, from figure 3.6, seems more appropriate for a flatter CO SLED, although we do not know how CO fluxes are after the CO $= 13 - 12$ one.

NGC 6240	Double PDR		PDR + XDR	
	PDR 1	PDR 2	PDR	XDR
n_H [cm^{-3}]	$10^{5.5}$	$10^{5.0}$	$10^{5.0}$	$10^{5.5}$
G_0 or F_X [erg s^{-1} cm^{-2}]	10^0	10^4	10^1	1.4×10^3
R_{in} [pc]	10	10	10	23.9
Cloud depth [pc]	2.6×10^{-3}	1.6×10^{-3}	3.5×10^{-3}	2.6×10^{-3}
Normalization	$10^{5.4}$	$10^{5.2}$	$10^{5.6}$	$10^{1.7}$
Total mass [M$_\odot$]	2.5×10^{10}	1.6×10^{10}	4.0×10^{10}	1.8×10^{10}
χ^2_ν	4.27		5.25	

Table 3.7: Best two models for galaxy NGC 6240. Second line contains incident flux as G_0 for the PDRs and as F_X, in units of erg s^{-1} cm^{-2}, for the XDR (last column). R_{in} is the inner radius of the spherical shell (for the PDRs this value is assumed to be always 10 pc), i.e. the average distance between it and the radiation source. Mass is calculated from data listed here using equation 4.1.2.

Chapter 4

Discussion of results

4.1 Molecular mass

In this section the molecular mass of the 4 galaxies is evaluated in two different ways: the first is from equation 1.2.1, using the luminosity of CO $J = 1 - 0$ line, and it is the traditional method of molecular mass estimation of galaxies (section 1.2.2); the other method takes advantage of our CO SLED fitting procedure, which have resulted in predictions about the number, size and density of molecular clouds.

Equation 1.2.1 is here rewritten converting the flux from Jy km s^{-1} to erg s^{-1} cm^{-2}:

$$M_{mol} = \frac{1.09 \times 10^{20}}{(1+z)} \left(\frac{D_L}{\text{Mpc}}\right)^2 \left(\frac{X_{CO}/(2 \times 10^{20})}{\text{cm}^{-2}(\text{K km s}^{-1})^{-1}}\right) \left(\frac{F_{CO\,(1-0)}}{\text{erg s}^{-1}\ \text{cm}^{-2}}\right) \tag{4.1.1}$$

with X_{CO} being the CO-to-H_2 conversion factor (see section 1.2.2). Another recurrent conversion factor is $\alpha_{CO} \equiv M_{mol}/L_{CO}$, and the corresponding value to $X_{CO} = 2 \times 10^{20}$ cm^{-2}(K km s^{-1})$^{-1}$, i.e. the average value found in the Milky Way, is $\alpha_{CO} = 4.3$ M$_\odot$ (K km s^{-1} pc^2)$^{-1}$. Note that equation 4.1.1 assumes virialized clouds that follow the Larson's size-line width relation (section 1.2.2) and have constant temperature (Bolatto et al. 2013), conditions that may not always be appropriate.

The total gas mass derived from the models, double PDR or PDR + XDR, is calculated from the column density $N_H = \int n_H dr$, being n_H from equation 3.1.3 and r the cloud depth. Both for PDR and XDR, given the normalization N, the external radius R and the column density N_H, the total mass of the clouds is:

$$M_{cloud} = N \times 4\pi R^2 N_H m_p \tag{4.1.2}$$

where $m_p = 1.67 \times 10^{-24}$ g is the proton mass. Also here, as for the observed flux (equation 3.2.2), the result depends on the product $N \times R^2$. Note that M_{cloud} is the total gas mass of the cloud, therefore including also ionized and neutral atomic gas (see figures 1.8 and 1.11 for an insight of the gas phases in these models).

Following the work of Gao et al. 2004b, we estimated also a dense molecular mass, corresponding to $n(H_2) \geq 3 \times 10^4$ cm^{-3}: this mass should be comparable to the one traced by the HCN $J = 1 - 0$ emission line observed by Gao et al. 2004b. We compared the dense masses of our best models with their results in figure 4.2. In table 4.1 these three masses are listed together with our estimate of α_{CO} (see next section 4.1.1).

Galaxy	M_{cloud}	M_{mol}	M_{dense}	α_{CO}
IRAS F05189−2524	3.2×10^{10}	1.7×10^{10}	1.83×10^{10}	8.09
NGC 34	2.1×10^{9}	1.4×10^{10}	2.02×10^{9}	0.65
NGC 4418	1.2×10^{8}	1.8×10^{9}	1.27×10^{7}	0.29
NGC 6240	4.1×10^{10}	4.4×10^{10}	4.05×10^{10}	4.01

Table 4.1: Gas masses for each galaxy. The first column is the total mass of the best model for each galaxy (see section 3.2 for details); column 2 shows the molecular mass computed from equation 4.1.1 using CO $J = 1 - 0$ luminosity and $\alpha_{CO} = 4.3$ $M_\odot$ (K km s^{-1} pc^2)$^{-1}$; third column is the dense mass, defined as the mass of the region of the cloud in which $n(H_2) \geq 3 \times 10^4$ cm^{-3}. The fourth column is our estimate for α_{CO} using the M_{cloud} masses. All the masses are in units of $M_\odot$, α_{CO} in $M_\odot$ (K km s^{-1} pc^2)$^{-1}$ units.

4.1.1 The CO-to-H_2 conversion factor

From our mass estimates is possible to calculate which conversion factor α_{CO} (see section 1.2.2 for details) should apply for our clouds, using equation 4.1.3:

$$\alpha_{CO} = 4.08 \times 10^{-4} \frac{(1+z)}{S_{CO}\Delta v D_L^2} M_{cloud} \tag{4.1.3}$$

where $S_{CO}\Delta v$ is the integrated line flux density in Jy km s^{-1}, D_L is the luminosity distance in Mpc and z is the redshift.

In the left graph of figure 4.1 the conversion factor α_{CO} of a sample of local spirals and ULIRGs is plotted against their total surface densities Σ (dominated by the stellar component, Bolatto et al. 2013); a fiducial $\Sigma^{-0.5}$ line for $\Sigma > 100$ M$_\odot$ pc^{-2} reasonably represent the observed trend.

In the right graph α_{CO} is correlated to the galaxy metallicity: higher values of the conversion factor are expected in low-metallicity galaxies, since in these environments lower C and O abundances and low dust-to-gas ratios are expected (so S_{CO} at the denominator of equation 4.1.3 decreases). Estimates for α_{CO} in both graphs use the dust optical depth τ_d that comes from IR emission modeling (see Bolatto et al. 2013 and references therein).

We plot our results (listed in table 4.1) as lines in figure 4.1 (left and right panels) since we are not in possess of total surface density and metallicity of our objects. A wide spread is present among the four galaxies, from ULIRGs typical values for NGC

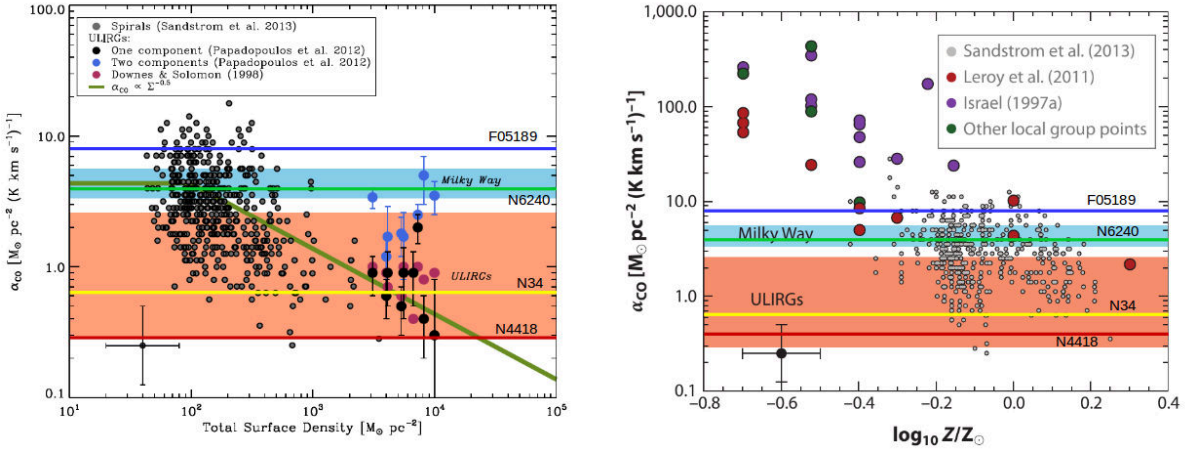

Figure 4.1: CO-to-H_2 conversion factor α_{CO} plotted against total surface density (left image) and metallicity (right image). Points are from galaxy samples written in legends and explained in detail in the Bolatto et al. 2013 review. Our 4 galaxies are represented here with straight colored tight lines, since we are not in possess of their total surface density and metallicity. The big colored bands show the recommended ranges in α_{CO} for the Milky Way and ULIRGs. Both taken from Bolatto et al. 2013, figures 12 (left) and 9 (right).

4418 ($\alpha_{CO} = 0.29$) and NGC 34 ($\alpha_{CO} = 0.65$), to 8.09 $M_\odot$ (K km s^{-1} pc^2)$^{-1}$ for IRAS F05189−2524: this last is highest than the Milky Way average but still in line with lots of other galaxies. Despite its disturbed appearance (figure 2.10) and high IR luminosity ($\log L_{IR} = 11.92$ in solar luminosities) NGC 6240 has the α_{CO} most similar (4.01 $M_\odot$ (K km s^{-1} pc^2)$^{-1}$) to the Galactic one. Results for NGC 4418 have to be taken with caution (see section 3.2 for details).

4.2 A dense Schmidt-Kennicutt relation

The Schmidt-Kennicutt relation, sometimes also called *star formation law*, is the relation between the gas content of a galaxy and its star formation rate (section 1.3.1). The most famous version of this relation, from the study of Kennicutt 1998, shows the SFR surface density as function of the gas surface density, intending both neutral atomic and molecular gas (namely HI + H_2), like in figure 1.14.

Here we have plotted the SFRs (calculated from their IR luminosity, both listed in table 2.1), as function of the dense mass, listed in table 4.1: following the same argument of Gao et al. 2004b, from which the original plot is taken, it is expected that the dense part of the molecular gas is the main responsible for star formation, so it makes more sense to focus on it.

In their work, Gao et al. 2004b used the HCN $J = 1 - 0$ luminosity, a known tracer

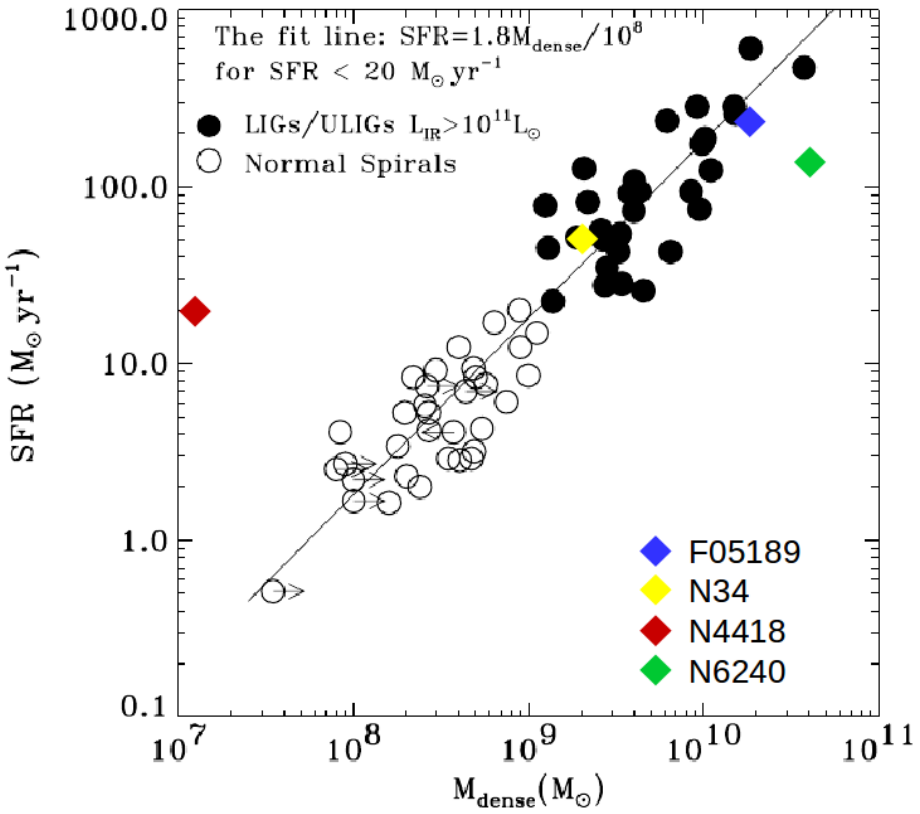

Figure 4.2: Schmidt-Kennicutt relation with dense molecular masses. The original Gao et al. 2004b sample contains 53 galaxies, of which 25 (U)LIRGs, and their M_{dense} have been calculated from HCN $J = 1 - 0$ luminosity. Our modeled M_{dense} are computed for the gas with $n(H_2) \geq 3 \times 10^4$ cm^{-3}. SFRs of our sample are from table 2.1. Adapted from figure 6 of Gao et al. 2004b.

of dense molecular gas (see section 1.1.3) from both normal star-forming galaxies and (U)LIRGs. They assumed a conversion factor $\alpha_{HCN} = 10$ M$_\odot$ (K km s^{-1} pc^2)$^{-1}$ (details are in Gao et al. 2004a, another paper of the same authors), valid for the densities in which they expect the HCN $J = 1 - 0$ to emit, namely $n(H_2) \geq 3 \times 10^4$ cm^{-3}.

With these prescriptions the SFRs result directly proportional to the dense mass of the galaxies (figure 4.2), instead of being fitted by a $n = 1.4$ power-law (like Kennicutt 1998), and instead of showing separate and parallel correlations for normal and starburst galaxies (like Daddi et al. 2010, see section 1.3.1). Lada, Forbrich, et al. 2012 found that also the Galactic molecular clouds follow the same relation.

In figure 4.2 our dense masses (listed in table 4.1) are plotted along with the Gao et al. 2004b sample. For IRAS F05189−2524 and NGC 34 the dense masses correlate very well with the original sample; the former has a $M_{dense}/M_{tot} \approx 0.6$ and $M_{mol} \approx M_{dense}$, so in this case the CO $J = 1 - 0$ luminosity seems a good tracer of dense gas; conversely, NGC 34 has $M_{dense}/M_{tot} \approx 1$ and $M_{dense}/M_{mol} \approx 0.14$, hence the CO $J = 1 - 0$, as expected, is tracing a lot of diffuse molecular gas, and our model contains only the densest part.

The dense mass of NGC 6240 seems overestimated (or its SFR underestimated, but in this case it would be $\sim 10^3$ that is unusually high in the local Universe): actually the mass is calculated for a combination of 2 PDRs of densities $10^{5.5}$ and 10^5 cm^{-3}, but these values are approximately the same of IRAS F05189−2524 and NGC 34, where M_{dense} is in agreement with Gao et al. 2004b; the main difference with them is that in this case the CO SLED fit is not so good ($\chi^2_\nu = 4.3$ against 3.0 and 2.8).

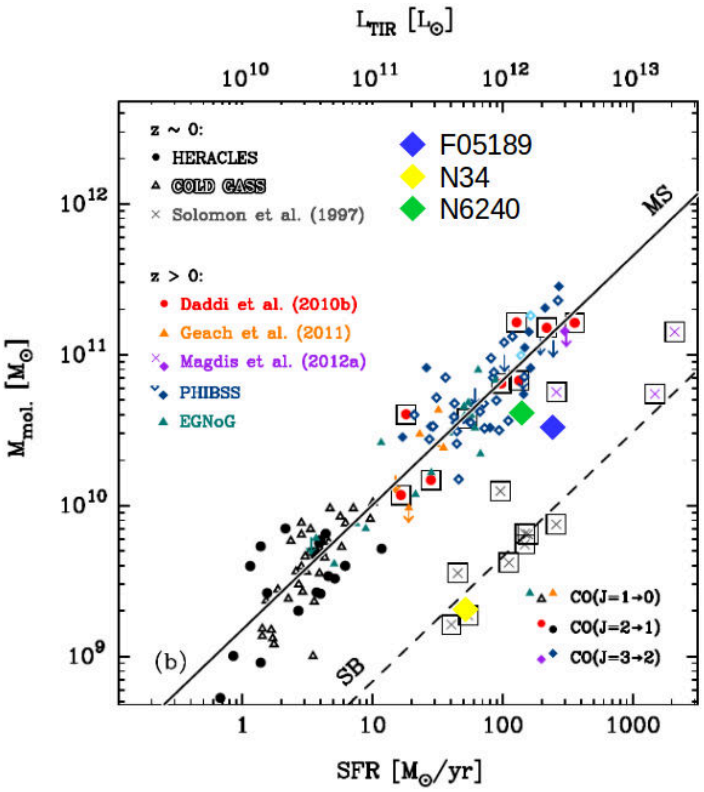

Figure 4.3: Inverse Schmidt-Kennicutt relation with Sargent et al. 2014 combination of samples and our four galaxies. Solid line is a fit of normal star-forming galaxies, dashed line is just its parallel that pass through starburst galaxies. M_{mol} from our sample are the one listed in table 4.1; SFRs from table 2.1. Adapted from figure 2b of Sargent et al. 2014.

The results of NGC 4418, as seen in section 3.2, should be taken with a lot of caution. Its low SFR (20 $M_\odot$ yr^{-1}) makes it a transition object between normal spirals and LIRGs, but the very low dense mass here is patently underestimated, and almost certainly its total mass is a lower limit too. NGC 4418 is the only galaxy in our sample with a mass component that has no dense component: its XDR model has $n_H = 10^{3.5}$ cm^{-3} and never reaches 3×10^4 cm^{-3}.

We also report the inverse Schmidt-Kennicutt relation (which is the same relation but with the axes switched) with our total gas masses as functions of SFRs (figure 4.3). The original plot is from Sargent et al. 2014, and contains data from several surveys (see the legend in figure 4.3). The solid line is the best-fit for the main-sequence (MS) of star-forming galaxies, while the dashed line is just drawn as parallel to the first and moved in order to pass through the starburst (SB) sample (the crosses from Solomon et al. 1997).

In the work of Sargent et al. 2014, SFRs are taken from the total IR luminosity (reported on the upper x-axis), while the molecular mass comes from CO luminosities with the adoption of a Z-dependent α_{CO} (with Z being the metallicity of the galaxy).

Our galaxies, with masses M_{cloud} estimated from our models (first column of table 4.1) and SFRs from L_{IR} (table 2.1), have been overplotted to figure 4.3. The results follow the same pattern of figure 4.1: IRAS F05189−2524 and NGC 6240 behave like normal spirals, NGC 34 like a starburst LIRG and NGC 4418 (out of the plot because of its very low gas mass) a extreme LIRG.

How to connect the single correlation seen in figure 4.2 with the two distinct sequences of figures 1.14 and 4.3? The hypothesis made by Gao et al. 2004b and sustained by Lada, Forbrich, et al. 2012 is that if instead of molecular mass (or total gas mass) we use only the denser part of it, the normal galaxies will move towards the starburst sequence (characterized by a lower normalization in figure 4.3) flattening it to a linear correlation. So the bimodality of star formation in galaxies would be just a bimodality in dense gas fraction f_{DG}: the main sequence galaxies have $f_{DG} \sim 0.1$ while (U)LIRGs have a $f_{DG} \to 1$ for increasing M_{mol} (Lada, Forbrich, et al. 2012).

4.3 Depletion time

In this section the depletion times of our galaxies are estimated on the basis of the SFRs listed in table 2.1 and the total gas masses in table 4.1 (first column) as estimated by our modeling. The depletion time is defined as $\tau_{depl} \equiv M_{mol}/SFR$, and it represents the time that it would take for a system with a given molecular mass content to burn it all in the star formation process.

In figure 4.4 the depletion time as a function of SFR is plotted. The original figure is taken from Sargent et al. 2014, and contains the same galaxies of figure 4.3. Again two sequences are clear, with normal star-forming galaxies characterized by $\tau_{depl} \gtrsim 0.7$ and (U)LIRGs with $\tau_{depl} \lesssim 0.2$.

Our galaxies follow again the same pattern found in figure 4.1 and especially in figure 4.3: NGC 6240 and IRAS F05189 with τ_{depl} typical of main-sequence galaxies (respectively $\tau_{depl} = 3.2 \times 10^8$ and 1.6×10^8 yr) and NGC 34, with $\tau = 4 \times 10^7$ yr, that makes it a typical starburst galaxy.

If the CO SLED fit of NGC 4418 has some meaning, its depletion time would be $\tau = 6.3 \times 10^6$ yr, equal to the average lifetime of a O star. This would make NGC 4418 a perfect candidate for the formation of a massive elliptical galaxy with quenched star formation due to exhaustion of molecular gas reservoir.

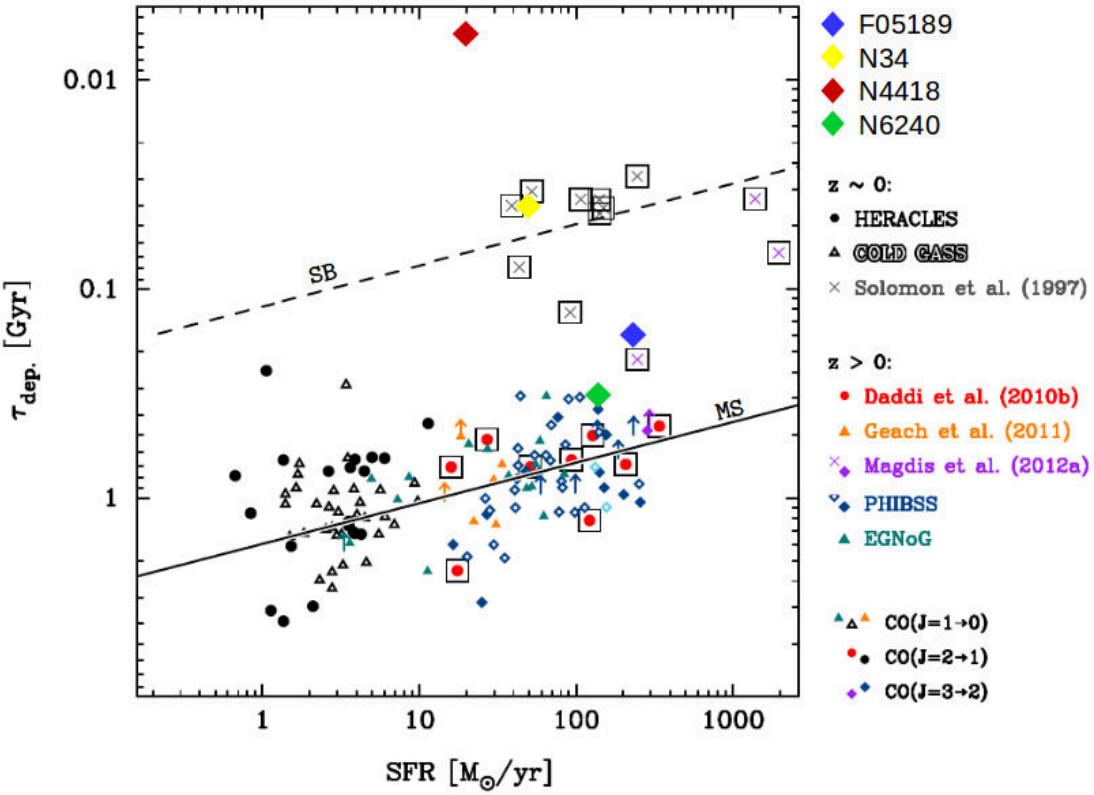

Figure 4.4: Depletion timescales against SFRs of our galaxy models combined with the full sample analyzed by Sargent et al. 2014 (the same of figure 4.3). Solid and dashed lines are the same ones rescaled from figure 4.3, showing the different but parallel correlations for main sequence and starburst galaxies. Adapted from figure 7 of Sargent et al. 2014.

4.4 Summary and future perspectives

The aim of this thesis work is to disentangle the dominant process (star formation or AGN) that drives the ISM physics. With this aim we have built a model capable of interpreting the CO spectral line energy distribution (SLED) of a galaxy as a combination of emission from a photo-dissociation region (PDR) and an X-ray dissociation region (XDR), the former being excited by a young stellar population, the latter being excited by an active galactic nucleus (AGN). Here the works is reassumed by its different steps.

1. We have selected local luminous IR galaxies (LIRGs or ULIRGs) from a Herschel-based survey, HerCULES (section 2.1)), in which the galaxies CO SLEDs had been observed from CO $J = 4-3$ up to $J = 13-12$. Only the galaxies with a CO SLED peak at high J_{upp} (around $J = 9-8$ or at greater energies) have been selected, i.e. the ones with a potential AGN excitation mechanism.

2. From the ALMA Archive all the observations of ^{12}CO in these galaxies have been downloaded; we have produced, for every available CO data-cube, a CO map (section 2.3.2) in order to measure the emitting area within a 3σ threshold in flux; the final galaxy sample consists of 4 galaxies (with a CO SLED that peaks at high-J observed by Herschel and CO data-cubes by ALMA: IRAS F05189−2524, NGC 34, NGC 4418 and NGC 6240.

3. Using the output of two grids of simulations (one for PDRs, the other for XDRs) computed with the spectral synthesis code CLOUDY (section 3.1.1), the observed CO SLEDs have been fitted by two types of model combinations: double PDR model or PDR + XDR model. The models use cumulative fluxes simulated by CLOUDY at cloud column densities 10^{22}, 10^{23} cm^{-2} (respectively for PDRs and XDRs) and have 6 free parameters: the two densities, incident fluxes and normalizations. A stringent constraint on the best-fit models has been imposed by the ALMA maps: the model CO-emitting region has to be lower than the volume of a sphere with radius $(A/\pi)^{1/2}$, with A being the CO emitting area seen by ALMA.

4. From the best-fitting models the dominant ISM excitation mechanism (star formation or black hole accretion) has been derived.

5. Finally the model gas masses have been estimated. The gas masses, together with the star formation of the galaxies, have been used to estimate the CO-to-H_2 conversion factors ($\alpha_{CO} \equiv M_{mol}/L_{CO}$) and the depletion times ($\tau_{depl} \equiv M_{mol}/SFR$) in order to put the galaxies studied in this thesis in a more general context.

The resulting best models are the double PDR for NGC 34, NGC 6240 and the PDR + XDR for IRAS F05189, NGC 4418. In the case of IRAS F05189 and NGC 34, the two computed models combinations are really similar on the basis of their reduced χ^2_ν (2.98 against 3 for the first galaxy, 2.8 against 2.9 for the second) and calculated masses. The minimization procedure found, indeed, a significant difference for the two models in

NGC 6240: reduced χ^2_ν correspond to a double PDR probability of 74% against 64% for PDR + XDR. Results for NGC 4418 have to be taken with a lot of caution, given the high values of χ^2_ν (15.8 and 24.1).

From the comparison of our results with other galaxy samples emerges that NGC 34 behaves like a typical starburst galaxy (with $\tau_{depl} = 4 \times 10^7$ yr), while IRAS F05189 and NGC 6240 seem more in a transition area between starburst and normal star-forming galaxies ($\tau_{depl} = 1.6 \times 10^8$ and 3.2×10^8 yr respectively). In every case the AGN radiation does not seem to dominate the observed CO SLEDs, which can be easily interpreted as excited by stellar radiation.

In the future, from the observational side, it would be interesting to enlarge the sample and apply this procedure, tested in detail for 4 galaxies, to a larger statistical sample, including also galaxies characterized by a different CO SLED, i.e. galaxies in class I and II (reported in figure 2.1). Moreover, other molecules (observed with ALMA) can be taken into account in the modeling, like HCN or HCO^+, known dense gas tracers given their high dipole moment ($\mu_{HCN} = 3.0$D and $\mu_{HCO^+} = 3.9$ D).

From the simulation side, it would be interesting to exploit all the CLOUDY potentialities, like the possibility of including turbulence and self-gravity. Finally, another challenging goal would be the inclusion of mechanical heating (a clue to shocks) together with photon-heating considered in this thesis.

Acknowledgements

Many thanks are owed to Livia Vallini for the useful suggestions and comments. We thank Giovanni Baldini, Gian Maria Cammerucci, Filippo Fraternali, Helena Girotto, Tiziana Ibba, Cristina Nanci, Rosita Paladino and Bruno Piga for helpful discussions and suggestions.

This thesis makes use of the following ALMA data: ADS/JAO.ALMA#2012.1.00306.S, ADS/JAO.ALMA#2013.1.00814.S, ADS/JAO.ALMA#2011.0.00182.S, ADS/JAO.ALMA-#2012.1.00377.S, ADS/JAO.ALMA#2013.1.00813.S, ADS/JAO.ALMA#2015.1.00370.S. ALMA is a partnership of ESO (representing its member states), NSF (USA) and NINS (Japan), together with NRC (Canada), MOST and ASIAA (Taiwan), and KASI (Republic of Korea), in cooperation with the Republic of Chile. The Joint ALMA Observatory is operated by ESO, AUI/NRAO and NAOJ.

This research has made extensive use of the NASA/IPAC Extragalactic Database (NED) which is operated by the Jet Propulsion Laboratory, California Institute of Technology, under contract with the National Aeronautics and Space Administration.

All atomic and molecular data, like frequencies and Einstein coefficients, are taken from the National Institute of Standards and Technology (NIST). Kramida, A., Ralchenko, Yu., Reader, J. and NIST ASD Team (2016). NIST Atomic Spectra Database (version 5.4), [Online]. Available: http://physics.nist.gov/asd [Sun Aug 20 2017]. National Institute of Standards and Technology, Gaithersburg, MD.

Appendices

Appendix A

CLOUDY input script

Here is the CLOUDY input script for the PDR grid. Every line that begins with a # sign is treated as comment and ignored by CLOUDY. The script ends and is computed by CLOUDY at the first empty line. For details about the physics involved and the choices made see sections 3.1.2 and 3.1.3.

```
### CLOUDY code
### PDR modeling grid
### Federico Esposito, Bologna, may 2017
#
title "PDRs grid for CO SLEDs interpretation"
#
background
table star "starburst_sfr80.mod" age=1e7 years
#
intensity -2.8 vary, range 0.44 to 1 Ryd
grid range from -2.8 to 3.2 with 1 dex steps
#
hden 1.5 vary
grid range from 1.5 to 5.5 with 0.5 dex steps
#
cosmic ray rate -16.3
magnetic field tangled -3.5 1.33
constant pressure
#
abundances ISM
grains PAH
#
stop temperature off
stop column density 23
failures 2
```

```
iterate to convergence
#
save grid "pdr_grid.grd"
save overview "pdr_grid.ovr" last separate
save pdr "pdr_grid.pdr" last separate
save pressure "pdr_grid.prs" last separate
save continuum "pdr_grid.con" units micron last separate
save lines cumulative "pdr_grid.cum" last separate
CO  2600m
CO  1300m
CO  866.7m
CO  650.1m
CO  520.1m
CO  433.4m
CO  371.5m
CO  325.1m
CO  289.0m
CO  260.2m
CO  236.5m
CO  216.9m
CO  200.2m
end of lines
```

The first thing to set up is the radiation field: `background` set both the shape and the intensity of the cosmic background, from radio wavelengths to X-rays, including the CMB; `table star` imports the stellar SED, which in our simulations is a Starburst99 model.

The `intensity` command set the incident flux in logarithmic cgs units, so -2.8 corresponds to $10^{-2.8}$ erg s^{-1} cm^{-2} $= 1.6 \times 10^{-3}$ erg s^{-1} cm^{-2}. It is possible to specify the `range` in Rydberg units (1 Ryd = 13.6 eV) in which this flux is integrated. It is important to write the `intensity` line just after the corresponding radiation shape command (which is `table star` in this case). The command *vary* is used only in case of grids of simulations.

The initial density of the cloud is specified by the `hden` command, always in cgs logarithmic units. The definition of this n_H is equation 3.1.3.

`cosmic ray rate` is the logarithm of the hydrogen ionization rate in s^{-1}; the `magnetic field` command needs details about its geometry (in our case `tangled`, in opposition to `ordered`) and strength: the two numbers here specified are $\log B_0$ and γ, and the resulting magnetic field is a function of gas density ρ: $B = B_0(\rho/\rho_0)^{\gamma/2}$.

The `constant pressure` command forces CLOUDY to gradually adjust the gas density in order to fulfill this requirement; total pressure is defined in equation 3.1.2.

Several chemical abundances and dust grains functions are stored in CLOUDY: here we chose the `ism` set (that includes the grains) and added the PAHs (which are not included by default).

By default CLOUDY stops the execution if the kinetic temperature drops below 4×10^3 K, so we turned of this behaviour. Our stopping criterion is instead the column density (in logarithmic cm^{-2} units).

When the heating-cooling balance or the constancy of pressure do not converge, a failure occurs. Since it is very difficult for the code to converge after more than 2 attempts, the command `failures 2` is there to save computational time.

The command `iterate to convergence` forces the code to repeat the execution until relative optical depths have changed by less than 0.20 between the last two iterations; optical depths are particularly important in presence of optically thick lines, like the CO $J = 1 - 0$ (section 1.2.2). The default maximum number of iterations is 10.

The last section of the code contains only instructions for the output files. By default CLOUDY produces only a `.out` file, which contains lots of informations about all the simulated chemical compounds and a summary of iterations made, with, if present, problems, cautions and notes. The command `last` save only the last iteration made, while the `separate` instruction is needed in case of grid simulations in order to produce a separate file for each grid member.

The `grid` file is just a summary of the simulated grid. `overview` and `pdr` contain the behaviour of quantities like gas density, temperature, chemical fractions and visual extinction expressed in function of cloud depth; figures 1.8 and 1.11 are made from these files. `pressure` divides the total pressure in its different components (the important ones in our simulations are the ones that appear in equation 3.1.2), again in function of cloud depth. The `continuum` file contains several spectra, among which incident, reflected and transmitted continuum, both alone and with atomic and molecular lines.

Last but not least, the `lines cumulative` output reports the cumulative fluxes of emission lines in function of cloud depth; the lines has to be listed just after this `save` command, and has to finish with a command that starts with the word `end`. This output has been used extensively in this thesis (in figures 1.9 and 1.12 for instance) since it contains the computed CO SLED.

Appendix B

Python minimization code

```
# Federico Esposito, Bologna, august 2017


import numpy as np
import os, sys
import itertools
from scipy.constants import pi
from scipy.constants import parsec # SI units
pc = parsec*1.e2


### STARTERS
gal = int(sys.argv[1])
prj = int(sys.argv[2])
galaxy = ['irasf05189', 'ngc34', 'ngc4418', 'ngc6240'][gal]

minimize_name = 'test'

pdr_norms = np.arange(2., 8., 0.1)
xdr_norms = np.arange(-4., 4., 0.1)
pdr_xdr_columns = [1e22, 1e23]
pdr_xdr_cases = ['int', 'lum']
os.chdir('/home/federico/Tesi/cloudy/')


### FUNCTIONS

def import_setlist(project):
  # in both models we deal with 2 parameters for each cloud
  n_par = 2
```

```
  # import the setlist with the 'success' column
  sl_complete = np.genfromtxt(
    fname = './' + project + '/' + project + '_setlist',
    dtype = 'U99, ' + 'float, '*n_par + 'int'
    )
  # new array without failures (last column = 0)
  success = sl_complete[sl_complete.dtype.names[-1]]
  sl = sl_complete[np.where(success != 0)]
  # generate a new np.array without that last column
  cols = []
  for i in range(len(sl.dtype.names)-1):
    cols.append(sl.dtype.names[i])
  setlist = sl[cols]
  # generate a new array with condition G0 <= 10^5
  G0 = setlist['f2']
  setlist = setlist[np.where(G0 != 3.2)]
  # list of CLOUDY parameters
  params_long = np.zeros([n_par, len(setlist)])
  params = []
  for p in range(n_par):
    params_long[p] = [ x[p+1] for x in setlist ]
    params.append( np.unique(params_long[p]) )
  return setlist, params


def import_galaxy(galaxy):
  if galaxy == 'irasf05189':
    lum_dist = 187*1e6*pc
    A_max = 2.48e6
    A_min = 2.48e6
    Lx = 4e44
    res_min = 335*pc
  elif galaxy == 'ngc34':
    lum_dist = 84.1*1e6*pc
    A_max = 0.488e6
    A_min = 3.06e5
    Lx = 2.98e42
    res_min = 64*pc
  elif galaxy == 'ngc4418':
    lum_dist = 36.5*1e6*pc
    A_max = 4.796e6
    A_min = 1.84e4
    Lx = 1e42
    res_min = 30*pc
  elif galaxy == 'ngc6240':
    lum_dist = 116*1e6*pc
```

```
    A_max = 17.6e6
    A_min = 1.87e6
    Lx = 9.64e43
    res_min = 200*pc
  # CO observed fluxes
  co_obs = np.loadtxt(
    fname = '../co_obs/co_obs_' + galaxy,
    comments = '#',
    usecols = [1,2])[:13]
  nans = np.array([x[0] for x in np.argwhere(np.isnan(co_obs))])
  co_select = np.delete(np.arange(len(co_obs)), nans)
  return lum_dist, co_obs, co_select, Lx, res_min, A_min


def generate_combo_name(combo):
  mod1_file, mod2_file = [str(x[0]) for x in combo]
  mod1_code = mod1_file[11:-4]
  mod2_code = mod2_file[11:-4]
  c_name = mod1_code + '__' + mod2_code
  return c_name


def generate_combo_matrix(mod1_sl, mod2_sl, out_dir):
  combo_matrix = list(itertools.product(mod1_sl, mod2_sl))
  if not os.path.exists(out_dir): os.makedirs(out_dir)
  galaxy = out_dir.split('_')[-1][:-1]
  matrix_file = out_dir[2:-(len(galaxy)+1)] + 'matrix_' + galaxy
  with open (out_dir + matrix_file, 'w') as f:
    # first header
    head = '#    ' + 'combo_name'.ljust(24)
    head = head + 'mod1_h mod1_F mod2_h mod2_F'
    f.write(head)
    for c in range(len(combo_matrix)):
      combo = combo_matrix[c]
      params = list(itertools.chain(
        *[(x[1], x[2]) for x in combo]))
      c_name = generate_combo_name(combo)
      f.write('\n' + str(c).ljust(5) + c_name + '   ')
      f.write('   '.join([str(x) for x in params]))
    f.write('\n#' + '-'*70 + '\n'*3)
    # second header for complete matrix with results
    f.write(head)
    f.write('    chi2     mod1_d      mod1_N')
    f.write('    mod2_d    mod2_N')
  return combo_matrix
```

```
def select_combos(combo_matrix, galaxy, projects, columns):
  # if Lx == 0. every combo will be selected
  Dl, co_obs, co_select, Lx, res_min, A = import_galaxy(galaxy)
  if projects[1][:3] == 'xdr':
    flux_select = []
    for c in range(len(combo_matrix)):
      combo = combo_matrix[c]
      # define flux at cloud illuminated surface
      radius = 10**(combo[1][2])
      flux = 10**42.23/(4*pi*radius**2)
      # find cloud depth
      idx = nearest_column(columns[1], combo[1], projects[1])
      xdr_dir = './' + projects[1] + '/'
      xdr_model = import_co_model(xdr_dir + combo[1][0])
      depth = xdr_model[idx][0]
      # impose a flux_min with R_in = D_max - depth
      D_max = pc*np.sqrt(A/pi)/2. - depth
      flux_min = Lx/(4*pi*D_max**2)
      if flux >= flux_min:
        flux_select.append(c)
  else:
    flux_select = range(len(combo_matrix))
  return flux_select


def import_co_model(datafile):
  # co_model[0] = row of file.cum
  # co_model[:,0] = depths column
  # co_model[:,j] = j-th CO line column
  co_model = np.loadtxt(
    fname = datafile,
    comments = '#',
    usecols = range(14)
    )
  return co_model


def nearest_column(coldens, half_combo, project):
  coldens_file = str(half_combo[0]).replace('.cum', '.pdr')
  coldens_file = './' + project + '/' + coldens_file
  coldens_model = np.loadtxt(fname = coldens_file, usecols = [1])
  idx = np.abs(coldens_model - coldens).argmin()
  return idx
```

```
def volumes(galaxy, current_norms, projects, mods, combo):
  # galaxy volume from ALMA CO-emitting area
  Dl, co_obs, co_select, Lx, res_min, A = import_galaxy(galaxy)
  V_gal = (4/3.)*pi*(A/pi)**(3/2.)
  # volumes from models
  vol_mods = []
  for i in range(2):
    N = 10**current_norms[i]
    d = mods[i][0]
    if projects[i][:3] == 'pdr':
      V = N*(4/3.)*pi*(10 + d/pc)**3
    if projects[i][:3] == 'xdr':
      radius = 10**(combo[i][2])
      R_in = radius*np.sqrt(Lx/10**42.23)
      V = N*(4/3.)*pi*((R_in + d)/pc)**3
    vol_mods.append(V)
  V_combo = sum(vol_mods)
  return (V_combo < V_gal)


def scale_the_line(model_row, line, norm, Dl, cloudy_class):
  logD = np.log10(Dl)
  if cloudy_class == 'int': # intensity case
    logR = np.log10(10*pc)
    logmod = norm + model_row[line] + 2*(logR - logD)
  if cloudy_class == 'lum': # luminosity case
    logmod = norm + model_row[line] - np.log10(4.*pi) - 2*logD
  return logmod


def scale_the_ladder(co_ladder, depth, norm, Dl, cloudy_class):
  logD = np.log10(Dl)
  if cloudy_class == 'int': # intensity case
    logR = np.log10(10*pc)
    log_constant = norm + 2.*(logR - logD)
  if cloudy_class == 'lum': # luminosity case
    log_constant = norm - np.log10(4.*pi) - 2*np.log10(Dl)
  logmod = [co_line + log_constant for co_line in co_ladder]
  return np.array(logmod)


def chi_pair(mods, norms, cases, galaxy):
  Dl, co_obs, co_select, Lx, D_max, A = import_galaxy(galaxy)
  chi2 = 0.
  for m in co_select:
    obs = co_obs[:,0][m]
```

```
    err = co_obs[:,1][m]
    log1 = scale_the_line(mods[0], m+1, norms[0], Dl, cases[0])
    log2 = scale_the_line(mods[1], m+1, norms[1], Dl, cases[1])
    comb_model = 10**log1 + 10**log2
    chi2 = chi2 + ((obs - comb_model)/err)**2
  return chi2


def save_chi_matrix(chi_matrix, combo, out_dir):
  np.savetxt(
    fname = out_dir + generate_combo_name(combo) + '.chi',
    X = chi_matrix,
    fmt = '%.2e')


def find_best(best_array, chi2, idcs):
  chi2_min = best_array[0]
  if chi2 < chi2_min:
    best_array[0] = chi2
    best_array[1] = idcs
  return best_array


def chi2_minimize(
  combo, columns, norms, cases, out_dir, projects, galaxy):
  # co_models from respective files.cum
  model_dirs = ['./' + projects[i] + '/' for i in range(2)]
  mod1_model = import_co_model(model_dirs[0] + combo[0][0])
  mod2_model = import_co_model(model_dirs[1] + combo[1][0])
  # using a frozen column density
  i = nearest_column(columns[0], combo[0], projects[0])
  k = nearest_column(columns[1], combo[1], projects[1])
  mods = ( mod1_model[i], mod2_model[k] )
  # cycle over every normalization
  best_array = [1e99, (0,0,0,0)]
  chi_matrix = np.zeros([len(norms[0]), len(norms[1])])
  for j in range(len(norms[0])):
    for l in range(len(norms[1])):
      idcs = [i,j,k,l]
      N_jl = ( norms[0][j], norms[1][l] )
      chi_matrix[j,l] = 1e99
      if volumes(galaxy, N_jl, projects, mods, combo):
        chi2 = chi_pair(mods, N_jl, cases, galaxy)
        chi_matrix[j,l] = chi2
        best_array = find_best(best_array, chi2, idcs)
  save_chi_matrix(chi_matrix, combo, out_dir)
```

```
  chi2_min = best_array[0]
  best_d1 = mod1_model[best_array[1][0]][0]
  best_N1 = norms[0][best_array[1][1]]
  best_d2 = mod2_model[best_array[1][2]][0]
  best_N2 = norms[1][best_array[1][3]]
  mod1_ladder = mod1_model[best_array[1][0]][1:]
  mod2_ladder = mod2_model[best_array[1][2]][1:]
  mod1_params = (best_d1, best_N1)
  mod2_params = (best_d2, best_N2)
  chi2_params = [mod1_params, mod2_params]
  ladders = [mod1_ladder, mod2_ladder]
  return chi2_min, chi2_params, ladders


def save_co_sled(chi2, params, ladders, c_name, cases, out_dir):
  # import data
  mod1_params, mod2_params = params
  d1, N1 = mod1_params
  d2, N2 = mod2_params
  Dl, co_obs, co_select, Lx, D_max, A = import_galaxy(galaxy)
  # scale the models directly from files.cum
  logmod1 = scale_the_ladder(ladders[0], d1, N1, Dl, cases[0])
  logmod2 = scale_the_ladder(ladders[1], d2, N2, Dl, cases[1])
  # save plt
  with open (out_dir + c_name + '.plt', 'w') as f:
    f.write(
      '#chi: ' + '%.2f' % chi2 + ', ' +
      'depths: ' + '%.3e' % d1 + ', ' + '%.3e' % d2 +
      '; normalizations: ' + str(N1) + ', ' + str(N2) + '\n'
      )
    for j in range(len(co_obs)):
      f.write('  '.join([str(x) for x in co_obs[j]]) + '  ')
      f.write(str(10**logmod1[j]) + '  ')
      f.write(str(10**logmod2[j]) + '  ' + '\n')


def save_combo_matrix(c, combo, chi2_min, chi_params, out_dir):
  galaxy = out_dir.split('_')[-1][:-1]
  matrix_file = out_dir[2:-(len(galaxy)+1)] + 'matrix_' + galaxy
  with open (out_dir + matrix_file, 'a') as f:
    params = list(itertools.chain(
      *[(x[1], x[2]) for x in combo]))
    c_name = generate_combo_name(combo)
    f.write('\n' + str(c).ljust(5) + c_name + '   ')
    f.write('   '.join([str(x) for x in params]) + '   ')
    f.write('%.3f' % chi2_min + '   ')
```

```
    f.write('%.3e' % chi_params[0][0] + '   ')
    f.write(str(chi_params[0][1])  + '   ')
    f.write('%.3e' % chi_params[1][0] + '   ')
    f.write(str(chi_params[1][1])  + '   ')



### FLOW

if prj == 0:
  projects = ['pdrs_combined', 'pdrs_combined']
  cases = [pdr_xdr_cases[0], pdr_xdr_cases[0]]
  columns = [pdr_xdr_columns[0], pdr_xdr_columns[0]]
  norms = [pdr_norms, pdr_norms]
  out_dir = './' + minimize_name + '_double_pdr_' + galaxy + '/'
elif prj == 1:
  projects = ['pdrs_combined', 'xdrs_combined']
  cases = [pdr_xdr_cases[0], pdr_xdr_cases[1]]
  columns = [pdr_xdr_columns[0], pdr_xdr_columns[1]]
  norms = [pdr_norms, xdr_norms]
  out_dir = './' + minimize_name + '_pdr_xdr_' + galaxy + '/'

mod1_sl, mod1_params = import_setlist(projects[0])
mod2_sl, mod2_params = import_setlist(projects[1])
combo_matrix = generate_combo_matrix(mod1_sl, mod2_sl, out_dir)
flux_select = select_combos(combo_matrix, galaxy, projects, columns)

for c in flux_select:
  print c, ' / ', len(combo_matrix)
  combo = combo_matrix[c]
  c_name = generate_combo_name(combo)
  chi2_min, chi2_params, ladders = chi2_minimize(
    combo, columns, norms, cases, out_dir, projects, galaxy)
  save_co_sled(
    chi2_min, chi2_params, ladders, c_name, cases, out_dir)
  save_combo_matrix(c, combo, chi2_min, chi2_params, out_dir)
```

The Python code is organized in three sections: the first contains the libraries to import and the *starters*, the second contains all the defined functions and the third is the *flow* of the code. The best way to read it is to directly jump at the third part, the *flow*, and exploring the functions once called.

Before the execution of this script it is mandatory to prepare, for each simulated grid, a *setlist*, which is just an ordered list containing, for each simulation of the grid, the filename (i.e. the `file.cum` with the CO SLEDs), the values of the two varying physical parameters (density and flux) and a flag that symbolize a not-failed CLOUDY

calculation. The two setlists are imported and used to build the `combo_matrix`, a list containing basically the same informations but for each combination of simulations. Then the code flags, in case of XDRs and if a observed X-ray luminosity is saved into the `import_galaxy` function, the allowed simulations (see section 3.2 for details).

The following part of the code is done for each allowed combination, and all the important stuff is found to be into the `chi2_minimize` function, which calculates the χ^2, for each combination, cycling all the normalizations set. Note that in Python the cycles (like the `for` and `if` cycles) are considered closed just from the code indentation. Within this nested `for` loop, the χ^2 is computed only if the total volume of the model combination is less than the galaxy volume: this task is done by the `volumes` function, that returns just a logical value (i.e. True or False). Once the `minimize_chi` function finds, for a given models combination, the minimum χ^2, it returns it with the normalizations and cloud depths found, saves the CO SLED of this configuration and updates the `combo_matrix`, exported to an external file.

Another code (very elementary) has been used to inspect the `combo_matrix` file, find the best combination (always with the minimum χ^2 criterion) and plot the CO SLEDs, like the ones from figure 3.3 to 3.10.

Bibliography

Abel, N. P., G. J. Ferland, et al. (2005). "The H II Region/PDR Connection: Self-consistent Calculations of Physical Conditions in Star-forming Regions". In: *Astrophysical Journal Supplement Series* 161, pp. 65–95. DOI: 10.1086/432913. eprint: astro-ph/0506514.

Abel, N. P. and S. Satyapal (2008). "[Ne V] Emission in Optically Classified Starbursts". In: *Astrophysical Journal* 678, 686-692, pp. 686–692. DOI: 10.1086/529013. arXiv: 0801.2766.

Abel, N. P., P. A. M. van Hoof, et al. (2008). "Sensitivity of PDR Calculations to Microphysical Details". In: *Astrophysical Journal* 686, 1125-1136, pp. 1125–1136. DOI: 10.1086/591505. arXiv: 0808.2532.

Aird, J. et al. (2010). "The evolution of the hard X-ray luminosity function of AGN". In: *Monthly Notices of the Royal Astronomical Society* 401, pp. 2531–2551. DOI: 10.1111/j.1365-2966.2009.15829.x. arXiv: 0910.1141.

Armus, L., J. Bernard-Salas, et al. (2006). "Detection of the Buried Active Galactic Nucleus in NGC 6240 with the Infrared Spectrograph on the Spitzer Space Telescope". In: *Astrophysical Journal* 640, pp. 204–210. DOI: 10.1086/500040. eprint: astro-ph/0511381.

Armus, L., J. M. Mazzarella, et al. (2009). "GOALS: The Great Observatories All-Sky LIRG Survey". In: *Publications of the Astronomical Society of Pacific* 121, p. 559. DOI: 10.1086/600092. arXiv: 0904.4498.

Arshutkin, L. N. (1985). "Study of carbon monoxide formation in interstellar clouds". In: *Astrophysics* 22, pp. 100–107. DOI: 10.1007/BF01084466.

Ascasibar, Y. and A. I. Dıaz (2010). "Photoionized gas in hydrostatic equilibrium: the role of gravity". In: *Monthly Notices of the Royal Astronomical Society* 404, pp. 275–282. DOI: 10.1111/j.1365-2966.2010.16270.x. arXiv: 1001.3035 [astro-ph.IM].

Baillard, A. et al. (2011). "The EFIGI catalogue of 4458 nearby galaxies with detailed morphology". In: *Astronomy & Astrophysics* 532, A74, A74. DOI: 10.1051/0004-6361/201016423. arXiv: 1103.5734.

Baldwin, J. A., M. M. Phillips, and R. Terlevich (1981). "Classification parameters for the emission-line spectra of extragalactic objects". In: *Publications of the Astronomical Society of the Pacific* 93, pp. 5–19. DOI: 10.1086/130766.

Bolatto, A. D., M. Wolfire, and A. K. Leroy (2013). "The CO-to-H_2 Conversion Factor". In: *Annual Review of Astronomy and Astrophysics* 51, pp. 207–268. DOI: 10.1146/annurev-astro-082812-140944. arXiv: 1301.3498.

Brightman, M. and K. Nandra (2011). "An XMM-Newton spectral survey of 12 μm selected galaxies - I. X-ray data". In: *Monthly Notices of the Royal Astronomical Society* 413, pp. 1206–1235. DOI: 10.1111/j.1365-2966.2011.18207.x. arXiv: 1012.3345 [astro-ph.HE].

Calzetti, D. (2011). "Polycyclic Aromatic Hydrocarbons as Star Formation Rate Indicators". In: *EAS Publications Series*. Ed. by C. Joblin and A. G. G. M. Tielens. Vol. 46. EAS Publications Series, pp. 133–141. DOI: 10.1051/eas/1146014. arXiv: 1010.4996.

Cami, J. et al. (2010). "Detection of C_{60} and C_{70} in a Young Planetary Nebula". In: *Science* 329, p. 1180. DOI: 10.1126/science.1192035.

Carral, P. et al. (1994). "The interstellar medium in the starburst regions of NGC 253 and NGC 3256". In: *Astrophysical Journal* 423, pp. 223–236. DOI: 10.1086/173801.

Carroll, Bradley W. and Dale A. Ostlie (2007). *An Introduction to Modern Astrophysics*. Ed. by San Francisco: Pearson Addison-Wesley. 2nd (International).

Chomiuk, L. and M. S. Povich (2011). "Toward a Unification of Star Formation Rate Determinations in the Milky Way and Other Galaxies". In: *Astronomical Journal* 142, 197, p. 197. DOI: 10.1088/0004-6256/142/6/197. arXiv: 1110.4105.

Chung, A. et al. (2009). "The Redshift Search Receiver Observations of ^{12}CO J = 1 $\rightarrow$ 0 in 29 Ultraluminous Infrared Galaxies". In: *Astronomical Journal* 138, pp. 858–872. DOI: 10.1088/0004-6256/138/3/858. arXiv: 0906.2797.

Collinson, J. S. et al. (2017). "Reaching the peak of the quasar spectral energy distribution - II. Exploring the accretion disc, dusty torus and host galaxy". In: *Monthly Notices of the Royal Astronomical Society* 465, pp. 358–382. DOI: 10.1093/mnras/stw2666. arXiv: 1610.04221 [astro-ph.HE].

Cowie, L. L. and A. Songaila (1986). "High-resolution optical and ultraviolet absorption-line studies of interstellar gas". In: *Annual Review of Astronomy and Astrophysics* 24, pp. 499–535. DOI: 10.1146/annurev.aa.24.090186.002435.

Daddi, E. et al. (2010). "Different Star Formation Laws for Disks Versus Starbursts at Low and High Redshifts". In: *Astrophysical Journal Letters* 714, pp. L118–L122. DOI: 10.1088/2041-8205/714/1/L118. arXiv: 1003.3889.

Delvecchio, I. et al. (2014). "Tracing the cosmic growth of supermassive black holes to z 3 with Herschel". In: *Monthly Notices of the Royal Astronomical Society* 439, pp. 2736–2754. DOI: 10.1093/mnras/stu130. arXiv: 1401.4503.

Dyson, J. E. and D. A. Williams (1997). *The physics of the interstellar medium*. DOI: 10.1201/9780585368115.

Eldridge, J. J. (2012). "Stochasticity, a variable stellar upper mass limit, binaries and star formation rate indicators". In: *Monthly Notices of the Royal Astronomical Society* 422, pp. 794–803. DOI: 10.1111/j.1365-2966.2012.20662.x. arXiv: 1106.4311 [astro-ph.SR].

Ferland, G. J. et al. (2013). "The 2013 Release of Cloudy". In: *Revista Mexicana de Astronomía y Astrofísica* 49, pp. 137–163. arXiv: 1302.4485 [astro-ph.GA].

Fernández, X. et al. (2010). "A Radio Perspective on the Wet Merger Remnant NGC 34". In: *Astronomical Journal* 140, pp. 1965–1974. DOI: 10.1088/0004-6256/140/6/1965. arXiv: 1010.0948.

Ferrarese, L. and D. Merritt (2000). "A Fundamental Relation between Supermassive Black Holes and Their Host Galaxies". In: *Astrophysical Journal Letters* 539, pp. L9–L12. DOI: 10.1086/312838. eprint: astro-ph/0006053.

Field, G. B. (1965). "Thermal Instability." In: *Astrophysical Journal* 142, p. 531. DOI: 10.1086/148317.

Fraternali, F. et al. (2002). "Deep H I Survey of the Spiral Galaxy NGC 2403". In: *Astronomical Journal* 123, pp. 3124–3140. DOI: 10.1086/340358. eprint: astro-ph/0203405.

Gao, Y. and P. M. Solomon (2004a). "HCN Survey of Normal Spiral, Infrared-luminous, and Ultraluminous Galaxies". In: *Astrophysical Journal Supplement Series* 152, pp. 63–80. DOI: 10.1086/383003. eprint: astro-ph/0310341.

— (2004b). "The Star Formation Rate and Dense Molecular Gas in Galaxies". In: *Astrophysical Journal* 606, pp. 271–290. DOI: 10.1086/382999. eprint: astro-ph/0310339.

Gebhardt, K. et al. (2000). "A Relationship between Nuclear Black Hole Mass and Galaxy Velocity Dispersion". In: *Astrophysical Journal Letters* 539, pp. L13–L16. DOI: 10.1086/312840. eprint: astro-ph/0006289.

González-Alfonso, E. et al. (2012). "Herschel/PACS spectroscopy of NGC 4418 and Arp 220: H_2O, $H_2{}^{18}O$, OH, ^{18}OH, O I, HCN, and NH_3". In: *Astronomy & Astrophysics* 541, A4, A4. DOI: 10.1051/0004-6361/201118029. arXiv: 1109.1118.

Griffin, M. J. et al. (2010). "The Herschel-SPIRE instrument and its in-flight performance". In: *Astronomy & Astrophysics* 518, L3, p. L3. DOI: 10.1051/0004-6361/201014519. arXiv: 1005.5123 [astro-ph.IM].

Guainazzi, M., G. Matt, and G. C. Perola (2005). "X-ray obscuration and obscured AGN in the local universe". In: *Astronomy and Astrophysics* 444, pp. 119–132. DOI: 10.1051/0004-6361:20053643. eprint: astro-ph/0508265.

Gültekin, K. et al. (2009). "The M-σ and M-L Relations in Galactic Bulges, and Determinations of Their Intrinsic Scatter". In: *Astrophysical Journal* 698, pp. 198–221. DOI: 10.1088/0004-637X/698/1/198. arXiv: 0903.4897 [astro-ph.GA].

Güver, T. and F. Özel (2009). "The relation between optical extinction and hydrogen column density in the Galaxy". In: *Monthly Notices of the Royal Astronomical Society* 400, pp. 2050–2053. DOI: 10.1111/j.1365-2966.2009.15598.x. arXiv: 0903.2057.

Habing, H. J. (1968). "The interstellar radiation density between 912 A and 2400 A". In: *Bulletin of the Astronomical Institutes of the Netherlands* 19, p. 421.

Harrison, C. (2014). "Observational constraints on the influence of active galactic nuclei on the evolution of galaxies". PhD thesis. Durham University.

Heckman, T. M. (1980). "An optical and radio survey of the nuclei of bright galaxies - Activity in normal galactic nuclei". In: *Astronomy & Astrophysics* 87, pp. 152–164.

Heckman, T. M., L. Armus, and G. K. Miley (1990). "On the nature and implications of starburst-driven galactic superwinds". In: *Astrophysical Journal Supplement Series* 74, pp. 833–868. DOI: 10.1086/191522.

Heckman, T. M., L. Blitz, et al. (1989). "A millimeter-wave survey of CO emission in Seyfert galaxies". In: *Astrophysical Journal* 342, pp. 735–758. DOI: 10.1086/167633.

Hollenbach, D. J. and A. G. G. M. Tielens (1997). "Dense Photodissociation Regions (PDRs)". In: *Annual Review of Astronomy and Astrophysics* 35, pp. 179–216. DOI: 10.1146/annurev.astro.35.1.179.

Hopkins, P. F. et al. (2008). "A Cosmological Framework for the Co-Evolution of Quasars, Supermassive Black Holes, and Elliptical Galaxies. I. Galaxy Mergers and Quasar Activity". In: *Astrophysical Journal Supplement Series* 175, 356-389, pp. 356–389. DOI: 10.1086/524362. arXiv: 0706.1243.

Imanishi, M. et al. (2004). "Near-Infrared and Millimeter Constraints on the Nuclear Energy Source of the Infrared-luminous Galaxy NGC 4418". In: *Astronomical Journal* 128, pp. 2037–2047. DOI: 10.1086/424620. eprint: astro-ph/0407469.

Indriolo, N. et al. (2010). "Constraining the Environment of CH^+ Formation with CH^+_3 Observations". In: *Astrophysical Journal* 711, pp. 1338–1342. DOI: 10.1088/0004-637X/711/2/1338. arXiv: 1002.1315.

Karttunen, H. et al., eds. (2007). *Fundamental Astronomy*.

Kennicutt Jr., R. C. (1998). "The Global Schmidt Law in Star-forming Galaxies". In: *Astrophysical Journal* 498, pp. 541–552. DOI: 10.1086/305588. eprint: astro-ph/9712213.

Kennicutt, R. C. and N. J. Evans (2012). "Star Formation in the Milky Way and Nearby Galaxies". In: *Annual Review of Astronomy and Astrophysics* 50, pp. 531–608. DOI: 10.1146/annurev-astro-081811-125610. arXiv: 1204.3552.

Kewley, L. J. et al. (2006). "The host galaxies and classification of active galactic nuclei". In: *Monthly Notices of the Royal Astronomical Society* 372, pp. 961–976. DOI: 10.1111/j.1365-2966.2006.10859.x. eprint: astro-ph/0605681.

Koda, J. et al. (2009). "Dynamically Driven Evolution of the Interstellar Medium in M51". In: *Astrophysical Journal Letters* 700, pp. L132–L136. DOI: 10.1088/0004-637X/700/2/L132. arXiv: 0907.1656 [astro-ph.CO].

Komossa, S. et al. (2003). "Discovery of a Binary Active Galactic Nucleus in the Ultraluminous Infrared Galaxy NGC 6240 Using Chandra". In: *Astrophysical Journal* 582, pp. L15–L19. DOI: 10.1086/346145. eprint: astro-ph/0212099.

Lada, C. J., J. Forbrich, et al. (2012). "Star Formation Rates in Molecular Clouds and the Nature of the Extragalactic Scaling Relations". In: *Astrophysical Journal* 745, 190, p. 190. DOI: 10.1088/0004-637X/745/2/190. arXiv: 1112.4466.

Lada, C. J., M. Lombardi, and J. F. Alves (2010). "On the Star Formation Rates in Molecular Clouds". In: *Astrophysical Journal* 724, pp. 687–693. DOI: 10.1088/0004-637X/724/1/687. arXiv: 1009.2985.

Larson, R. B. (1981). "Turbulence and star formation in molecular clouds". In: *Monthly Notices of the Royal Astronomical Society* 194, pp. 809–826. DOI: 10.1093/mnras/194.4.809.

Leitherer, C., S. Ekström, et al. (2014). "The Effects of Stellar Rotation. II. A Comprehensive Set of Starburst99 Models". In: *Astrophysical Journal Supplement Series* 212, 14, p. 14. DOI: 10.1088/0067-0049/212/1/14. arXiv: 1403.5444.

Leitherer, C., D. Schaerer, et al. (1999). "Starburst99: Synthesis Models for Galaxies with Active Star Formation". In: *Astrophysical Journal Supplement Series* 123, pp. 3–40. DOI: 10.1086/313233. eprint: astro-ph/9902334.

Li, A. (2007). "Dust in Active Galactic Nuclei". In: *The Central Engine of Active Galactic Nuclei*. Ed. by L. C. Ho and J.-W. Wang. Vol. 373. Astronomical Society of the Pacific Conference Series, p. 561.

Madau, P. and M. Dickinson (2014). "Cosmic Star-Formation History". In: *Annual Review of Astronomy and Astrophysics* 52, pp. 415–486. DOI: 10.1146/annurev-astro-081811-125615. arXiv: 1403.0007.

Madau, P., L. Pozzetti, and M. Dickinson (1998). "The Star Formation History of Field Galaxies". In: *Astrophysical Journal* 498, pp. 106–116. DOI: 10.1086/305523. eprint: astro-ph/9708220.

Maiolino, R. et al. (2003). "Elusive active galactic nuclei". In: *Monthly Notices of the Royal Astronomical Society* 344, pp. L59–L64. DOI: 10.1046/j.1365-8711.2003.07036.x. eprint: astro-ph/0307380.

Maloney, P. R., D. J. Hollenbach, and A. G. G. M. Tielens (1996). "X-Ray–irradiated Molecular Gas. I. Physical Processes and General Results". In: *Astrophysical Journal* 466, p. 561. DOI: 10.1086/177532.

Mangum, J. G. (2016). "Calibration of the Atacama Large Millimeter Array". In: *The Science of Calibration*. Ed. by S. Deustua et al. Vol. 503. Astronomical Society of the Pacific Conference Series, p. 69.

Mathis, J. S., W. Rumpl, and K. H. Nordsieck (1977). "The size distribution of interstellar grains". In: *Astrophysical Journal* 217, pp. 425–433. DOI: 10.1086/155591.

McKee, C. F. and E. C. Ostriker (2007). "Theory of Star Formation". In: *Annual Review of Astronomy and Astrophysics* 45, pp. 565–687. DOI: 10.1146/annurev.astro.45.051806.110602. arXiv: 0707.3514.

McMullin, J. P. et al. (2007). "CASA Architecture and Applications". In: *Astronomical Data Analysis Software and Systems XVI*. Ed. by R. A. Shaw, F. Hill, and D. J. Bell. Vol. 376. Astronomical Society of the Pacific Conference Series, p. 127.

Meijerink, R., M. Spaans, and F. P. Israel (2007). "Diagnostics of irradiated dense gas in galaxy nuclei. II. A grid of XDR and PDR models". In: *Astronomy & Astrophysics* 461, pp. 793–811. DOI: 10.1051/0004-6361:20066130. eprint: astro-ph/0610360.

Meyer, D. M., M. Jura, and J. A. Cardelli (1998). "The Definitive Abundance of Interstellar Oxygen". In: *Astrophysical Journal* 493, pp. 222–229. DOI: 10.1086/305128. eprint: astro-ph/9710163.

Mukai, K. (1993). "PIMMS and Viewing: proposal preparation tools". In: *Legacy, vol.3, p.21-31* 3, pp. 21–31.

Omont, A. (2007). "Molecules in galaxies". In: *Reports on Progress in Physics* 70, pp. 1099–1176. DOI: 10.1088/0034-4885/70/7/R03. arXiv: 0709.3814.

Osterbrock, D. E. (1991). "Active galactic nuclei". In: *Reports on Progress in Physics* 54, pp. 579–633. DOI: 10.1088/0034-4885/54/4/002.

Papadopoulos, P. P. et al. (2012). "The molecular gas in luminous infrared galaxies - I. CO lines, extreme physical conditions and their drivers". In: *Monthly Notices of the Royal Astronomical Society* 426, pp. 2601–2629. DOI: 10.1111/j.1365-2966.2012.21001.x. arXiv: 1109.4176.

Pereira-Santaella, M. et al. (2014). "Warm molecular gas temperature distribution in six local infrared bright Seyfert galaxies". In: *Astronomy & Astrophysics* 566, A49, A49. DOI: 10.1051/0004-6361/201423430. arXiv: 1404.6470.

Pilbratt, G. L. et al. (2010). "Herschel Space Observatory. An ESA facility for far-infrared and submillimetre astronomy". In: *Astronomy & Astrophysics* 518, L1, p. L1. DOI: 10.1051/0004-6361/201014759. arXiv: 1005.5331 [astro-ph.IM].

Pozzi, F. et al. (2017). "CO excitation in the Seyfert galaxy NGC7130". In: *ArXiv e-prints*. arXiv: 1705.08221.

Rickard, L. J. et al. (1975). "Detection of extragalactic carbon monoxide at millimeter wavelengths". In: *Astrophysical Journal Letters* 199, pp. L75–L78. DOI: 10.1086/181852.

Rigopoulou, D. et al. (1999). "A Large Mid-Infrared Spectroscopic and Near-Infrared Imaging Survey of Ultraluminous Infrared Galaxies: Their Nature and Evolution". In: *Astronomical Journal* 118, pp. 2625–2645. DOI: 10.1086/301146. eprint: astro-ph/9908300.

Rosenberg, M. J. F. et al. (2015). "The Herschel Comprehensive (U)LIRG Emission Survey (HERCULES): CO Ladders, Fine Structure Lines, and Neutral Gas Cooling". In: *Astrophysical Journal* 801, 72, p. 72. DOI: 10.1088/0004-637X/801/2/72. arXiv: 1501.02985.

Rupke, D. S. N. and S. Veilleux (2015). "Spatially Extended Na I D Resonant Emission and Absorption in the Galactic Wind of the Nearby Infrared-Luminous Quasar F05189-2524". In: *Astrophysical Journal* 801, 126, p. 126. DOI: 10.1088/0004-637X/801/2/126. arXiv: 1411.3744.

Salpeter, E. E. (1955). "The Luminosity Function and Stellar Evolution." In: *Astrophysical Journal* 121, p. 161. DOI: 10.1086/145971.

Sanders, D. B., J. M. Mazzarella, et al. (2003). "The IRAS Revised Bright Galaxy Sample". In: *Astronomical Journal* 126, pp. 1607–1664. DOI: 10.1086/376841. eprint: astro-ph/0306263.

Sanders, D. B. and I. F. Mirabel (1996). "Luminous Infrared Galaxies". In: *Annual Review of Astronomy and Astrophysics* 34, p. 749. DOI: 10.1146/annurev.astro.34.1.749.

Sanders, D. B., N. Z. Scoville, and B. T. Soifer (1991). "Molecular gas in luminous infrared galaxies". In: *Astrophysical Journal* 370, pp. 158–171. DOI: 10.1086/169800.

Sargent, M. T. et al. (2014). "Regularity Underlying Complexity: A Redshift-independent Description of the Continuous Variation of Galaxy-scale Molecular Gas Properties in the Mass-star Formation Rate Plane". In: *Astrophysical Journal* 793, 19, p. 19. DOI: 10.1088/0004-637X/793/1/19. arXiv: 1303.4392.

Savage, B. D. and K. R. Sembach (1996). "Interstellar Abundances from Absorption-Line Observations with the Hubble Space Telescope". In: *Annual Review of Astronomy and Astrophysics* 34, pp. 279–330. DOI: 10.1146/annurev.astro.34.1.279.

Schmidt, M. (1959). "The Rate of Star Formation." In: *Astrophysical Journal* 129, p. 243. DOI: 10.1086/146614.

Schweizer, F. and P. Seitzer (2007). "Remnant of a "Wet" Merger: NGC 34 and Its Young Massive Clusters, Young Stellar Disk, and Strong Gaseous Outflow". In: *Astronomical Journal* 133, pp. 2132–2155. DOI: 10.1086/513317. eprint: astro-ph/0702645.

Shankar, F., D. H. Weinberg, and J. Miralda-Escudé (2009). "Self-Consistent Models of the AGN and Black Hole Populations: Duty Cycles, Accretion Rates, and the Mean Radiative Efficiency". In: *Astrophysical Journal* 690, pp. 20–41. DOI: 10.1088/0004-637X/690/1/20. arXiv: 0710.4488.

Shirley, Y. L. (2015). "The Critical Density and the Effective Excitation Density of Commonly Observed Molecular Dense Gas Tracers". In: *Publications of the Astronomical Society of Pacific* 127, p. 299. DOI: 10.1086/680342. arXiv: 1501.01629 [astro-ph.IM].

Solomon, P. M. et al. (1997). "The Molecular Interstellar Medium in Ultraluminous Infrared Galaxies". In: *Astrophysical Journal* 478, pp. 144–161. DOI: 10.1086/303765. eprint: astro-ph/9610166.

Spoon, H. W. W. et al. (2001). "The obscured mid-infrared continuum of NGC 4418: A dust- and ice-enshrouded AGN". In: *Astronomy & Astrophysics* 365, pp. L353–L356. DOI: 10.1051/0004-6361:20000557. eprint: astro-ph/0012011.

Strong, A. W. and J. R. Mattox (1996). "Gradient model analysis of EGRET diffuse Galactic γ-ray emission." In: *Astronomy & Astrophysics* 308, pp. L21–L24.

Strong, M. et al. (2004). "Molecular gas properties of 12-μm Seyfert galaxies - I. The southern sample". In: *Monthly Notices of the Royal Astronomical Society* 353, pp. 1151–1160. DOI: 10.1111/j.1365-2966.2004.08139.x.

Vallini, L. et al. (2017). "Molecular cloud photoevaporation and far-infrared line emission". In: *Monthly Notices of the Royal Astronomical Society* 467, pp. 1300–1312. DOI: 10.1093/mnras/stx180. arXiv: 1606.08464.

van der Tak, F. F. S. et al. (2007). "A computer program for fast non-LTE analysis of interstellar line spectra. With diagnostic plots to interpret observed line intensity ratios". In: *Astronomy & Astrophysics* 468, pp. 627–635. DOI: 10.1051/0004-6361:20066820. arXiv: 0704.0155.

Varenius, E. et al. (2014). "The radio core structure of the luminous infrared galaxy NGC 4418. A young clustered starburst revealed?" In: *Astronomy & Astrophysics* 566, A15, A15. DOI: 10.1051/0004-6361/201323303. arXiv: 1403.3782.

Veilleux, S. et al. (1995). "Optical Spectroscopy of Luminous Infrared Galaxies. II. Analysis of the Nuclear and Long-Slit Data". In: *Astrophysical Journal Supplement Series* 98, p. 171. DOI: 10.1086/192158.

Vignati, P. et al. (1999). "BeppoSAX unveils the nuclear component in NGC 6240". In: *Astronomy & Astrophysics* 349, pp. L57–L60. eprint: astro-ph/9908253.

Williams, J. P. et al. (1998). "The Ionization Fraction in Dense Molecular Gas. I. Low-Mass Cores". In: *Astrophysical Journal* 503, pp. 689–699. DOI: 10.1086/306034.

Wilson, R. W., K. B. Jefferts, and A. A. Penzias (1970). "Carbon Monoxide in the Orion Nebula". In: *Astrophysical Journal Letters* 161, p. L43. DOI: 10.1086/180567.

Wootten, A. and A. R. Thompson (2009). "The Atacama Large Millimeter/Submillimeter Array". In: *IEEE Proceedings* 97, pp. 1463–1471. DOI: 10.1109/JPROC.2009.2020572. arXiv: 0904.3739 [astro-ph.IM].

Xue, R. and M. Huang (2009). "PDR diagnostics study with CLOUDY". In: *Research in Astronomy and Astrophysics* 9, pp. 457–469. DOI: 10.1088/1674-4527/9/4/008.

Zamorani, G. et al. (1981). "X-ray studies of quasars with the Einstein Observatory. II". In: *Astrophysical Journal* 245, pp. 357–374. DOI: 10.1086/158815.